applied sciences

MDPI

Article

Numerical and Analytical Analysis of the Low-Frequency Magnetic Fields Generated by Three-Phase Underground Power Cables with Solid Bonding

Eduard Lunca *, Silviu Vornicu and Alexandru Sălceanu

Department of Electrical Measurements and Materials, "Gheorghe Asachi" Technical University of Iasi, 23 Professor Dimitrie Mangeron Blvd., 700050 Iasi, Romania; silviu-constantin.vornicu@academic.tuiasi.ro (S.V.); asalcean@tuiasi.ro (A.S.)

* Correspondence: elunca@tuiasi.ro; Tel.: +40-232-701246

Abstract: There is a special concern for measuring and simulating low-frequency magnetic fields generated by underground power cables, particularly in human exposure studies. In the present study, an accurate 2D finite element model for computing magnetic fields generated by three-phase underground power cables with solid bonding is proposed. The model is developed in ANSYS Maxwell 2D low-frequency electromagnetic field simulation software for a typical 12/20 kV (medium-voltage) three-phase underground power cable in both trefoil and flat formations, but it can be adapted to any cable system. Model validation is achieved by analytical computations conducted with a software tool based on the Biot–Savart law and the superposition principle. RMS magnetic flux density profiles calculated at various heights above the ground with these two methods correlate very well. This is also true for induced shield currents. The application of the finite element model to multiple three-phase power cables laid together is also considered.

Keywords: magnetic field; underground power cable; solid bonding; finite element model; analytical calculation

Citation: Lunca, E.; Vornicu, S.; Sălceanu, A. Numerical and Analytical Analysis of the Low-Frequency Magnetic Fields Generated by Three-Phase Underground Power Cables with Solid Bonding. *Appl. Sci.* **2023**, *13*, 6328. https://doi.org/10.3390/app13106328

Academic Editor: Mario Lucido

Received: 21 April 2023
Revised: 16 May 2023
Accepted: 19 May 2023
Published: 22 May 2023

1. Introduction

The general concern and implicit interest in monitoring the low-frequency magnetic fields generated by underground electric cables (in either transmission or especially distribution networks) has recently been augmented. If in the case of the high-voltage transmission systems, underground power cables are a solution only in certain special cases (water or wide road crossings or particularly scenic areas), we can say that in the urban distribution area, underground power cables (of medium voltage) are an increasingly applied solution. Assembly and installation costs are considerably higher by comparison with the overhead solution, but aesthetics and reliability are significantly improved, leading to reductions of up to 10 fold in outage duration. On the other hand, the three-phase underground power cables in the distribution systems, which may carry currents of hundreds of amperes at voltages of tens or sometimes even hundreds of kV, are found in the immediate vicinity of humans, much closer than overhead power lines. What are the values of the electric and magnetic fields generated and to what extent can they be controlled and reduced is a question that concerns every citizen. Consequently, the specialists must provide scientifically based answers [1].

Regarding electric fields, the shielding effect achieved due to the Faraday cage principle is very strong, being mainly produced by the conductive metallic screen/shield that protects any underground cable (when bonded to ground, it will also carry out the short circuit fault current), or by the ground in which the cable is buried (which has some conductive properties). In contrast, shielding magnetic fields is much more complicated and expensive. There are two techniques: ferromagnetic shielding (performed with shields made of materials

with high magnetic permeability, on the principle of the path of minimum reluctance) and induced current shielding (which is effective only if the shield is a good electrical conductor and thick enough). In addition to high costs and constructive-technological difficulties, these solutions for shielding magnetic fields also have the important disadvantage of increasing the losses produced by line charging currents. That is why they will be applied only on relatively short distances and only in the case of very special requirements [2,3].

Therefore, as in the case of overhead power lines, it is strongly recommended that through analytical calculations, numerical modeling or actual measurements, to be verified that the low-frequency magnetic field generated by underground power cables at the soil level is (far) below the values considered acceptable by the health regulations. Computations, which can be quite accurate, are often preferable to measurements because they can be performed for any desired scenario, rather than being limited to the particular conditions at the measurement time [4–8].

A common 2D approach for calculating magnetic fields generated by underground power cables is based on the Biot–Savart law and the superposition principle, assuming that the cables are straight, horizontal, infinitely long and parallel to each other and the effect of the induced shield currents on the magnetic field is negligible [9–12]. Basically, this is the case for single-point bonding systems and cross-bonding systems, in which the induced shield currents are zero or insignificant. However, when dealing with solid bonding (i.e., the underground power cables operate with their metallic shields bonded and grounded at both ends), the circulating currents induced in shields may achieve the same order as the wire-core currents, which leads to a certain total magnetic field reduction. In some studies, e.g., [13,14], analytical expressions for the induced shield currents have been obtained under balanced three-phase conditions. It has also been considered the magnetic field reduction.

Some 2D finite element method (FEM) models have also been developed for computing magnetic fields from three-phase underground cables with solid bonding. In [15], COMSOL Multiphysics is used to investigate the magnetic field reduction rate for a three-phase cable in flat formation as a function of the distance between cables, the shield diameter, as well as the cross-sectional area of the cable shields. In [16], QuickField was mainly used for predicting underground cable ampacity (for both trefoil and flat formations), while the developed model also allows investigating the magnetic field distribution at the ground surface (only limited results are presented). For a similar purpose (flat formation only), ANSYS Maxwell is used in [17].

In our study, which is an extended version of [18], FEM based on ANSYS Maxwell (2D) software is used to compute low-frequency magnetic fields generated by three-phase underground power cables with solid bonding according to the usual procedures applied in human exposure studies. Both trefoil and flat formations of a 12/20 kV (medium-voltage) three-phase power cable are considered for FEM model implementation. For its validation, calculated magnetic fields and induced shield currents are checked by comparison with analytical results obtained with a software tool based on the Biot–Savart law and the superposition principle, which represents an updated version of a previously developed program [19]. Finally, the application of the FEM model to multiple three-phase power cables laid together is considered. In all cases, the magnetic field reduction rate due to induced shield currents is determined as well.

The computational time, generally a major drawback of using FEM [20], is, in this study, quite acceptable, in the order of 10 to 25 min (simple cable formation, depending on mesh size). Compared to the analytical approach, which is limited to simple trefoil and flat formations of cables, the FEM model can also be applied to various types of cable arrangements while taking into account different influencing factors, such as the relative phase sequences and positions of the cables. Hence, it may be used not only for assessing compliance with relevant magnetic field exposure regulations, but also as an accurate tool for optimizing cable layout and location to mitigate magnetic field problems. Usually, the

modification of the total magnetic field due to induced shield currents is not considered in the commercially available software for power cable system analysis.

2. Physical Model Selected for Analysis

The single-core power cables in a three-phase circuit can be laid out in a number of formations. Typical ones are trefoil and flat. In the first case, the three cables are placed in the corners of an equilateral triangle, as presented in Figure 1a; in the second case, the three cables are placed in the same horizontal plane, at equal distances between adjacent cables, as presented in Figure 1b. The choice of use depends on several factors such as shield bonding method, conductor area and available space for installation [21,22].

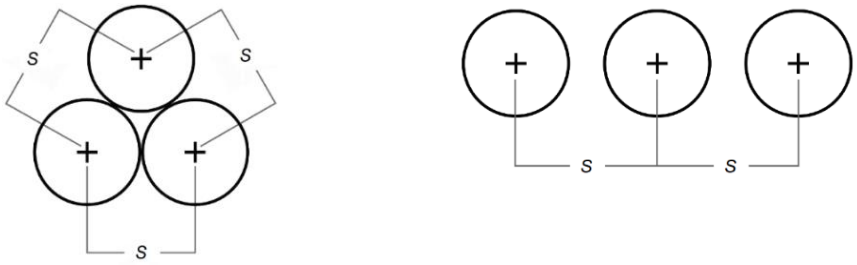

(**a**) (**b**)

Figure 1. Typical cable formations: (**a**) trefoil formation; (**b**) flat formation.

In solid bonding systems (suitable for cable lengths over 500 m), the cable shields are grounded at both ends of the cables, as depicted in Figure 2, where R_g represents the grounding resistance. This bonding scheme will reduce the induced shield voltages, but there will be circulating shield currents proportional to the wire-core currents. This will cause losses in the shields, which reduce the cable current carrying capacity. At the same time, the circulating shield current generates a magnetic field that is significantly out of phase with respect to the wire-core magnetic field. In the following, only the total magnetic field will be investigated.

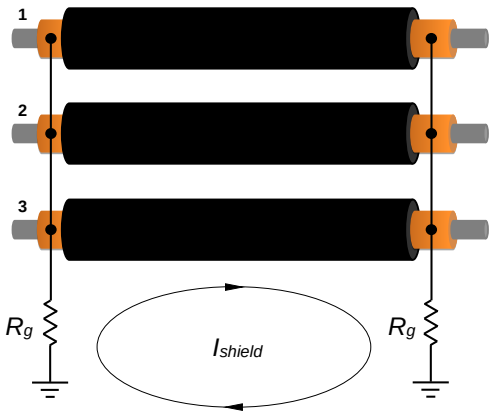

Figure 2. Solid bonding.

Since solid bonding is more common for medium-voltage applications, a 12/20 kV NA2XS(F)2Y single-core cable (Figure 3) has been selected for finite element analysis. The cable is constructed from aluminum (Al) core conductor with the cross-sectional area of 150 mm^2, semi-conductive layer over conductor, core insulation of cross-linked polyethylene (XLPE), semi-conductive layer over insulation, swelling tape, copper (Cu) wire shield with the cross-sectional area of 25 mm^2, waterproofing tape and outer sheath of high-density polyethylene (HDPE). The current carrying capacity when buried in the ground is 319 A for trefoil formation and 352 A for flat formation, respectively. Other cable characteristics are given in Table 1.

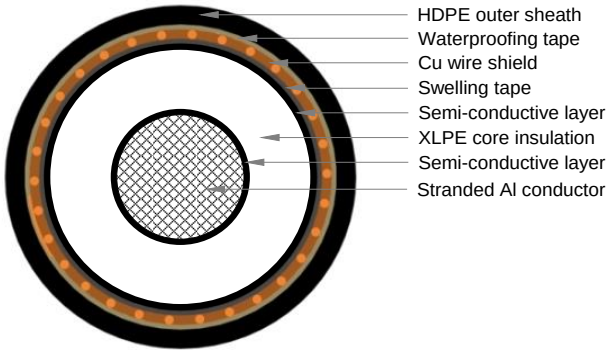

Figure 3. NA2XS(F)2Y cable.

Table 1. Cable characteristics.

Cable Characteristic	Value
Core conductor diameter	14.2 mm
Nominal cross-sectional area of core conductor	150 mm^2
Thickness of XLPE insulation	5.5 mm
Diameter over insulation	26.4 mm
Diameter over copper shield	30.5 mm
Nominal cross-sectional area of shield	25 mm^2
Diameter over HDPE sheath (over complete cable)	36 mm
Nominal phase-to-ground/phase-to-phase voltage	12/20 kV
DC resistance of conductor at 20 °C	0.206 Ω/km
Maximum operating conductor temperature	+90 °C

The physical layout of the analyzed three-phase cable system is presented in Figure 4, where two cases are considered in conformity with the national regulations regarding the design and execution of the electrical cable networks [23]:

- The three phases are buried in the ground, at a depth of 0.8 m, in trefoil formation (the spacing between the centers of any two cables is 36 mm, as dictated by the cable outer diameter), Figure 4a;
- The three phases are buried in the ground, at a depth of 0.8 m, in flat formation with clearance between cables of 70 mm (the spacing between the centers of the adjacent cables is 106 mm), Figure 4b.

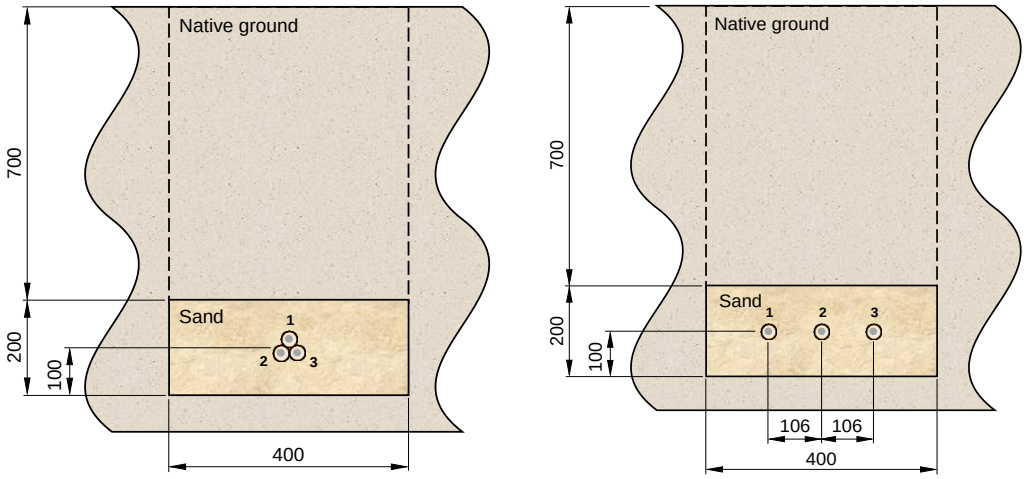

Figure 4. Physical layout of the analyzed three-phase cable system: (**a**) trefoil formation; (**b**) flat formation with spacing (all dimensions are given in mm).

In both cases, the power cables are located in a rectangular trench 0.9 m deep and 0.4 m wide, between two sand layers of 0.1 m thickness. Both ends of all cable shields are connected to ground, as indicated in Figure 2.

For model implementation and its validation, it is assumed that the three-phase cable system has exactly balanced currents, as follows: $\boldsymbol{I_1} = I \angle -120^\circ$, $\boldsymbol{I_2} = I \angle 0^\circ$ and $\boldsymbol{I_3} = I \angle 120^\circ$. Computations will be performed at maximum rated current (319 A and 352 A, respectively), assuming that the actual laying depth has no significant influence on the maximum admissible load current, which is otherwise compensated by the reduction in the ambient temperature and the more favorable specific thermal resistances of the ground at bigger laying depths (according to [23], the usual laying depth range is approximately 0.7 m ÷ 1.2 m). Additionally, the surrounding ground is considered electrically homogenous and non-magnetic.

3. Finite Element Model

ANSYS Maxwell 2D is a powerful software package that uses the finite element method to solve 2D low-frequency electromagnetic problems, by specifying the appropriate geometry, material properties and excitations for a device or system of devices [24,25]. The proposed magnetic field problem is solved using the eddy current field solver, which allows computing steady state, time-varying (AC) magnetic fields at a given frequency, here 50 Hz. It also computes current densities, taking into account eddy current effects in solid conductors (including skin and proximity effects), as well as other quantities that can be derived from the magnetic field solution. An adaptive mesh refinement technique is used to achieve the best mesh required to meet the defined accuracy level.

The quantities that the eddy current field simulator resolves are the magnetic vector potential ($\boldsymbol{A}$)—related to magnetic flux density by $\boldsymbol{B} = \nabla \times \boldsymbol{A}$—and the electric scalar potential (V). A first equation used for this purpose, derived from Maxwell's equations, is:

$$\nabla \times \frac{1}{\mu}(\nabla \times \boldsymbol{A}) = (\sigma + j\omega\varepsilon)(-j\omega\boldsymbol{A} - \nabla V), \tag{1}$$

where μ is the absolute magnetic permeability, σ is the electrical conductivity, and $\omega = 2\pi f$ is the angular frequency at which all quantities are oscillating and ε is the absolute electric permittivity.

As we can see, the right side of (1) consists of a complex conductivity, $\sigma + j\omega\varepsilon$, multiplied by the complex value of the electric field strength, i.e., $\boldsymbol{E} = -j\omega\boldsymbol{A} - \nabla V$. Therefore, the result is the complex current density, $\boldsymbol{J}$, which is the sum of three components:

- $\boldsymbol{J_s} = -\sigma\nabla V$, the source current density due to the differences in electric potential;
- $\boldsymbol{J_e} = -j\omega\sigma\boldsymbol{A}$, the induced eddy current density due to time-varying magnetic fields;
- $\boldsymbol{J_d} = j\omega\varepsilon(-j\omega\boldsymbol{A} - \nabla V)$, the displacement current density due to time-varying electric fields.

Since the total current (I_T) flowing in any conductor that is connected to an external source is specified when setting up the problem, a second equation used by the eddy current module to solve for $\boldsymbol{A}$ and V is:

$$I_T = \int_S \boldsymbol{J} dS = \int_S (\sigma + j\omega\varepsilon)(-j\omega\boldsymbol{A} - \nabla V), \tag{2}$$

which basically states that the total current in a conductor equals the integral of $\boldsymbol{J}$ over the cross-sectional area of the conductor, S.

Because $\boldsymbol{B}$ is assumed to lie in the xy plane, $\boldsymbol{A}$ has only a component in the z direction. Therefore, the eddy current module will solve only for $\boldsymbol{A_z}(x,y)$. Additionally, $\boldsymbol{E}$ has a z component only, which means that V is constant over the entire cross section of a conductor. Therefore, it is not necessary to solve for V at every node.

3.1. Global FEM Model, Boundary Conditions and Solver Setup

The global FEM model of the three-phase cable system is depicted in Figure 5a, where the computational domain is a square of side a = 20 m, sufficiently large to determine the

behavior of the magnetic field well outside from the cable central axis. A discretized section around the power cables is given in Figure 5b. The power cables are buried—according to the geometrical dimensions in Figure 4a (for trefoil formation) and Figure 4b (for flat formation)—in a ground with the electrical conductivity $\sigma = 0.01$ S/m, the relative magnetic permeability $\mu_r = 1$ and the relative electric permittivity $\varepsilon_r = 10$. The half top layer in Figure 5a models the air. The model depth (cable length) is 1 m.

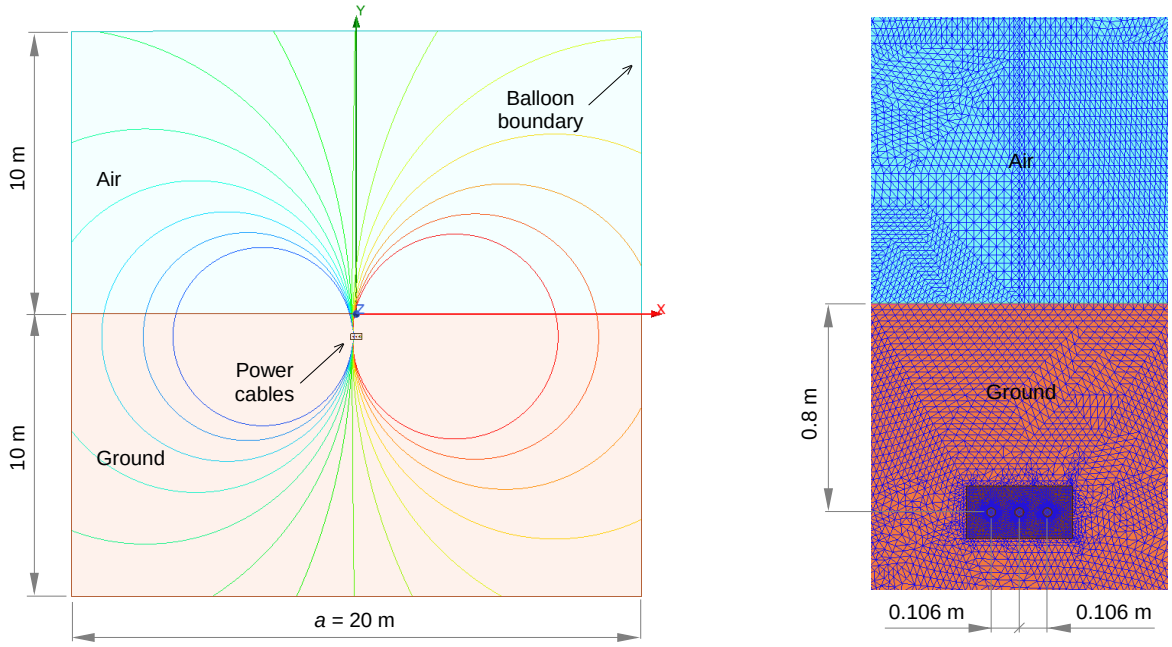

(**a**) (**b**)

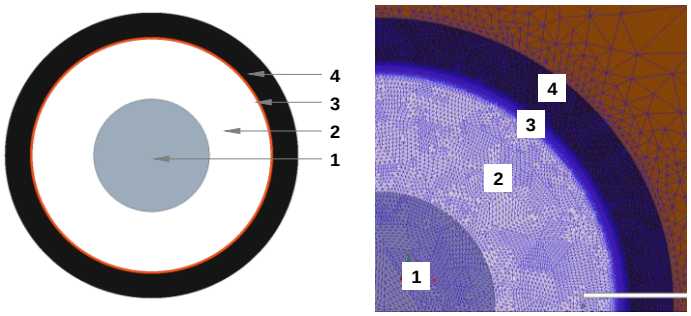

Layer No	Cable layer	Dimension
1	Aluminium conductor	r = 7.1 mm
2	XLPE insulation	th = 7.5655 mm
3	Copper (pipe) shield	th = 0.269 mm
4	HDPE oversheath	th = 3.0655 mm

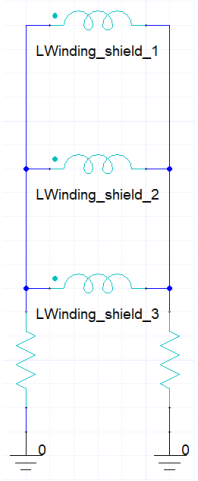

(**c**) (**d**)

Figure 5. The 2D FEM model for computing magnetic fields from a three-phase underground cable system with solid bonding: (**a**) global geometric model; (**b**) discretized section around the power cables; (**c**) simplified cable model; (**d**) coupled circuit for shield bonding.

All power cables are modeled as presented in Figure 5c, using a simplified four-layer cable model consisting of Al core conductor ($\sigma_{20} = 35.38 \times 10^6$ S/m, $\mu_r = 1$ and $\varepsilon_r = 1$), XLPE insulation ($\sigma = 1 \times 10^{-15}$ S/m, $\mu_r = 1$ and $\varepsilon_r = 2.5$), Cu shield ($\sigma_{20} = 58 \times 10^6$ S/m, $\mu_r = 1$ and $\varepsilon_r = 1$) and HDPE oversheath ($\sigma = 1 \times 10^{-14}$ S/m, $\mu_r = 1$ and $\varepsilon_r = 2.3$). The equivalent thickness (th) of the Cu shield layer is chosen so that it closely matches the nominal 25 mm^2 cross-sectional area of the real wire shield, while its mean radius is exactly

the same, 14.8 mm. For cables with metallic sheets, the sheet layer in the cable model will simply reflect the cross section of the real sheet. In simulation, the aforementioned conductivities (at T_0 = 20 °C) of the metallic layers will be adjusted to maximum operating temperatures (90 °C for Al core conductors; approximately 80 °C for Cu shields), by taking into account the following temperature coefficients (of resistivity, $\rho = 1/\sigma$) per K at 20 °C [26]: 4.03×10^{-3} for Al and, respectively, 3.93×10^{-3} for Cu.

Since the analyzed cable structure is assumed to be completely isolated from other magnetic fields or sources of current, Balloon boundary conditions are assigned to all four edges of the defined computational domain. In this case, the magnetic vector potential, $\boldsymbol{A}_z$, goes to zero at infinity; the magnetic flux lines are neither tangential nor normal to the Balloon boundary. At the interfaces between objects, natural boundary conditions are automatically assigned by the eddy current module.

The values of the wire-core currents (amplitude and phase) are assigned using the software functionality "Current Excitation", while the shield bonding is encoded in the model by the coupled circuit in Figure 5d, where external windings are used for controlling the induced shield currents. This electrical circuit was defined with Maxwell Circuit Editor. As mentioned above, only perfectly balanced currents are considered for model implementation and further validation, but unbalanced loading conditions can also be managed. By simulation, the effect of grounding resistance was proved to be insignificant.

A fine mesh was defined for analysis, totalizing a number of triangle elements in the order of 1,300,000. The mesh refinement was achieved by restricting the maximum length of the elements in all model blocks, ensuring that high-resolution magnetic field profiles are generated over a large distance of interest with respect to the cable central axis (a number of preliminary tests with mesh size were performed). The maximum element length in the (very thin) shield blocks is 0.05 mm, which represents the minimum defined over the entire domain. In the air and surrounding ground, the maximum element length is 60 mm, which represents the maximum defined over the entire domain.

The adaptive setup was configured with a maximum number of passes of 10 and a percent error of 0.1. The convergence was set as 30% refinement per pass, minimum number of passes of 2 and minimum number of converged passes of 1. The adaptive frequency is 50 Hz.

3.2. Calculation of RMS Magnetic Flux Density

According to the usual evaluation procedures applied in magnetic field exposure studies, we are mainly interested in computing lateral profiles of the RMS magnetic flux density at various heights above the ground, particularly at the standard height of 1 m. Such profiles of B_{RMS} are calculated in a separate Microsoft Excel worksheet, where a sufficiently large number of instantaneous magnetic flux density profiles (generated over a 20-ms period) are imported and then "summed" together with the formula [18,27]:

$$B_{RMS}(i) = \sqrt{\frac{1}{N}\sum_{n=1}^{N} B_n^2(i)}, \tag{3}$$

where $B_1(i), \ldots, B_N(i)$ are the instantaneous values of the magnetic flux density corresponding to the point i of the profile and N stands for the total number of values (profiles). Here, we use N = 73.

On this basis, for I = 319 A, Figure 6a shows lateral profiles of the instantaneous magnetic flux density up to 10 m from the central axis of the three-phase power cable in trefoil formation, at the height of 1 m above the ground, as well as the correspondent B_{RMS} profile (blue thick line). A 2D distribution of the instantaneous magnetic flux density around the three-phase cable in trefoil formation (at the time t = 16.94 ms, at which the peak magnetic flux density in Figure 6a is obtained) is presented in Figure 6b. Similarly, by adopting I = 352 A, Figure 7a shows simulation results for the three-phase power cable in flat formation. A 2D distribution of the instantaneous magnetic flux density around the three-phase cable in flat formation (at the time t = 15.56 ms, at which the peak magnetic

flux density in Figure 7a is obtained) is depicted in Figure 7b. More details on the magnetic fields and induced shield currents from both configurations are discussed in Section 5.

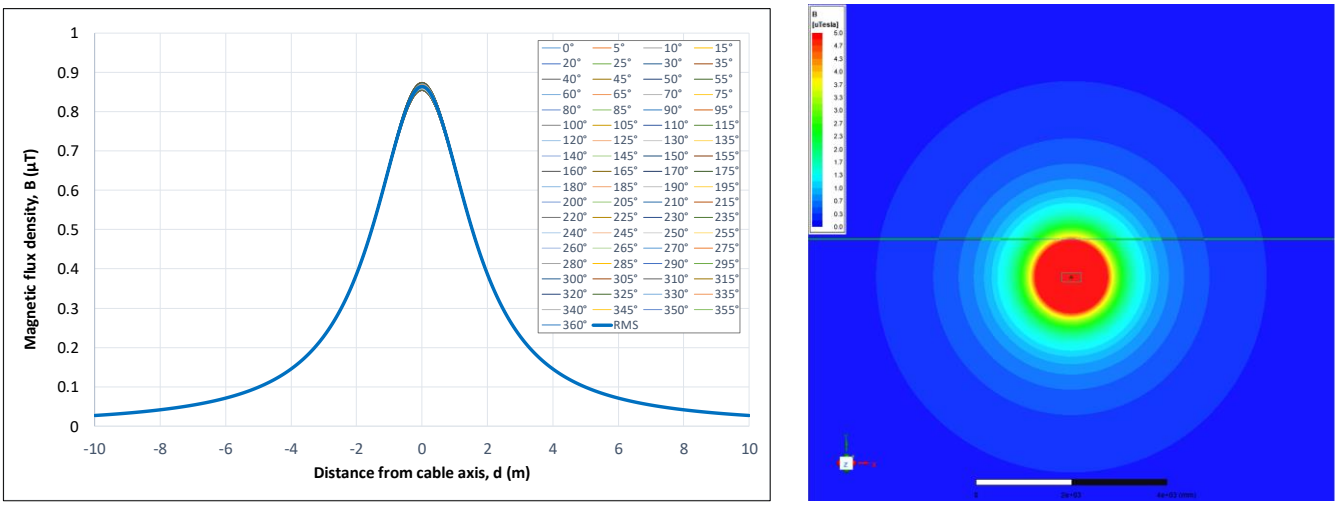

(**a**) (**b**)

Figure 6. Example of simulation results for the three-phase power cable in trefoil formation: (**a**) instantaneous magnetic flux density profiles and calculated RMS magnetic flux density profile at the height h = 1 m above the ground; (**b**) a momentary magnetic field distribution in the cross section of the power cable (t = 16.94 ms).

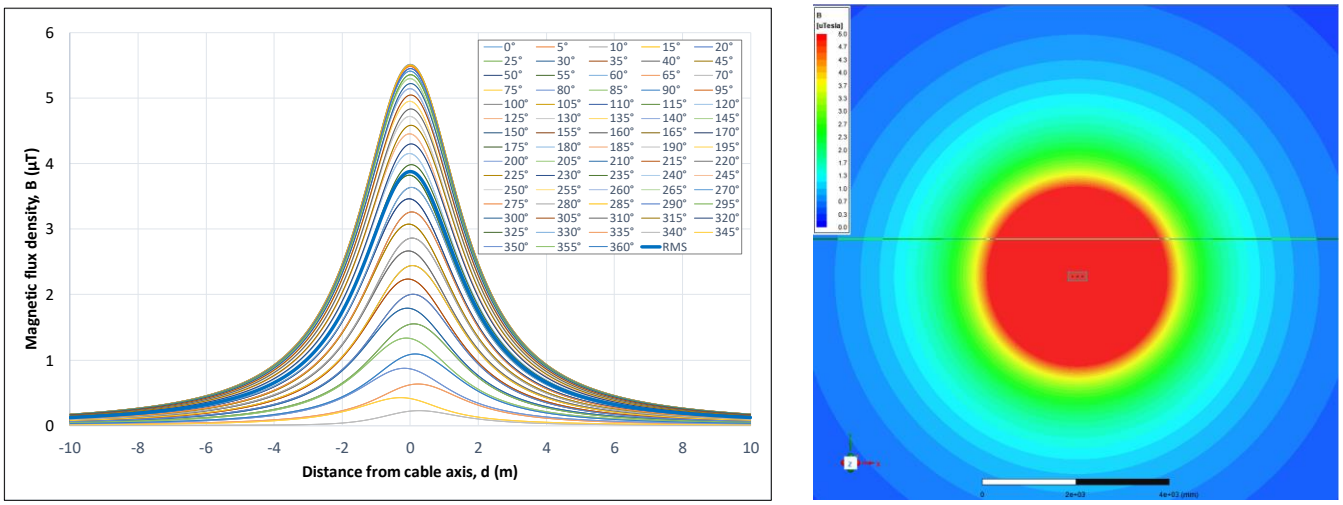

(**a**) (**b**)

Figure 7. Example of simulation results for the three-phase power cable in flat formation: (**a**) instantaneous magnetic flux density profiles and calculated RMS magnetic flux density profile at the height h = 1 m above the ground; (**b**) a momentary magnetic field distribution in the cross section of the power cable (t = 15.56 ms).

4. Analytical Approach for FEM Model Validation

To verify the numerical results obtained with the proposed FEM model, an interactive software tool based on the Biot–Savart law and the superposition principle has been developed. Assuming that the power cables are straight and infinitely long, the total magnetic flux density at any measuring point (x, y) in the vicinity of a three-phase power cable with solid bonding can be calculated as (Figure 8):

$$\boldsymbol{B_x} = \sum_{i=1}^{3} \frac{-\mu_0}{2\pi}(\boldsymbol{I_i} + \boldsymbol{I_{sh\_i}})\left[\frac{y - y_i}{r_i^2}\right]; \tag{4}$$

$$\boldsymbol{B_y} = \sum_{i=1}^{3} \frac{\mu_0}{2\pi}(\boldsymbol{I_i} + \boldsymbol{I_{sh\_i}})\left[\frac{x - x_i}{r_i^2}\right]; \tag{5}$$

$$\boldsymbol{B} = \sqrt{|\boldsymbol{B_x}|^2 + |\boldsymbol{B_y}|^2}, \tag{6}$$

where $\boldsymbol{I_i}$ is the phase current carried by the conductor located at (x_i, y_i), $\boldsymbol{I_{sh\_i}}$ is the circulating current in the shield located at (x_i, y_i), $r_i = \sqrt{(x - x_i)^2 + (y - y_i)^2}$ represents the distance between the conductor/shield and the measurement point (x, y) and $\mu_0 = 4\pi \times 10^{-7}$ H/m is the magnetic permeability of the free space.

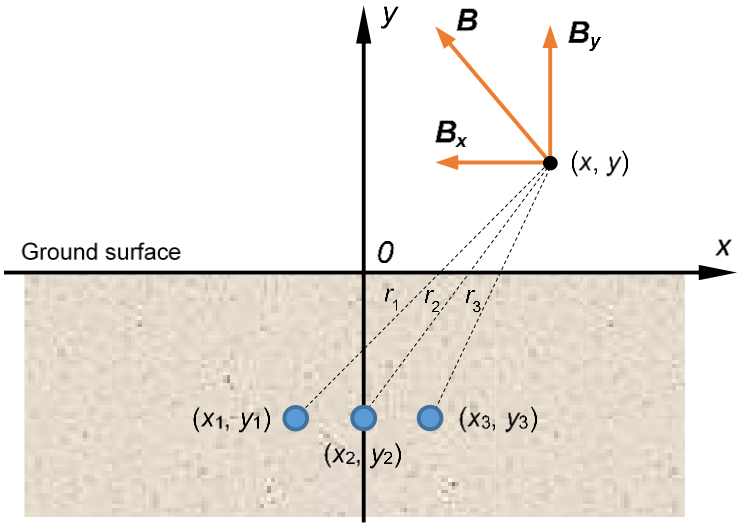

Figure 8. The 2D analytical calculation of the magnetic flux density generated by a three-phase power cable with solid bonding.

If considering the same phase sequence ($\boldsymbol{I_1} = I \angle -120°$, $\boldsymbol{I_2} = I \angle 0°$ and $\boldsymbol{I_3} = I \angle 120°$), it can be shown that the currents induced in the shields of the three-phase power cable in trefoil formation (Figure 1a) have the general form [21,26]:

$$\boldsymbol{I_{sh\_i}} = -\boldsymbol{I_i}\frac{jX}{R_{sh} + jX}, \tag{7}$$

where $X = 2 \times \omega \times 10^{-7} \ln(s/r_{sh})$ represents the shield reactance per unit length of cable, in Ω /m, and R_{sh} is the shield DC resistance per unit length of cable, in Ω/m. In the expression of X, s is the spacing between the centers of the (adjacent) conductors, in m, and r_{sh} is the mean of the outer and inner radii of the shield, in m.

Similarly, for balanced phase currents, the currents induced in the shields of the three-phase power cable in flat formation (Figure 1b) have the following expressions [21,26]:

$$\boldsymbol{I_{sh\_1}} = \frac{\boldsymbol{I_2}}{2}\left[\frac{Q^2}{R_{sh}^2 + Q^2} - \frac{\sqrt{3}R_{sh}P}{R_{sh}^2 + P^2} + j\left(\frac{R_{sh}Q}{R_{sh}^2 + Q^2} + \frac{\sqrt{3}P^2}{R_{sh}^2 + P^2}\right)\right]; \tag{8}$$

$$\boldsymbol{I_{sh\_2}} = -\boldsymbol{I_2}\left(\frac{Q^2}{R_{sh}^2 + Q^2} + j\frac{R_{sh}Q}{R_{sh}^2 + Q^2}\right); \tag{9}$$

$$\boldsymbol{I_{sh\_3}} = \frac{\boldsymbol{I_2}}{2}\left[\frac{Q^2}{R_{sh}^2 + Q^2} + \frac{\sqrt{3}R_{sh}P}{R_{sh}^2 + P^2} + j\left(\frac{R_{sh}Q}{R_{sh}^2 + Q^2} - \frac{\sqrt{3}P^2}{R_{sh}^2 + P^2}\right)\right], \tag{10}$$

where $Q = X - X_m/3$, $P = X + X_m$, $X = 2 \times \omega \times 10^{-7} \ln(s/r_{sh})$ represents the shield reactance per unit length of cable for two adjacent single-core cables, in Ω/m, and $X_m = 2 \times \omega \times 10^{-7} \ln 2$ is the mutual reactance per unit length of cable between the shield of an outer cable and the conductors of the other two, in Ω/m.

Finally, the shield resistance R_{sh} (at the shield temperature T_{sh}) is calculated with the formula:

$$R_{sh} = \frac{\rho_{sh20}}{A_{sh}}[1 + \alpha_{sh20}(T_{sh} - 20)], \quad (11)$$

where ρ_{sh20} is the electrical resistivity of the shield material at 20 °C, A_{sh} is the shield cross-sectional area and α_{sh20} is the temperature coefficient of resistance at 20 °C. In our case, at T_{sh} = 80 °C, R_{sh} = 0.852 mΩ/m.

All these equations, together with a field mapping algorithm, have been implemented into a LabVIEW program that is able to generate lateral profiles of the total RMS magnetic flux density, B, as well as of its transversal components, B_x and B_y, at any user-defined height above the ground. The program also displays the induced shield currents (RMS value and phase). Magnetic flux density profiles generated with this simulation tool for trefoil formation (I = 319 A) and flat formation (I = 352 A) are presented in Figure 9a,b, respectively. Detailed comparisons to numerical results are presented in Section 5.

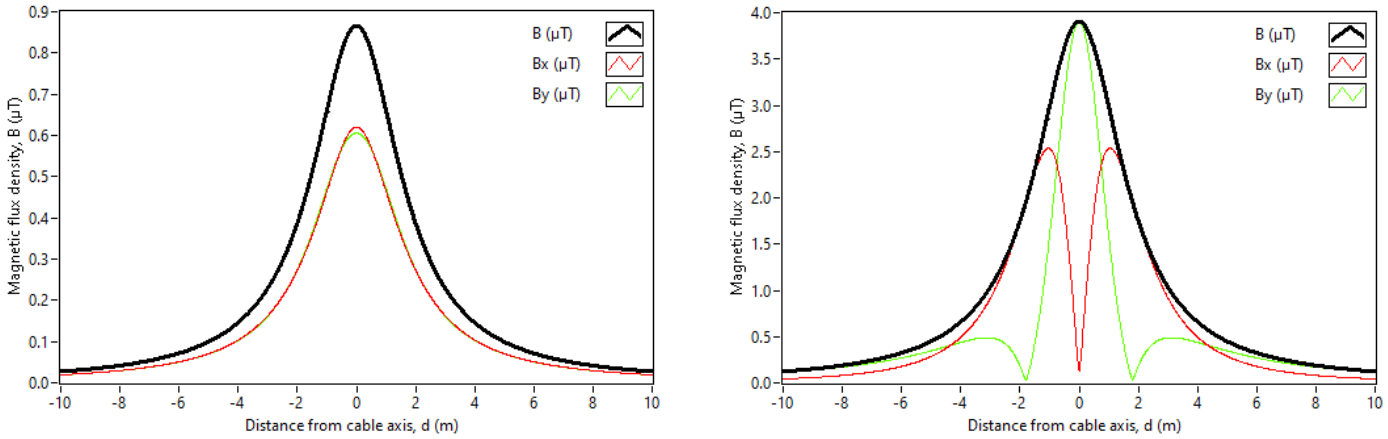

Figure 9. Example of results obtained by analytical computation (the total RMS magnetic flux density and its transversal components at the height of 1 m above the ground): (**a**) for the three-phase power cable in trefoil formation; (**b**) for the three-phase power cable in flat formation.

5. Results and Discussions

5.1. Magnetic Fields from the Considered Trefoil and Flat Formations

Comparisons between FEM simulation results and analytical computation results (lateral profiles of the total RMS magnetic flux density at the height of 1 m above the ground) for the considered trefoil and flat formations are given in Figure 10a,b, respectively. Induced shield currents calculated by both methods are given in Tables 2 and 3, respectively. As it can be seen, the results obtained by the two methods correlate very well. The smallest difference in the RMS magnetic flux density at the cable central axis is obtained for trefoil formation (Figure 10a), namely 2.36 nT. For the three-phase underground power cable in flat formation (Figure 10b), the difference in RMS magnetic flux density at the centerline is 26.49 nT. In both cases, lower values of magnetic flux density have been obtained by numerical simulation. Clearly, these differences are too small for any practical purposes related to magnetic field exposure assessment, but we may assume a slightly different evaluation of the electromagnetic interaction between models (eddy currents in shields are neglected in the analytical model).

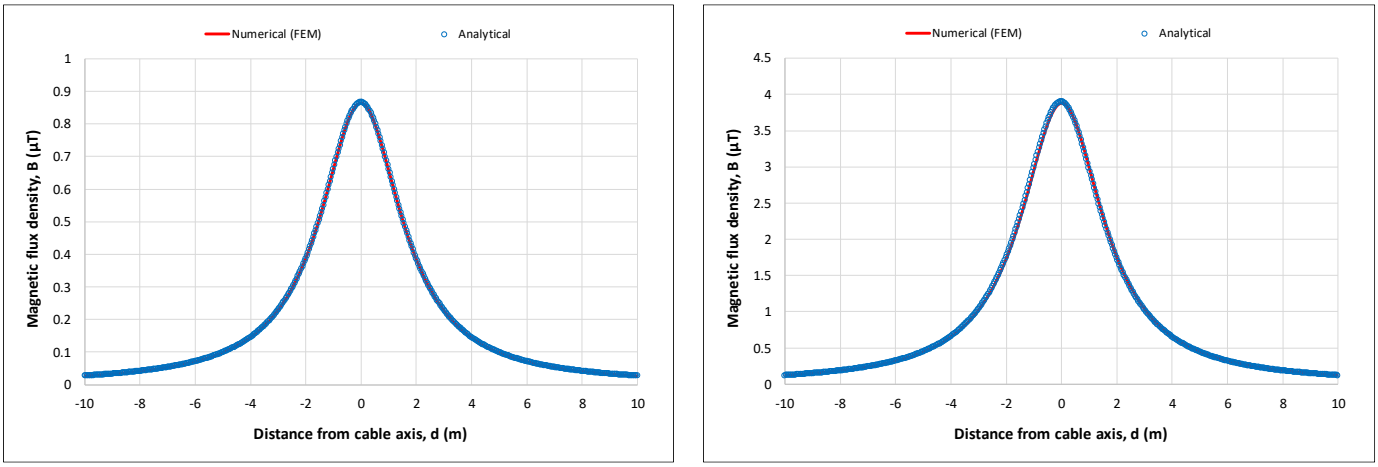

(**a**) (**b**)

Figure 10. Comparison between numerical and analytical results (RMS magnetic flux density profiles at the height of 1 m above the ground): (**a**) for the three-phase power cable in trefoil formation; (**b**) for the three-phase power cable in flat formation.

Table 2. Induced shield currents obtained by numerical simulation and analytical computation (trefoil formation).

Current No.	Conductor Current		Shield Current (FEM)		Shield Current (Analytical)	
	RMS Value (A)	Phase (°)	RMS Value (A)	Phase (°)	RMS Value (A)	Phase (°)
1	319	–120	20.816	145.371	20.872	146.248
2	319	0	20.814	–94.625	20.872	–93.752
3	319	120	20.814	25.368	20.872	26.248

Table 3. Induced shield currents obtained by numerical simulation and analytical computation (flat formation).

Current No.	Conductor Current		Shield Current (FEM)		Shield Current (Analytical)	
	RMS Value (A)	Phase (°)	RMS Value (A)	Phase (°)	RMS Value (A)	Phase (°)
1	352	–120	64.129	148.533	64.229	148.547
2	352	0	44.704	–97.308	44.757	–97.305
3	352	120	61.347	10.178	61.454	10.196

Decreasing the number of mesh elements to about 620,000 still produces very accurate results in the RMS magnetic flux density (differences below 0.04% at the height of 1 m above the ground, regardless the measurement point), while the computation time reduces from about 25 min to 10 min (Intel® Core™ i7-12700H Processor, 14 CPU, 16 GB RAM, GeForce RTX 3050 GPU). Doubling and even tripling the number of mesh elements has no significant effect on the calculated RMS magnetic flux density profile at the height of 1 m above the ground.

With the setting of Balloon boundary conditions, the distance from the source of magnetic fields (cables) to the outer boundary is not a critical issue, since different dimensions of boundary has almost no effect on the simulation results (for instance, the simulation results obtained by doubling the side a of the computational domain are virtually identical). If the side a of the computational domain reduces to half, the differences in the RMS magnetic flux density at the height of 1 m above the ground, regardless the measurement point, do not exceed 0.06%.

Lateral profiles of the total RMS magnetic flux density at several heights above the ground, obtained by numerical simulation only, are presented in Figure 11a,b, respectively.

At maximum rated current (319 A), the magnetic field at the central axis of the three-phase power cable in trefoil formation is very low compared to the ICNIRP 1998 limit for general public (100 μT at 50 Hz) [28], ranging from 4.377 μT at the ground level (0-m height) to 0.357 μT at the height of 2 m. At the standard height of 1 m, the RMS magnetic flux density at the centerline is 0.864 μT (115.74-fold below the ICNIRP reference level), while at the distance of 10 m from the cable axis it falls to only 0.027% of the ICNIRP limit. Much higher exposure levels can be observed for the three-phase power cable in flat formation (maximum rated current of 352 A), in which case the RMS magnetic flux density above the cable axis varies from 19.409 μT at 0-m height to 1.604 μT at the height of 2 m. Once again, at the standard height of 1 m, the RMS magnetic flux density at the centerline is 3.876 μT (25.8-fold below the ICNIRP reference level), falling to 0.122% of the ICNIRP limit at the distance of 10 m from the cable axis. These values should be seen as maximum exposure levels from such common configurations of 12/20 kV three-phase underground power cables.

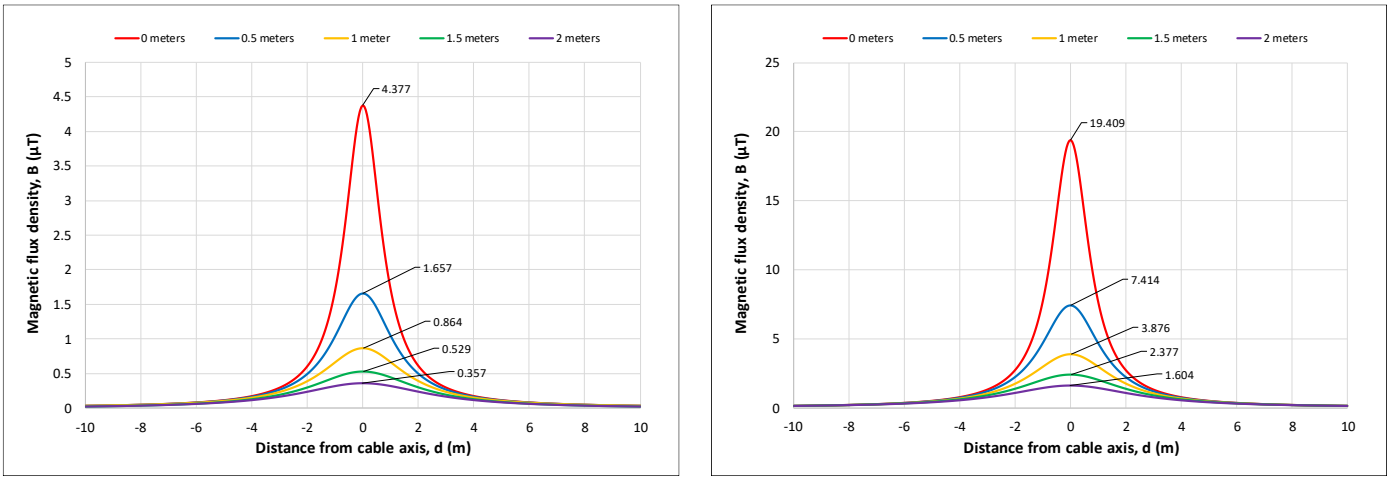

(**a**) (**b**)

Figure 11. Magnetic flux density profiles at several heights above the ground, obtained by numerical simulation: (**a**) for trefoil formation; (**b**) for flat formation.

To illustrate the effect of shields on the magnetic field reduction, Figure 12a,b compare vertical profiles of the total RMS magnetic flux density at the central axis of the two analyzed cable structures, obtained by numerical simulation, with solidly bonded and non-bonded shields. As shown in Figure 12a, for trefoil formation, the underground cable with solidly bonded shields produces a magnetic field that is only 0.41% lower than the magnetic field created by the non-bonded cable. For flat cable formation (Figure 12b), the magnetic field reduction effect is more evident, namely 1.83%. If we theoretically assume that both the core conductors and shields operate at a temperature of 20 °C (hence they exhibit lower resistivity, see Section 3), these figures increase to 0.62% and 2.76%, respectively.

As it can be observed from the results presented above, the magnetic field reduction rate for the analyzed cable configurations is quite low. However, for other cable systems, depending on their geometry and the cable characteristics, it may significantly increase. For instance, if we replace the 12/20 kV NA2XS(F)2Y single-core cable used in the FEM model with a similar one, but having a copper wire shield with the cross-sectional area of 50 mm^2, the RMS magnetic flux density at the central axis of the two three-phase power cables will have the vertical profiles given in Figures 13a and 13b, respectively. Now, for trefoil formation, the underground cable with solidly bonded shields generates a magnetic field that is 1.45% lower than the magnetic field created by the non-bonded cable (Figure 13a), while the magnetic field reduction rate for flat formation increases to 6.76% (Figure 13b).

At a temperature of 20 °C for both the core conductors and shields, the magnetic field reduction rates increase to 2.24% and 9.82%, respectively.

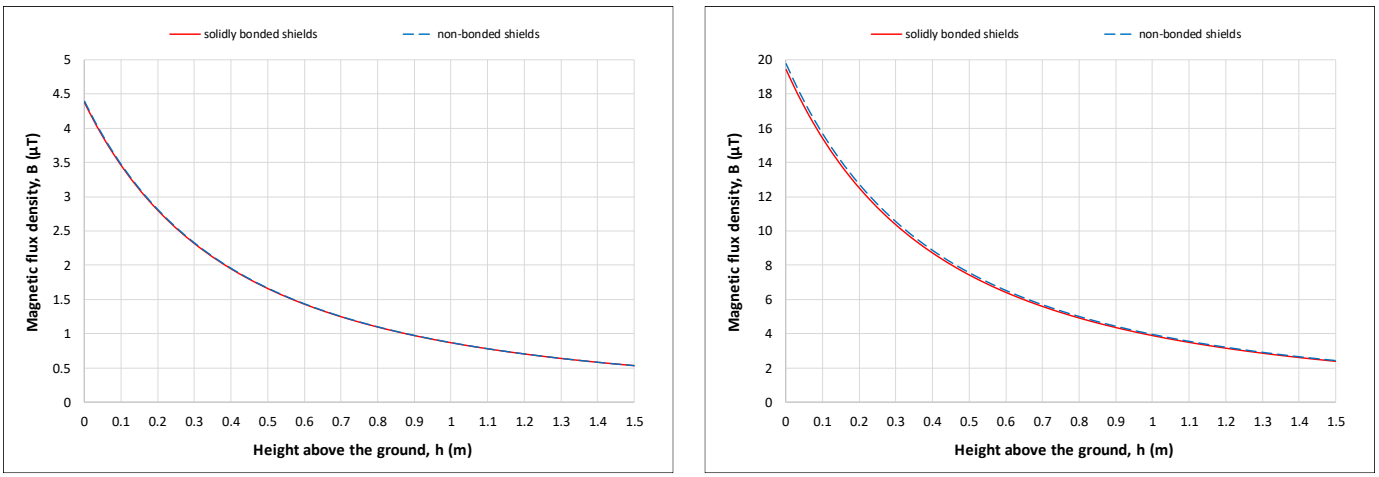

Figure 12. Magnetic flux density at the central axis of the three-phase power cable with solidly bonded shields and non-bonded shields, obtained by numerical simulation: (**a**) for trefoil formation; (**b**) for flat formation.

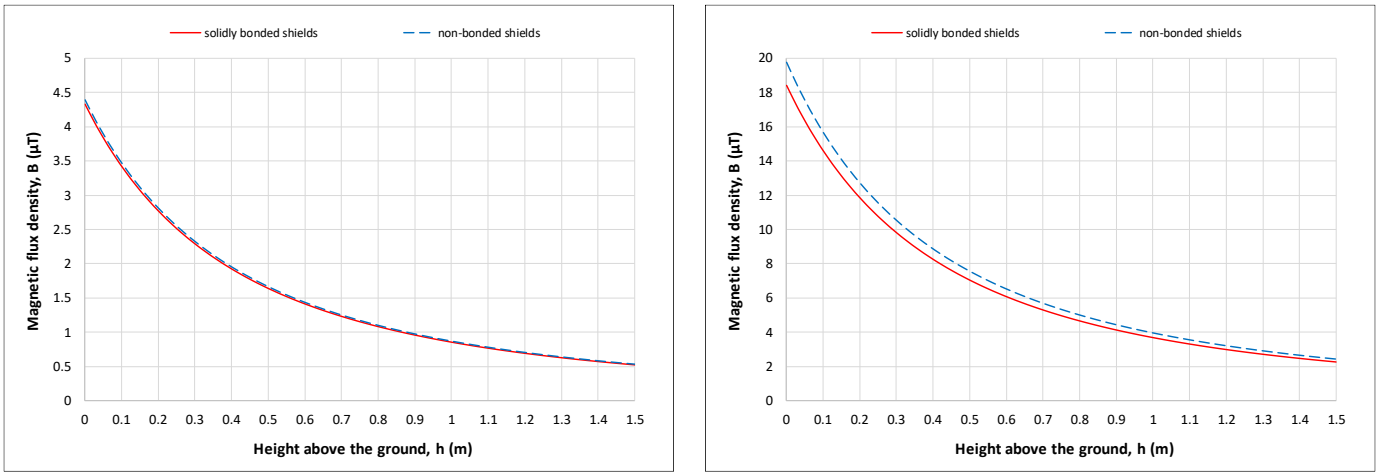

Figure 13. Magnetic flux density at the central axis of the three-phase underground power cable with solidly bonded shields and non-bonded shields (50 mm^2 copper wire shield), obtained by numerical simulation: (**a**) for trefoil formation; (**b**) for flat formation.

Compared to FEM, the software based on standard formulas provides much faster results, but it can only be applied to simple trefoil and flat formations of underground power cables (under balanced loading conditions). On the other hand, FEM is much more flexible, allowing to take into consideration different cable aspects (armoring, current unbalance, etc.), and it can easily be extended to various types of cable arrangements. Such an example will be presented in the following.

5.2. Magnetic Field from Two Adjacent Three-Phase Power Cables in Flat Formation

After FEM model validation, it was used to investigate the magnetic flux density distribution and magnetic field reduction rate for an arrangement of two adjacent three-phase power cables (with solid bonding) laid horizontally in the ground, also at the burial

depth of 0.8 m (Figure 14). Each individual cable is modeled as presented in Figure 5c. According to [23], the clearance between cables is 70 mm, hence the spacing between the centers of the adjacent cables is 0.106 m. It is assumed that both circuits carry (maximum) balanced currents of 307 A_{RMS} (a correction factor has been applied for cable agglomeration) and the temperatures of all core conductors and shields are 90 °C and 80 °C, respectively. For analysis, the phases of the left-side circuit are indicated by the letters A, B and C, while the phases of the right-side circuit are indicated by the letters A′, B′ and C′.

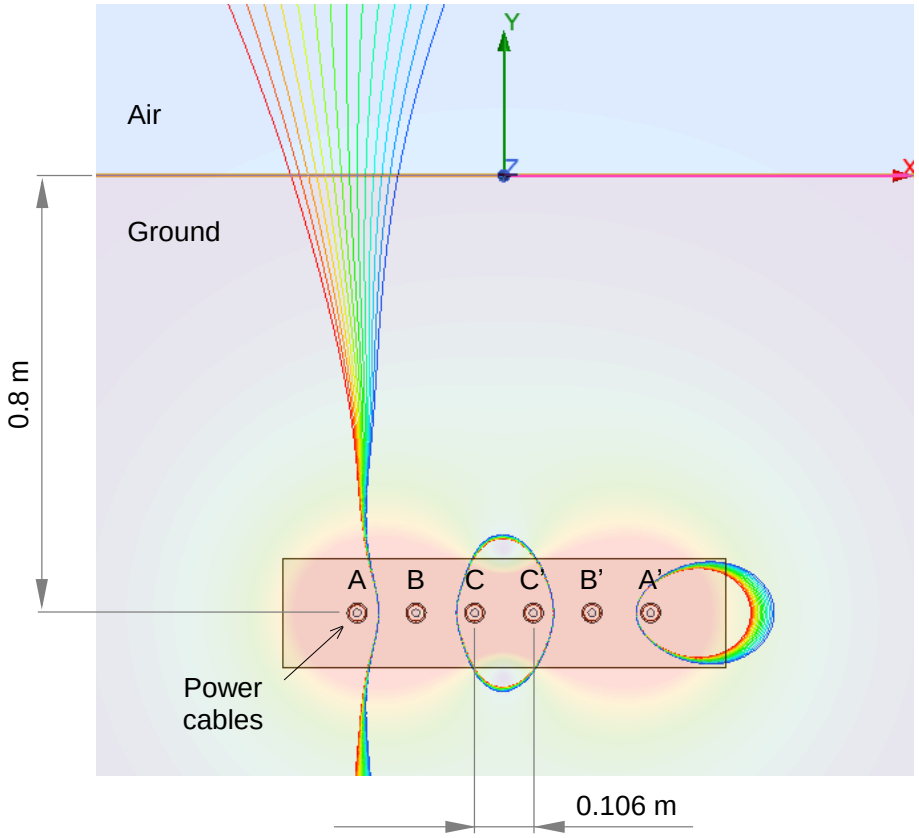

Figure 14. The 2D FEM model for computing magnetic fields from an arrangement of two adjacent three-phase power cables (with solid bonding) in flat formation.

Generally, the magnetic fields generated by two or more adjacent three-phase underground power cables will interact in a complex way, depending on their relative phase sequences and positions. Figure 15 shows the variations of RMS magnetic flux density at the height of 1 m above the ground with the change in phase sequence of the two adjacent three-phase power cables. The maximum RMS magnetic flux density, 6.633 μT, is obtained when the phases of the two circuits are in the same order, respectively ABC-A′B′C′. On the contrary, the minimum RMS magnetic flux density, 1.213 μT, is obtained when the phases of the two circuits are in reversed order, respectively ABC-C′B′A′. This confirms what some industry guidelines recommend for two parallel three-phase circuits. A 2D distribution of the instantaneous magnetic flux density around the analyzed cable arrangement is given in Figure 16.

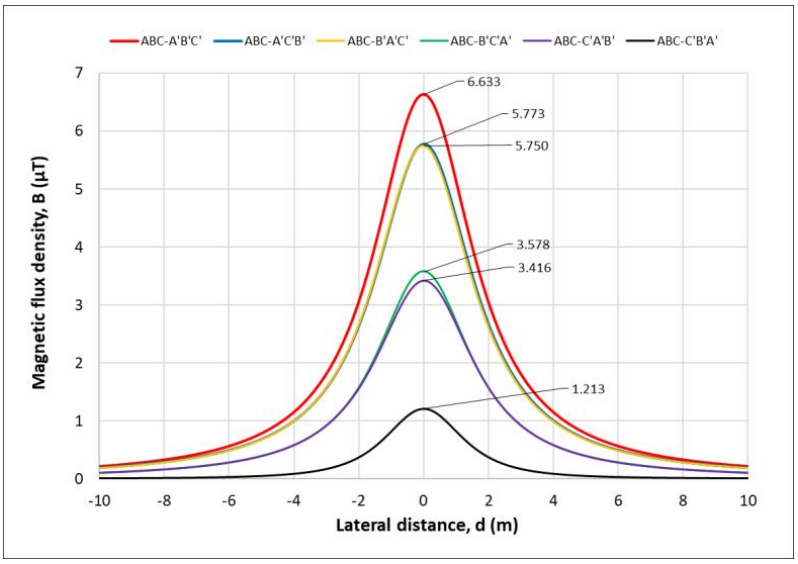

Figure 15. RMS magnetic flux density profiles at the height of 1 m above the ground as a function of phase sequence.

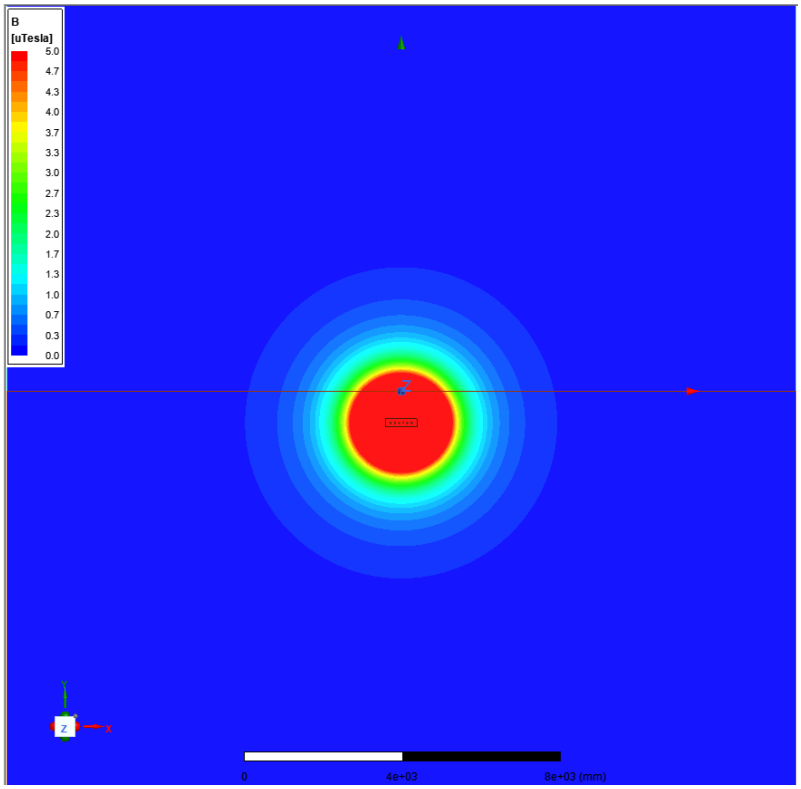

Figure 16. The 2D distribution of the (maximum) instantaneous magnetic flux density around the considered power cable arrangement.

The effect of cable shields on magnetic field reduction (at the height of 1 m above the ground) is illustrated in Table 4. The highest reduction rate, 2.16%, is obtained for the phase sequence ABC-B′A′C′, while the minimum reduction rate, 0.20%, is obtained for the phase sequence ABC-C′B′A′. However, in this case, as already presented in Figure 15, the cancelation effect in the total magnetic field created by the two circuits is maximum. At the ground level, the magnetic field reduction rate for the phase sequences ABC-B′A′C′ and ABC-C′B′A′ increases (slightly) to 2.24% and 0.33%, respectively.

Table 4. Magnetic field reduction rate due to the shields for the arrangement of two horizontally laid three-phase power cables with solid bonding.

Sequence No.	Phase Sequence		Magnetic Field Reduction Rate at 1 m above the Ground
	Left Circuit	Right Circuit	
1	ABC	A′B′C′	1.45%
2	ABC	A′C′B′	1.77%
3	ABC	B′A′C′	2.16%
4	ABC	B′C′A′	1.62%
5	ABC	C′A′B′	1.52%
6	ABC	C′B′A′	0.20%

Based on a similar analysis, numerical computations performed for an arrangement of two adjacent three-phase power cables in trefoil formation, separated by a horizontal clearance of 250 mm at the burial depth of 0.8 m [23], revealed maximum RMS magnetic flux densities (at the height of 1 m above the ground) ranging from 1.502 μT, for the phase sequence ABC-A′B′C′, to 0.517 μT, for the phase sequence ABC-B′C′A′ (optimum phasing). The highest magnetic field reduction rate, 0.50%, is obtained for the phase sequence ABC-B′A′C′, while the minimum magnetic field reduction rate, 0.40%, is obtained for the phase sequences ABC-A′B′C′ and ABC-C′A′B′. The calculated current rating of the two circuits was 284 A_{RMS}.

As we can see, the magnetic field produced by the two arrangements (for optimum phasing) is lower than the magnetic field associated with the simple cable formations discussed in the previous section. For both arrangements, the highest magnetic field reduction rate (due to induced shield currents) is not obtained for the optimum phasing.

6. Conclusions

The main achievements of this study are the development and validation of a simple and yet effective FEM model, based on ANSYS Maxwell (2D), for computing and analyzing low-frequency magnetic fields generated by three-phase underground cable systems with solid bonding. Comparisons to analytical computations based on the Biot–Savart law and the superposition principle, for both trefoil and flat formations of cables, revealed a very good agreement between results (for instance, at the standard height of 1 m above the ground, the differences in the RMS magnetic flux density at the central axis of the analyzed cable formations are only 2.36 nT and 26.49 nT, respectively).

The effect of cable shields on the magnetic field reduction has also been investigated. At maximum rated current (under balanced loading conditions), the magnetic field reduction rate due to induced shield currents is clearly better for flat cable formation, but the remaining magnetic field is significantly higher than for trefoil cable configuration. A similar situation has also been observed for an arrangement of two adjacent three-phase power cables, first laid in flat formation and then laid in trefoil formation. However, in both cases investigated here, the highest magnetic field reduction rate (due to induced shield currents) is not obtained for the optimum (low magnetic field) phasing of the two circuits.

The proposed FEM model can be adapted to calculate magnetic field distributions for any cable layout, as well as for various types of cable groups, taking into account influencing factors such as cable spacing, burial depth, phase sequence, magnetic permeability of soil. Generally, it may be used as an accurate tool for determining the worst-case magnetic field exposure levels produced by three-phase underground power cables close to the ground surface and for optimizing cable layout and location to mitigate magnetic field problems.

Author Contributions: Conceptualization, E.L., S.V. and A.S.; methodology, E.L. and S.V.; software, E.L. and S.V.; validation, E.L., S.V. and A.S.; formal analysis, E.L., S.V. and A.S.; investigation, E.L., S.V. and A.S.; resources, E.L., S.V. and A.S.; data curation, E.L., S.V. and A.S.; writing—original draft preparation, E.L., S.V. and A.S.; writing—review and editing, E.L. and A.S., visualization, E.L. and S.V.; supervision, E.L. and A.S. All authors have read and agreed to the published version of the manuscript.

Funding: This research received no external funding. The APC was funded by "Gheorghe Asachi" Technical University of Iasi.

Institutional Review Board Statement: Not applicable.

Informed Consent Statement: Not applicable.

Data Availability Statement: Not applicable.

Conflicts of Interest: The authors declare no conflict of interest.

References

1. Kljajic, D.; Djuric, N.; Bjelica, J.; Milutinov, M.; Kasas-Lazetic, K.; Antic, D. Utilization of the boundary exposure assessment for the broadband low-frequency EMF monitoring. *Meas. J.* **2017**, *100*, 110–114. [CrossRef]
2. Underground Power Cables. Available online: https://www.emfs.info/sources/underground/ (accessed on 20 April 2023).
3. Ippolito, M.G.; Puccio, A.; Ala, G.; Ganci, S. Attenuation of low frequency magnetic fields produced by HV underground power cables. In Proceedings of the 50th International Universities Power Engineering Conference (UPEC), Stoke on Trent, UK, 1–4 September 2015. [CrossRef]
4. Djekidel, R.; Mahi, D.; Hadjaj, C. Assessment of magnetic induction emission generated by an underground HV cable. *UPB Sci. Bull. C Electr. Eng. Comput. Sci.* **2016**, *78*, 179–194.
5. Kumru, C.F.; Arabul, A.Y. Numerical analysis and comparison of magnetic fields caused by constant and time varying currents in medium voltage underground cables. *Eur. J. Sci. Technol.* **2022**, *35*, 449–454. [CrossRef]
6. Ates, K.; Carlak, H.F.; Ozen, S. Magnetic field exposures due to underground power cables: A simulation study. In Proceedings of the 2nd World Congress on Electrical Engineering and Computer Systems and Science (EECSS'16), Budapest, Hungary, 16–17 August 2016. [CrossRef]
7. Abu Zarim, Z.A.; Anthony, T.M. Magnetic field simulation & measurement of underground cable system inside duct bank. In Proceedings of the 22nd International Conference on Electricity Distribution (CIRED 2013), Stockholm, Sweden, 10–13 June 2013.
8. Mahariq, I.; Beryozkina, S.; Mohammed, H.; Kurt, H. On the eddy current losses in metallic towers. *Int. J. Renew. Energy Dev.* **2020**, *9*, 1–6. [CrossRef]
9. Fernandez, E.; Patrick, J. Magnetic Fields from High Voltage Power Cables. Available online: http://elek.com.au/wp-content/uploads/2018/09/Magnetic-Fields-from-High-Voltage-Power-Cables.pdf (accessed on 20 April 2023).
10. Hernández Jiménez, V.J.; Castronuovo, E.D.; Sánchez Rodríguez-Morcillo, I. Optimal statistical calculation of underground cable bundles positions for time-varying currents. *Int. J. Electr. Power Energy Syst.* **2018**, *95*, 26–35. [CrossRef]
11. Djekidel, R.; Mahi, D.; Bessedik, S.A.; Hadjaj, C. Analysis of magnetic flux density generated by a three-phase underground power cable. In Proceedings of the 10th National Conference on High Voltage (CNHT), Algiers, Algeria, 24–26 May 2016. [CrossRef]
12. Farag, A.S.; Hossam-Eldin, A.A.; Karawia, H.M. Magnetic fields management for underground cables structures. In Proceedings of the 21st International Conference on Electricity Distribution (CIRED 2011), Frankfurt, Germany, 6–9 June 2011.
13. Rozov, V.; Grinchenko, V.; Tkachenko, O.; Yerisov, A. Analytical calculation of magnetic field shielding factor for cable line with two-point bonded shields. In Proceedings of the 2018 IEEE 17th International Conference on Mathematical Methods in Electromagnetic Theory (MMET), Kyiv, Ukraine, 2–5 July 2018. [CrossRef]
14. Riba Ruiz, J.R.; Alabern Morera, X. Effects of the circulating sheath currents in the magnetic field generated by an underground power line. In Proceedings of the International Conference on Renewable Energy and Power Quality (ICREPQ'06), Palma de Mallorca, Spain, 5–7 April 2006. [CrossRef]
15. Grinchenko, V.; Tkachenko, O.; Chunikhin, K. Magnetic field calculation of cable line with two-point bonded shields. In Proceedings of the 2017 IEEE International Young Scientists Forum on Applied Physics and Engineering (YSF), Lviv, Ukraine, 17–20 October 2017. [CrossRef]
16. Dubitsky, S.; Greshnyakov, G.; Korovkin, N. Refinement of underground power cable ampacity by multiphysics FEA simulation. *Int. J. Energy Res.* **2015**, *9*, 12–19.
17. Novák, B.; Koller, L.; Berta, I. Loss reduction in cable sheathing. In Proceedings of the International Conference on Renewable Energies and Power Quality (ICREPQ'10), Granada, Spain, 23–25 March 2010. [CrossRef]
18. Lunca, E.; Vornicu, S.; Salceanu, A. Numerical modelling of the magnetic fields generated by underground power cables with two-point bonded shields. In Proceedings of the 25th IMEKO TC4 International Symposium (IMEKO TC-4 2022), Brescia, Italy, 12–14 September 2022.
19. Vornicu, S.; Lunca, E.; Salceanu, A. Computation of the low frequency magnetic fields generated by a 12/20 kV underground power line. In Proceedings of the 2018 International Conference and Exposition on Electrical and Power Engineering (EPE), Iasi, Romania, 18–19 October 2018. [CrossRef]
20. Mahariq, I.; Erciyas, A. A spectral element method for the solution of magnetostatic fields. *Turk. J. Elec. Eng. Comp. Sci.* **2017**, *25*, 2922–2932. [CrossRef]
21. Gouda, O.E. *Environmental Impacts on Underground Power Distribution*, 1st ed.; IGI Global: Hershey, PA, USA, 2016.
22. Ocłoń, P.; Cisek, P.; Pilarczyk, M.; Taler, D. Numerical simulation of heat dissipation processes in underground power cable system situated in thermal backfill and buried in a multilayered soil. *Energy Conv. Manag.* **2015**, *95*, 352–370. [CrossRef]

23. *NTE 007/08/00*; Normative Document Regarding the Design and Execution of the Electrical Cable Networks. ANRE: Bucharest, Romania, 2008. Available online: https://anre.ro/wp-content/uploads/2023/04/ORDIN_38_NTE_007_Normativ.pdf (accessed on 20 April 2023). (In Romanian)
24. Fericean, S. *Inductive Sensors for Industrial Applications*, 1st ed.; Artech House: Norwood, NJ, USA, 2019.
25. *Maxwell Help*, Release 2021 R1; ANSYS, Inc.: Canonsburg, PA, USA, 2021.
26. *IEC 60287-1-1*; Electric Cables—Calculation of the Current Rating—Part 1-1: Current Rating Equations (100% Load Factor) and Calculation of Losses—General, Edition 2.1. International Electrotechnical Commission: Geneva, Switzerland, 2014.
27. Lunca, E.; Neagu, B.C.; Vornicu, S. Finite Element Analysis of Electromagnetic Fields Emitted by Overhead High-Voltage Power Lines. In *Numerical Methods for Energy Applications*, 1st ed.; Mahdavi Tabatabaei, N., Bizon, N., Eds.; Springer: Cham, Switzerland, 2021; Volume 1, pp. 795–821. [CrossRef]
28. International Commission on Non-Ionizing Radiation Protection. ICNIRP Guidelines for Limiting Exposure to Time-Varying Electric, Magnetic, and Electromagnetic Fields (up to 300 GHz). *Health Phys.* **1998**, *74*, 494–522.

Measurement 124 (2018) 197–204

Contents lists available at ScienceDirect

Measurement

journal homepage: www.elsevier.com/locate/measurement

Computation and analysis of the extremely low frequency electric and magnetic fields generated by two designs of 400 kV overhead transmission lines

Eduard Lunca*, Silviu Ursache, Alexandru Salceanu

Technical University of Iasi, Faculty of Electrical Engineering, 23 Prof. Dimitrie Mangeron Street, 700050 Iasi, Romania

ARTICLE INFO

Keywords:
Electric field
Magnetic field
Extremely low frequency
400 kV transmission line
2D computation

ABSTRACT

The overhead transmission lines are considered one of the major sources of electric and magnetic fields, which can induce electrical currents within the human body. In this study, the electric and magnetic fields generated by two recent designs of 400 kV transmission lines used in the Romanian power system are computed and compared to the exposure limits established by the International Commission on Non-Ionizing Radiation Protection for the general public. The computations are carried out with two dedicated software tools, called PowerMag and PowerELT, which have been developed based on a 2D quasi-static analytical approach. This approach, as well as the electric and magnetic field distributions obtained for the considered 400 kV overhead transmission lines, will be discussed in detail. To confirm the validity of the results, some comparisons to finite element computations will also be presented.

1. Introduction

Over the past 35 years, extensive research has been conducted to determine if the extremely low frequency (ELF) electric and magnetic fields like those emitted by power lines, in-house installations and household appliances can affect the human health. Researchers from different scientific disciplines conducted numerous studies regarding the potential effects of ELF fields, such as cancer in children and in adults, reproductive effects, neurological effects, cardiovascular disorders, and immunological modifications. Most notably, a weak statistical association was reported between childhood leukemia and chronic exposure to average ELF magnetic fields above 0.3–0.4 μT [1–3].

Aiming to provide protection against ELF electric and magnetic fields, a number of national and international organizations have formulated exposure guidelines. However, these guidelines are not based on a consideration of risks related to cancer or other health problems. Rather, the point of the guidelines is to make sure that the electric currents induced in the human body by such fields are not stronger than those naturally produced by the brain, nerves and heart [4].

The current consensus among various national and international scientific organizations is that there are no known adverse health consequences of exposure to ELF fields at the levels generally found in residential and occupational environments, including proximity to electric transmission and distribution facilities. Despite this fact, the public frequently expresses concern about ELF electric and magnetic fields, often in the context of locating new transmission lines [5–8].

In Romania, the highest voltage transmission lines operate at 400 kV, totalizing a length of 4703.7 km. The main objective of this study is to compute the ELF electric and magnetic fields associated with two designs of 400 kV overhead transmission lines, considered for actual developments: a 400 kV single-circuit line carried on RODELTA type towers and a 400 kV double-circuit line carried on DONAU type towers, respectively. These ELF fields will be compared to the exposure limits adopted by our country for the general public.

Like many states in the European Union (EU), Romania has transposed into national legislation the Council Recommendation 1999/519/EC of 12 July 1999 on the limitation of exposure of the general public to electromagnetic fields (0 Hz to 300 GHz), which provides reference levels derived from the guidelines published by the International Commission on Non-Ionizing Radiation Protection (ICNIRP) in 1998 [9]. Accordingly, the reference level for public exposure to 50 Hz electric fields is 5000 V/m, while the reference level for public exposure to 50 Hz magnetic fields is 100 μT. In 2010, ICNIRP issued less restrictive recommendations for the frequency range 1 Hz–100 kHz [10], but most EU countries, including Romania, still comply with the previously established limits.

The rest of the paper is structured as follows: Section 2 describes the methods adopted for the computation of the ELF electric and magnetic

* Corresponding author.
E-mail addresses: elunca@tuiasi.ro (E. Lunca), silviu_ursache@tuiasi.ro (S. Ursache), asalcean@tuiasi.ro (A. Salceanu).

https://doi.org/10.1016/j.measurement.2018.04.012
Received 29 January 2018; Received in revised form 31 March 2018; Accepted 5 April 2018
Available online 07 April 2018
0263-2241/

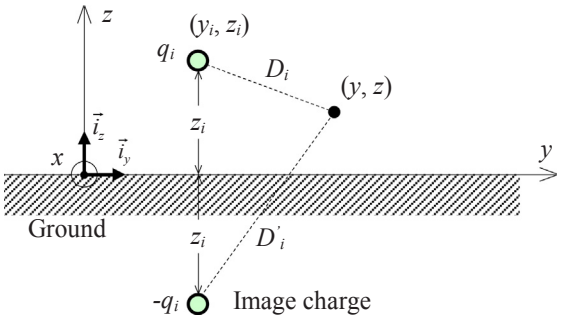

Fig. 1. Single power line conductor model for computing the electric field strength in the yz-plane.

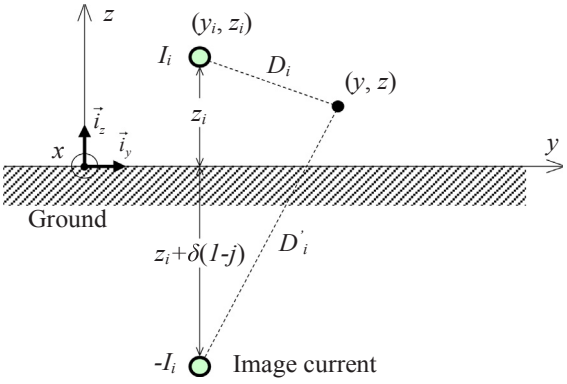

Fig. 2. Single power line conductor model for computing the magnetic flux density in the yz-plane.

Table 1
Input data for the 400 kV single-circuit transmission line using RODELTA type towers.

	y_i (m)	z_i (m)	$\underline{U}_i$ (kV)	$\underline{I}_i$ (A)
A	−7.5	h_g	231 ∠ 0°	1000 ∠ 0°
B	0.0	h_g + 11	231 ∠ −120°	1000 ∠ −120°
C	7.5	h_g	231 ∠ 120°	1000 ∠ 120°

fields generated by overhead power lines, as well as the computation (simulation) software that implements these methods; Section 3 investigates the distribution of the ELF fields around the considered 400 kV transmission lines and check the compliance with the ICNIRP guidelines; the conclusions are drawn in Section 4.

2. Materials and methods

The ELF electric and magnetic fields originating from power lines change very slowly in time, which means that they can be considered as quasi-static. Hence, these fields can be computed separately. In 2D analysis, the common practice is to assume that the power line conductors are straight horizontal wires of infinite length, parallel to a flat ground and parallel to each other. The electric field is usually computed by finding the linear charge density (electric charge per unit length) on the conductors [11–17], while the magnetic field is usually computed by applying the Biot-Savart law [16–23]. Such an approach has been adopted in our study as well.

2.1. Computation of the electric field strength

Assuming that the ground is perfectly conductive, the electric field in the vicinity of a power line conductor located at (y_i, z_i) above the ground and having a linear charge density q_i can be obtained by using

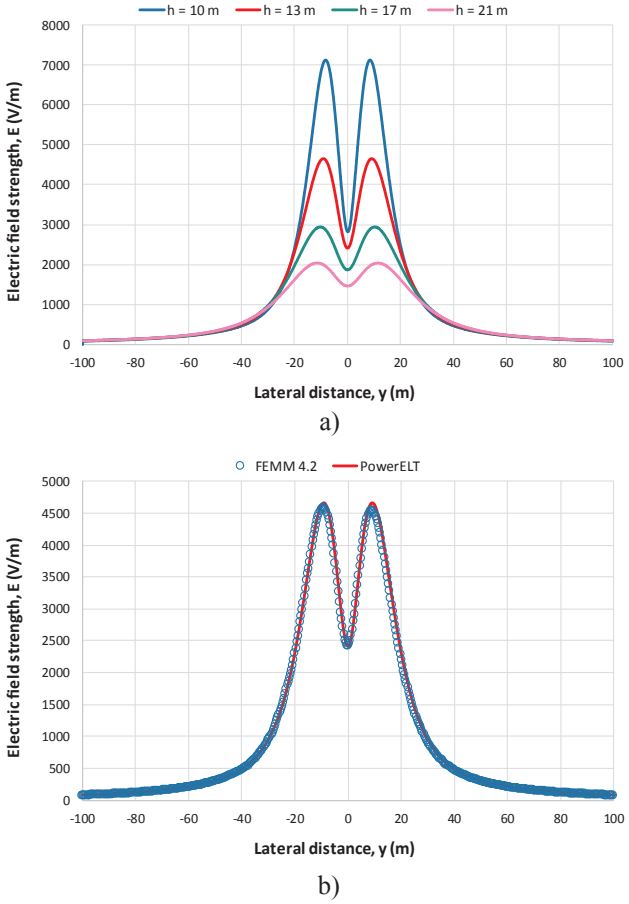

Fig. 3. Lateral profiles of the RMS electric field strength from the considered 400 kV single-circuit line, at 1 m above the ground: (a) for various ground clearances (10 m, 13 m, 17 m and 21 m); (b) comparison to FEMM 4.2 results (h_g = 13 m).

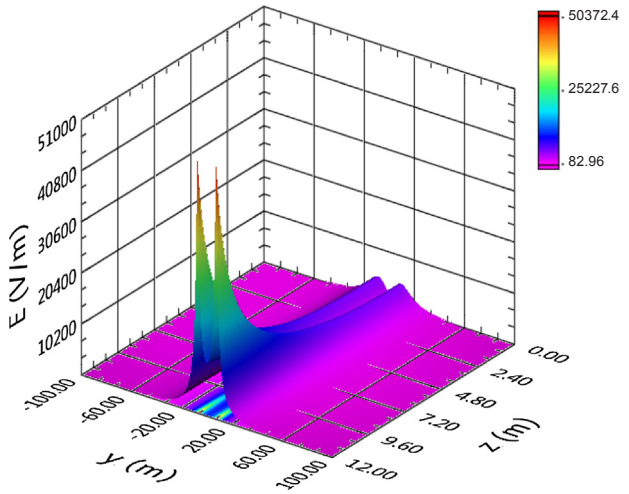

Fig. 4. The distribution of the RMS electric field strength from the considered 400 kV single-circuit line, from the ground level up to 12 m (h_g = 13 m).

the image method, as presented in Fig. 1, where $D_i = \sqrt{(y-y_i)^2 + (z-z_i)^2}$ is the distance between the conductor and the observation point (y, z) and $D'_i = \sqrt{(y-y_i)^2 + (z+z_i)^2}$ is the distance between the image conductor and the observation point (y, z). The influence of multiple conductors will be taken into account by applying the superposition principle.

In conformity with [14,17,24–27], the total electric field strength

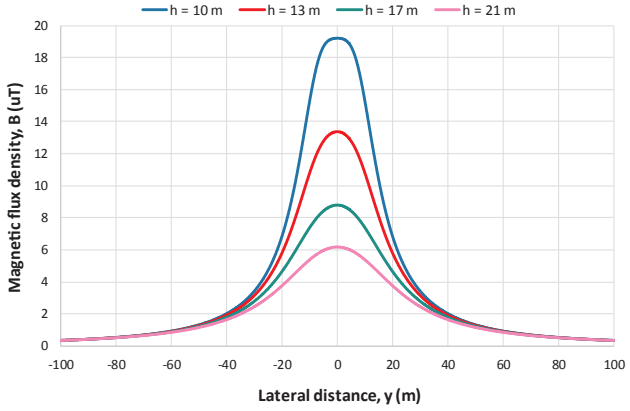

a)

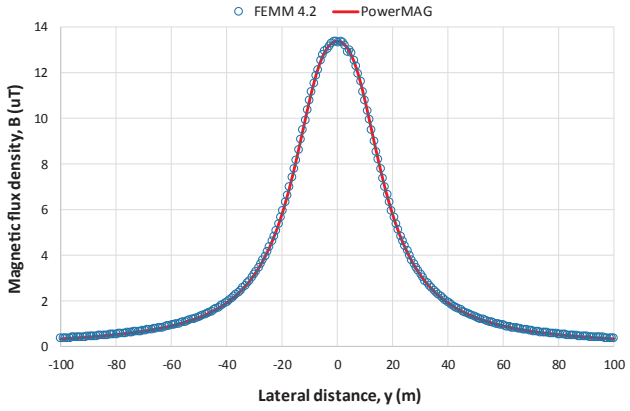

b)

Fig. 5. Lateral profiles of the RMS magnetic flux density from the considered 400 kV single-circuit line, at 1 m above the ground: (a) for various ground clearances (10 m, 13 m, 17 m and 21 m); (b) comparison to FEMM 4.2 results (h_g = 13 m).

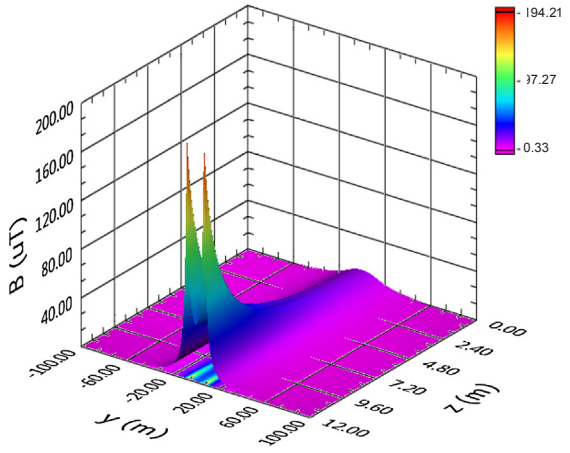

Fig. 6. The distribution of the RMS magnetic flux density from the considered 400 kV single-circuit line, from the ground level up to 12 m (h_g = 13 m).

(due to all power line conductors) can be calculated with the formula:

$$\vec{E}(y,z) = \sum_{i=1}^{n} \frac{q_i}{2\pi\varepsilon_0}\left(\frac{y-y_i}{D_i^2} - \frac{y-y_i}{D_i'^2}\right)\cdot\vec{i}_y + \sum_{i=1}^{n} \frac{q_i}{2\pi\varepsilon_0}\left(\frac{z-z_i}{D_i^2} - \frac{z+z_i}{D_i'^2}\right)\cdot\vec{i}_z \quad (1)$$

where $\varepsilon_0 = 1/(36\pi\cdot10^9)$ F/m represents the electric permittivity of the free space and n is the total number of conductors.

The charges q_i on conductors are determined from the phase voltages and Maxwell potential coefficients, using the matrix equation:

$$[q] = [p]^{-1}\cdot[V] \quad (2)$$

where $[q]$ is the column vector of the linear charge densities on each conductor, $[V]$ is the column vector of the potentials of the conductors and $[p]^{-1}$ is the inverted (symmetric) matrix of the Maxwell potential coefficients. These coefficients are calculated on the basis of line geometry and conductor radius, using the formulas:

$$p_{ii} = \frac{1}{2\pi\varepsilon_0}\ln\left(\frac{2z_i}{R_i}\right) \quad (3)$$

$$p_{ij} = \frac{1}{2\pi\varepsilon_0}\ln\left(\frac{D_{ij}'}{D_{ij}}\right) \quad (4)$$

in which R_i represents the radius of the conductor i, D_{ij} is the distance between the conductor i and the conductor j, and D'_{ij} is the distance between the conductor i and the image of the conductor j.

If the line conductors are bundled (as in the case of a 400 kV transmission line), the conductor radius R will be replaced by an equivalent radius R_{eq}, given by [28]:

$$R_{eq} = \sqrt[N]{R\cdot d^{(N-1)}} \quad (5)$$

where N is the number of individual conductors in bundle and d is the separation distance between these conductors. Eq. (5) is valid for up to three conductors per bundle.

2.2. Computation of the magnetic flux density

In 2D analysis, the ELF magnetic fields from overhead power lines can easily be computed using the Biot-Savart law, the image method and the superposition principle. According to [16–20,29], a simple, yet reasonable formula for calculating the total magnetic flux density at any observation point (y, z) in the vicinity of an overhead power line is:

$$\vec{B}(y,z) = -\sum_{i=1}^{n} \frac{\mu_0 I_i}{2\pi}\left[\frac{z-z_i}{D_i^2} - \frac{z+z_i+\delta(1-j)}{D_i'^2}\right]\cdot\vec{i}_y + \sum_{i=1}^{n} \frac{\mu_0 I_i}{2\pi}\left[\frac{y-y_i}{D_i^2} - \frac{y-y_i}{D_i'^2}\right]\cdot\vec{i}_z \quad (6)$$

where I_i represents the phase current carried by the i-th conductor – located at (y_i, z_i) with respect to the coordinate system in Fig. 2 – in the positive x-direction, $D_i = \sqrt{(y-y_i)^2 + (z-z_i)^2}$ is the distance from the observation point (y, z) to the i-th conductor, $D_i' = \sqrt{(y-y_i)^2 + (z+z_i+\delta(1-j))^2}$ is the "complex distance" from the observation point (y, z) to the i-th conductor's image, $\mu_0 = 4\pi\cdot10^{-7}$ H/m represents the magnetic permeability of the free space, and n is the total number of conductors.

As it can be seen in the simplified power line model in Fig. 2, the image current for each conductor – equal in amplitude and opposite in direction to the conductor current – is buried in the earth at the "complex depth" $z_i + \delta(1-j)$, where $\delta = 503\sqrt{\rho_g/f}$ represents the skin depth of the earth, ρ_g is the earth resistivity and f is the frequency. Since the earth resistivity typically ranges from 10 Ωm to 1000 Ωm, the image currents are normally located at hundreds of meters below the ground.

2.3. Computation software

Based on the theoretical background presented above, two computer programs have been developed to serve as tools for rapid evaluation of the ELF electric and magnetic fields around power line systems. Although most computer programs for calculating electric and magnetic fields generated by overhead power lines are developed in MATLAB, e.g. [12,23,30–33], these tools have been written in LabVIEW, which is a graphical programming environment commonly used for applications that require test, measurement and control [34–36].

Table 2
Magnetic flux densities at 1 m above the ground for different loading conditions, h_g = 13 m.

I (A)	B (μT), at distance from the centerline				
	Maximum under line	15 m	37.5 m	50 m	100 m
100	1.34	0.81	0.21	0.13	0.033
350	4.68	2.83	0.75	0.44	0.12
500	6.69	4.04	1.07	0.63	0.17
700	9.37	5.66	1.50	0.89	0.23

Table 3
Input data for the 400 kV double-circuit transmission line using DONAU type towers.

	y_i (m)	z_i (m)	$\underline{U_i}$ (kV)	$\underline{I_i}$ (A)
A	−12.625	h_g	231 ∠ 0°	1000 ∠ 0°
B	−5.625	h_g	231 ∠ −120°	1000 ∠ −120°
C	−9.125	h_g + 10.5	231 ∠ 120°	1000 ∠ 120°
A′	12.625	h_g	231 ∠ 0°	1000 ∠ 0°
B′	5.625	h_g	231 ∠ −120°	1000 ∠ −120°
C′	9.125	h_g + 10.5	231 ∠ 120°	1000 ∠ 120°

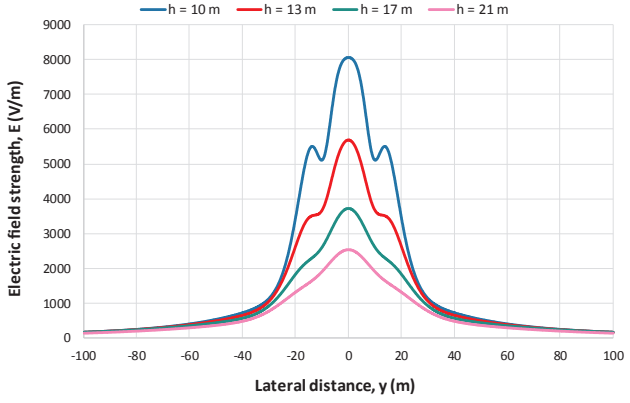

Fig. 7. Lateral profiles of the RMS electric field strength from the considered 400 kV double-circuit line, at 1 m above the ground: (a) for various ground clearances (10 m, 13 m, 17 m and 21 m); (b) comparison to FEMM 4.2 results (h_g = 13 m).

They have been designed with highly interactive user interfaces, featuring simple data entry, advanced field visualization, possibility to export data in multiple formats, etc.

The program for computing ELF magnetic fields generated by overhead power lines is called *PowerMAG* and has already been used in [29] and [37], to investigate the magnetic field exposure from typical 110 kV and 220 kV single- and double-circuit lines of the Romanian power system. The program for computing ELF electric fields generated by overhead power lines is a completely new tool, called *PowerELT*. These simulation tools are able to generate quite accurate lateral profiles (along *y*-axis) of the electric and magnetic fields at a specified height above the ground, as well as to directly map the two fields in the cross section (*yz*-plane) of the power line, between any two sets of user-defined coordinates. As with other simulation programs, the knowledge of the power line geometry, as well as of the voltage and of the current respectively (amplitude and phase), for each line conductor, is a prerequisite.

Both programs have been validated extensively, in several ways. First, they have been checked against a large number of published calculations and measurements, for specified geometries of overhead power lines, e.g. [13,16,19,24,38–43]. Second, they have been compared to similar simulation tools, based on appropriate analytical models, such as EMFACDC from ITU-T [44]. Third, they have been validated by comparison to finite element computations performed with FEMM 4.2 [45], an open source software for solving low frequency electromagnetic problems on two-dimensional planar and axisymmetric domains (see, for instance, [29] and Section 3). Overall, a very good agreement has been observed.

3. Results and discussions

As already stated, for the purpose of this study, a 400 kV single-circuit overhead transmission line with geometry imposed by RODELTA (SnR 400150) type towers and a 400 kV double-circuit overhead transmission line with geometry imposed by DONAU (Sn 400250) type towers have been considered. Both lines are equipped with three standard ACSR 300/69 mm^2 conductors per phase, symmetrically separated by a distance of 0.4 m (the radius of an individual conductor is 12.57 mm, leading to an equivalent conductor radius of 126.22 mm). The influence of the ground wire on the distribution of the electric and magnetic fields is neglected and the lines are considered exactly balanced, which means that the phase voltages and currents have equal amplitudes and 120° phase shift with respect to each other (in practice, the overhead transmission lines operate with the phases very nearly balanced). In addition, the two circuits of the 400 kV double-circuit line are assumed to carry perfectly balanced currents, but this is rare in reality.

The computation results will be presented in terms of lateral profiles of electric and magnetic field at the height of 1 m above the ground (as normally used for human exposure assessments), as well as of cross-section distributions of electric and magnetic field, from the ground level up to 1 m below the lowest conductors (better illustrate the field behavior around the transmission lines). In both representations, a lateral distance of 100 m from the centerline will be considered.

3.1. The ELF electric and magnetic fields from the 400 kV single-circuit transmission line (RODELTA)

The input data for the 400 kV single-circuit transmission line – including the geometrical parameters, as well as the phase voltages and currents (RMS value and phase) – are given in Table 1. Since both the electric and magnetic fields depend on the clearance of the line, h_g, this parameter will be taken into account by specifying four ground clearances, namely h_g = 10 m, h_g = 13 m, h_g = 17 m and h_g = 21 m. Note that "the maximum electric/magnetic field under the line" will refer to the largest field for the specified clearance, which is not necessarily on the route centerline; it is often under one of the conductor bundles.

3.1.1. The distribution of the electric field strength

Fig. 3a shows the lateral profiles of the total RMS electric field strength for all the aforementioned clearances, computed at the

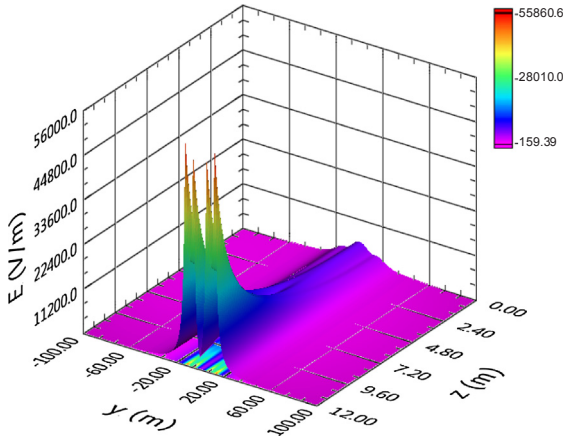

Fig. 8. The distribution of the electric field strength from the considered 400 kV double-circuit line, from the ground level up to 12 m (h_g = 13 m).

standard height of 1 m above the ground. For h_g = 10 m, a low clearance, the maximum electric field strength under the line is 7128.4 V/m, which is 1.43 times higher than the ICNIRP reference level for the general public, 5000 V/m. At 37.5 m distance from the centerline, which represents the semi-width of the safety/protection zone for 400 kV overhead transmission lines (according to the national regulations) [46], the electric field strength decreases to 535.8 V/m, representing 10.72% of the ICNIRP exposure limit. For h_g = 13 m, an intermediate clearance, the maximum electric field strength under the line is 4655.4 V/m (93.11% of the limit), while at 37.5 m distance from the centerline the field strength decreases to 567.0 V/m (11.34% of the limit). At the tower (h_g = 21 m), the maximum electric field strength under the line is 2032.1 V/m (40.64% of the exposure limit).

The dotted profile in Fig. 3b (h_g = 13 m) is included for comparison purposes only; it is generated with the FEMM 4.2 model proposed by the authors in [47], as a "current flow" (quasi-electrostatic) problem, where the transmission line is placed in the air, above a ground having zero electric potential. The RMS value of the electric field strength at each point of the lateral profile is calculated from 40 instantaneous values evenly distributed over a period of 20 ms, which have been obtained by (successively) imposing adequate instantaneous voltages on the power line conductors. As it can easily be seen from the graph, the two profiles of electric field are in very good agreement.

Fig. 4 shows the distribution of the electric field strength from the ground level up to 12 m, for h_g = 13 m. Near the ground, the highest (unperturbed) field levels occur at approximately 9 m from the centerline, where a 1.8 m-tall person could be exposed to electric field strengths as high as 4764.1 V/m (at the ground level, E = 4606.4 V/m). Starting from around 35 m from the centerline, no significant differences can be observed between the electric field values calculated at different heights. At 100 m distance from the centerline, the electric field strength is approximately 83 V/m, accounting for only 1.66% of the ICNIRP limit for the general public.

3.1.2. The distribution of the magnetic flux density

Generally, the magnetic field from a power line varies widely with time because the current in the conductors depends on the power consumption. Most of the magnetic field computations performed in this study assume a line current of 1000 A, which is rather large. However, since the magnetic flux density is directly proportional to the current in the conductors, the field levels can easily be scaled down for more typical loads.

The lateral profiles of the total RMS magnetic flux density at the height of 1 m above the ground are shown in Fig. 5a. For h_g = 10 m, the maximum magnetic flux density under the line is 19.18 μT, which is 5.21 times below the ICNIRP reference level for the general public, 100 μT. At 37.5 m distance from the centerline (at the limit of the safety/protection zone), the magnetic flux density decreases to 2.26 μT, representing 2.26% of the ICNIRP limit. For h_g = 13 m, the maximum magnetic flux density under the line is 13.39 μT (13.39% of the limit), while at 37.5 m distance from the centerline the magnetic flux density decreases to 2.14 μT (2.14% of the limit). At the tower (h_g = 21 m), the maximum magnetic flux density under the line is 6.15 μT (6.15% of the exposure limit). The distance at which B = 0.4 μT (cutoff value used in many epidemiological studies) varies only slightly with respect to h_g, from 91.6 m (h_g = 10 m) to 89.50 m (h_g = 21 m).

Fig. 5b compares the lateral profiles of the magnetic flux density (h_g = 13 m) obtained with the PowerMAG software and the FEMM 4.2 time-harmonic magnetic model proposed by the authors in [28], in which the transmission line is placed in the air, above a real ground having the conductivity $\sigma_g = 1/\rho_g$ = 0.02 S/m and the relative magnetic permeability μ_r = 1. This time, the RMS values of the magnetic flux density along the defined contour are simply calculated by dividing the peak values reported in time-harmonic regime by √2. As it can be seen from the graph, the two profiles of magnetic field are also in very good agreement.

Fig. 6 shows the distribution of the magnetic flux density from the ground level up to 12 m, for h_g = 13 m. At the centerline, for heights ranging from 0 m to 1.8 m above the ground, the magnetic flux density varies between 11.97 μT and 14.68 μT, respectively. Starting from around 55 m from the centerline, no significant differences can be observed between the magnetic flux density values calculated at different heights. At 100 m from the centerline, the magnetic flux density is approximately 0.34 μT, accounting for only 0.34% of the ICNIRP limit for the general public.

In addition to the results presented above, Table 2 gives the magnetic flux densities computed for several lower currents, at various distances from the centerline (h_g = 13 m). If considering a normal loading of 350 A–400 A, it can be concluded that the typical levels of the magnetic field under the 400 kV single-circuit line, at 1 m above the ground, are in the order of 5 μT.

3.2. The ELF electric and magnetic fields from the 400 kV double-circuit transmission line (DONAU)

The input data for the 400 kV double-circuit transmission line are given in Table 3. The electric and magnetic field computations are performed under the same conditions as for the single-circuit line.

3.2.1. The distribution of the electric field strength

The lateral profiles of the RMS electric field strength from the double-circuit line are shown in Fig. 7a. The maximum electric field strength under the line exceeds the ICNIRP limit for both h_g = 10 m (E_{max} = 8053.3 V/m, 1.61 times higher than the limit) and h_g = 13 m (E_{max} = 5679.1 V/m, 1.14 times higher than the limit); outside the safety/protection zone, the electric field strength accounts for less than 785.3 V/m (15.71% of the limit) and 704.3 V/m (14.09% of the limit), respectively. At the tower (h_g = 21 m), the maximum field strength under the double-circuit line is 2547.5 V/m (50.95% of the limit).

As with the single-circuit line, Fig. 7b compares the lateral profiles of the electric field strength generated with PowerELT and FEMM 4.2, for the same ground clearance (h_g = 13 m). Also this time, a very good agreement between results can be observed.

The distribution of the electric field strength in the cross-section of the 400 kV double-circuit line is presented in Fig. 8 (h_g = 13 m). At the centerline, for heights ranging from 0 m to 1.8 m above the ground, the electric field strength varies between 5648.5 V/m and 5747.3 V/m, respectively. Starting from around 50 m from the centerline, the differences between the electric field values calculated at various heights may be considered negligible. At 100 m from the centerline, the electric field strength is approximately 161 V/m (3.22% of the ICNIRP limit), double the value obtained for the single-circuit line.

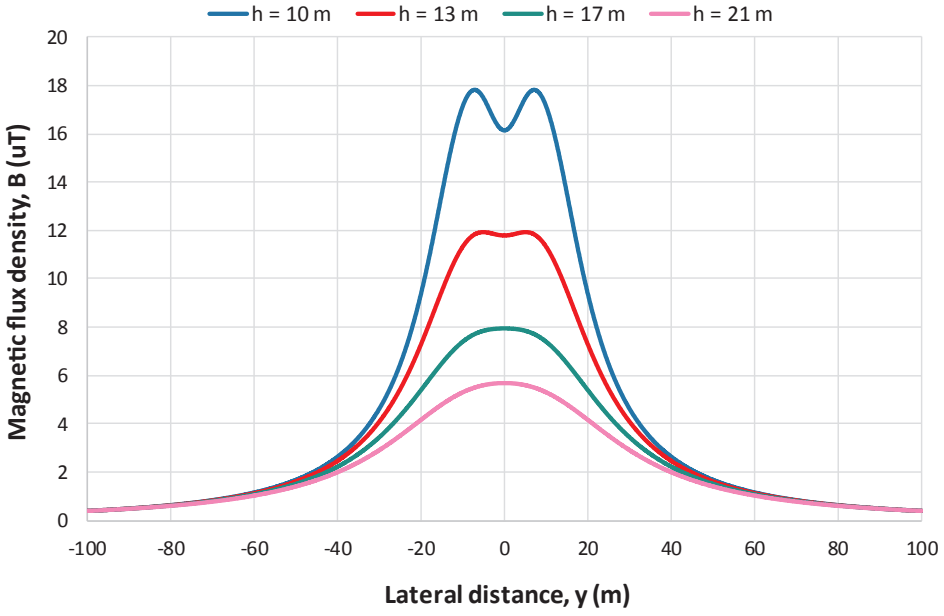

a)

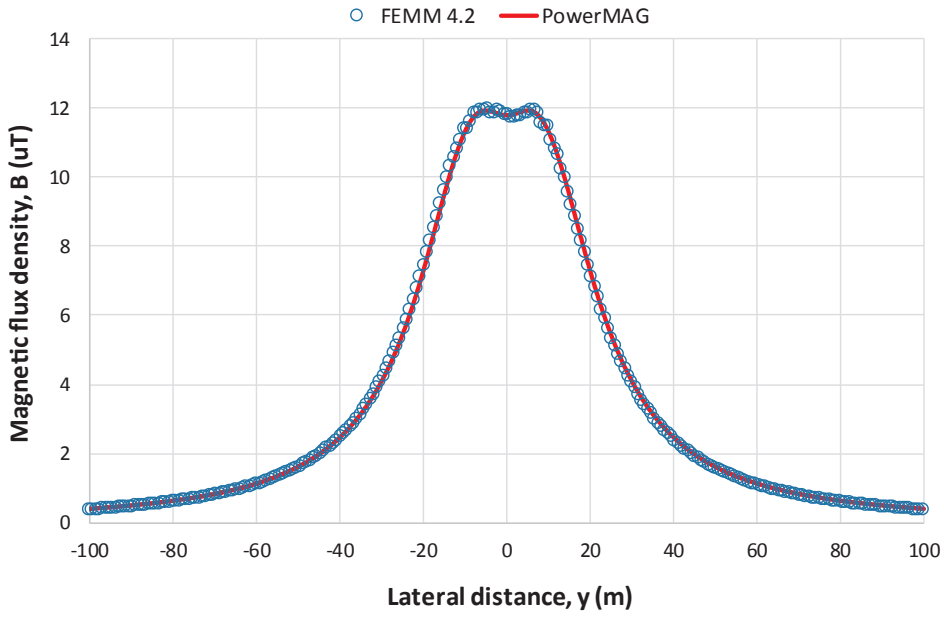

b)

Fig. 9. Lateral profiles of the RMS magnetic flux density from the considered 400 kV double-circuit line, at 1 m above the ground: (a) for various ground clearances (10 m, 13 m, 17 m and 21 m); (b) comparison to FEMM 4.2 results (h_g = 13 m).

3.2.2. The distribution of the magnetic flux density

The lateral profiles of the RMS magnetic flux density from the double-circuit line are shown in Fig. 9a (I = 1000 A). For h_g = 10 m, the maximum magnetic flux density under the line is 17.80 μT (5.62 times below the ICNIRP reference level), slightly lower than for the single-circuit line. At the limit of the safety/protection zone (37.5 m distance from the centerline), the magnetic flux density is 3.02 μT (3.02% of the ICNIRP limit), slightly higher than for the single-circuit line. For h_g = 13 m, the maximum magnetic flux density under the line is 11.92 μT (11.92% of the limit), while at 37.5 m distance from the centerline the magnetic flux density decreases to 2.79 μT (2.79% of the limit). At the tower (h_g = 21 m), the maximum magnetic flux density under the line is 5.70 μT (5.70% of the exposure limit). The distance at which B = 0.4 μT varies from 102.8 m (for h_g = 10 m) to 100.5 m (for h_g = 21 m).

Similarly, Fig. 9b compares the lateral profiles of the magnetic flux density obtained with PowerMAG and FEMM 4.2, for the ground clearance h_g = 13 m. A very good agreement between results can also be observed.

The distribution of the magnetic flux density in the cross-section of the 400 kV double-circuit line is presented in Fig. 10 (h_g = 13 m). At a distance of 5.8 m from the centerline, a 1.8 m-tall person could be exposed to magnetic fields as high as 13.13 μT (at the ground level, B = 10.62 μT). Starting from around 65 m from the centerline, the differences between the magnetic flux density values calculated at various heights may be considered negligible. At 100 m from the

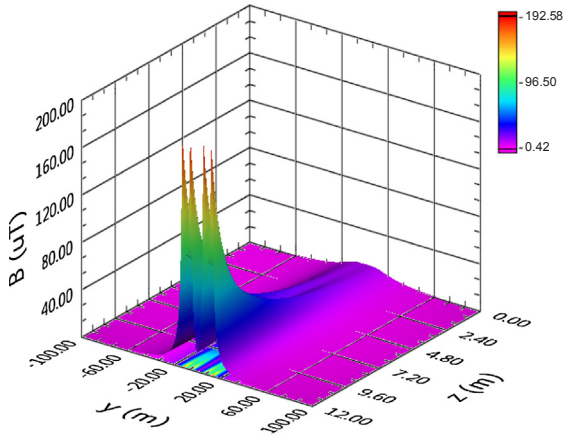

Fig. 10. The distribution of the magnetic flux density from the considered 400 kV double-circuit line, from the ground level up to 12 m (h_g = 13 m).

Table 4
Magnetic flux densities at 1 m above the ground for different loading conditions, h_g = 13 m.

I (A)	*B* (μT), at distance from the centerline				
	Maximum under line	15 m	37.5 m	50 m	100 m
100	1.19	0.95	0.28	0.16	0.042
350	4.17	3.32	0.98	0.57	0.15
500	5.96	4.75	1.40	0.82	0.21
700	8.35	6.65	1.95	1.14	0.29

centerline, the magnetic flux density is approximately 0.42 μT, accounting for only 0.42% of the ICNIRP limit for the general public.

Table 4 gives magnetic flux densities computed for currents lower than 1000 A (h_g = 13 m). As already observed, for the same current, the magnetic field levels under the 400 kV double-circuit line are lower than those under the single-circuit line (the magnetic field generated by the single-circuit line falls below the magnetic field generated by the double-circuit line at a distance of about 9 m from the centerline). If considering a normal loading of 350 A–400 A, the typical levels of the magnetic field under the 400 kV double-circuit line, at 1 m above the ground, are in the order of 4.5 μT.

4. Conclusions

The paper has been focused on the computation and analysis of the ELF electric and magnetic fields associated with two recent designs of 400 kV overhead transmission lines – single-circuit and double-circuit, respectively – used in Romania. The computations have been carried out with two original programs based on a 2D quasi-static analytical approach and have been rigorously verified by numerical modeling based on the finite element method. According to these computations, the electric field strength at 1 m above the ground exceeds the ICNIRP limit for the general public under both transmission lines, with the highest value, 8053.3 V/m (1.61 times higher than the limit), being registered under the 400 kV double-circuit line. On the contrary, the highest magnetic flux density is registered under the 400 kV single-circuit line, 19.18 μT (for phase currents of 1000 A), but this value is more than 5 times below the ICNIRP limit for the general public. Outside the safety/protection zone (37.5 m from the centerline), the electric and magnetic fields originating from the double-circuit line are slightly higher than those generated by the single-circuit line, not exceeding 785.3 V/m (15.71% of the limit) and 3.02 μT (3.02% of the limit), respectively. The calculated ELF fields are similar to those reported for other types of 400 kV transmission lines.

References

[1] A. Ahlbom, N. Day, M. Feychting, et al., A pooled analysis of magnetic fields and childhood leukaemia, Br. J. Cancer 83 (5) (2000) 692–698.
[2] S. Greenland, A.R. Sheppard, W.T. Kaune, et al., A pooled analysis of magnetic fields, wire codes, and childhood leukemia, Childhood Leukemia-EMF Study Group, Epidemiology 11 (6) (2000) 624–634.
[3] L. Kheifets, A. Ahlbom, C.M. Crespi, et al., Pooled analysis of recent studies on magnetic fields and childhood leukemia, Br. J. Cancer 103 (7) (2010) 1128–1135.
[4] Health Canada, Electric and magnetic fields from power lines and electrical appliances, November 2012. http://publications.gc.ca/site/eng/431220/publication.html (accessed 14 November 2017).
[5] Exponent, Research on Extremely Low Frequency Electric and Magnetic Fields from Alternating Current Transmission Lines — Summary Evaluation of the Evidence, Report prepared for Manitoba Hydro Transmission Planning & Design, 15 May 2015. https://www.hydro.mb.ca/projects/mb_mn_transmission/pdfs/eis/mmtp_tdr_socioec_low_frequency_electric_study.pdf (accessed 14 November 2017).
[6] J.T. Porsius, L. Claassen, T. Smid, et al., Health responses to a new high-voltage power line route: design of a quasi-experimental prospective field study in the Netherlands, BMC Public Health 14 (237) (2014) 1–12 (accessed 14 November 2017).
[7] J.T. Porsius, L. Claassen, T. Smid, et al., Symptom reporting after the introduction of a new high-voltage power line: A prospective field study, Environ. Res. 138 (2015) 112–117.
[8] R.K.Z. Sahbudin, S.A. Fauzi, S. Hitam, M. Mokhtar, Investigation of electrical potential and electromagnetic field for overhead high voltage power lines in Malaysia, J. Appl. Sci. 10 (22) (2010) 2862–2868.
[9] International Commission on Non-Ionizing Radiation Protection, ICNIRP guidelines for limiting exposure to time-varying electric, magnetic, and electromagnetic fields (up to 300 GHz), Health Phys. 74 (4) (1998) 494–522.
[10] International Commission on Non-Ionizing Radiation Protection, Guidelines for limiting exposure to time-varying electric and magnetic fields (1 Hz – 100 kHz), Health Phys. 99 (6) (2000) 818–836.
[11] R.G. Olsen, Calculation of ELF Electric and Magnetic Fields in Air: Synopsis, in: EMF Engineering Review Symposium, Charleston, April 28–29, 1998. ftp://ftp.emf-data.org/pub/emf-data/symposium98/topic-06a-synopsis.pdf (accessed 14 November 2017).
[12] A. Marincu, M. Gregonici, S. Musuroi, The electromagnetic field around a high voltage 400 kV electrical overhead line and the influence on the biological systems, Facta Universitatis, Series: Electronics and Energetics 18 (1) (2005) 105–111.
[13] M. Milutinov, A. Juhas, M. Prša, Electric field strength and polarization of multi three-phase power lines, in: 8th International Conference on Applied Electromagnetics, Niš, September 3–5, 2007, pp. 1–4.
[14] S.M. Elhabashi, J.E. Ehtaiba, Electric fields intensity around the new 400 kV power transmission lines in Libya, in: 6th WSEAS International Conference on Circuits, Systems, Electronics, Control and Signal Processing, Cairo, December 29–31, 2007, pp. 390–398.
[15] S.S. Razavipour, M. Jahangiri, H. Sadeghipoor, Electrical field around the overhead transmission lines, World Acad. Sci. Eng. Technol. 6 (2) (2012) 168–171.
[16] M. Milutinov, A. Juhas, M. Prša, Electromagnetic field underneath overhead high voltage power line, in: 4th International Conference on Engineering Technologies, Novi Sad, April 28–30, 2009, pp. 1–5.
[17] E. Lunca, S. Ursache, A. Salceanu, Characterization of the electric and magnetic field exposure from a 400 kV overhead power transmission line in Romania, in: 22nd IMEKO TC4 International Symposium and 20th International Workshop on ADC Modelling and Testing, Iasi, September 14–15, 2017, pp. 1–5.
[18] R.G. Olsen, D. Deno, R.S. Baishiki, et al., Magnetic fields from electric power lines: theory and comparison to measurements, IEEE Trans. Power Delivery 3 (4) (1988) 2127–2136.
[19] R.G. Olsen, Electromagnetic fields from power lines, in: IEEE International Symposium on EMC, Dallas, 1993, pp. 138–143.
[20] P.S. Maruvada, A. Turgeon, D.L. Goulet, Study of population exposure to magnetic fields due to secondary utilization of transmission line corridors, IEEE Trans. Power Delivery 10 (3) (1995) 1541–1548.
[21] G. Filippopoulos, D.K. Tsanakas, Analytical calculation of the magnetic field produced by electric power lines, IEEE Trans. Power Delivery 20 (2) (2005) 1474–1482.
[22] F. Moro, R. Turri, Fast analytical computation of power-line magnetic fields by complex vector method, IEEE Trans. Power Delivery 23 (2) (2008) 1042–1048.
[23] I.N. Ztoupis, I.F. Gonos, I.A. Stathopulos, Calculation of power frequency fields from high voltage overhead lines in residential areas, in: 18th International Symposium on High Voltage Engineering, Seoul, August 25–30, 2013, pp. 61–66.
[24] M.S.H. Al Salameh, M.A.S. Hassouna, Arranging overhead power line conductors using swarm intelligence technique to minimize electromagnetic fields, Prog. Electromagn. Res. B 26 (2010) 213–236.
[25] M. Ouadah, M. Zergoug, Analysis of the electromagnetic interferences between overhead power lines and buried pipelines, Med. J. Model. Simul. 1 (1) (2014) 13–23.
[26] S.F. Braicu, L. Czumbil, D. Stet, D.D. Micu, Evaluation of the electric and magnetic field near high voltage power lines, in: 5th International Conference on Advancements of Medicine and Health Care through Technology, Cluj-Napoca, October 12–15, 2016, pp. 141–146.
[27] H.Y. Chen, C.K. Peng, D.P. Lin, Currents induced in the human body by ELF electric fields inside houses located under power lines, Radio Sci. 34 (4) (1999) 1013–1024.
[28] L.L. Grigsby, Electric Power Generation, Transmission, and Distribution, third ed.,

CRC Press, Boca Raton, 2012.
[29] E. Lunca, M. Istrate, A. Salceanu, Comparative analysis of the extremely low-frequency magnetic field exposure from overhead power lines, Environ. Eng. Manage. J. 12 (6) (2013) 1145–1152.
[30] O.E. Gouda, G.M. Amer, W.A. Salem, Computational aspects of electromagnetic fields near H.V. transmission lines, Energy Power Eng. 1 (2) (2009) 65–71.
[31] J.S. Santos, C.E.A. Henrique, R.M. Silva, C.A.C. Tenorio, A Matlab based software for measurement of transmission line fields, in: 2011 IEEE Power & Energy Society Innovative Smart Grid Technologies Conference, Anaheim, January 17–19, 2011, pp. 1–6.
[32] M. Nafar, Magnetic field calculation around 230 kV bundled transmission lines, Int. J. Eng. Innovation Res. 2 (6) (2013) 463–466.
[33] L. Xiao, K.E Holbert, Development of software for calculating electromagnetic fields near power lines, in: North American Power Symposium (NAPS 2014), Pullman, September 7–9, 2014, pp. 1–6.
[34] E. Lunca, S. Ursache, O. Neacsu, Graphical programming tools for electrical engineering higher education, Int. J. Online Eng. 7 (1) (2011) 19–24.
[35] E. Lunca, S. Ursache, A. Salceanu, LabVIEW interactive simulations for electromagnetic compatibility, Int. J. Online Eng. 8 (2) (2012) 11–14.
[36] P. Arpaia, E. De Matteis, V. Inglese, Software for measurement automation: A review of the state of the art, Measurement 66 (2015) 10–25.
[37] E. Lunca, M. Istrate, A. Salceanu, S. Tibuliac, Computation of the magnetic field exposure from 110 kV overhead power lines, in: 7th International Conference on Electrical and Power Engineering, Iasi, October 25–27, 2012, pp. 628–631.
[38] S. Vujević, P. Sarajčev, D. Lovrić, Computation of the power line electric and magnetic fields, in: 17th Telecommunications Forum, Belgrade, November 24–26, 2009, pp. 875–878.
[39] S. Vujević, D. Lovrić, T. Modrić, 2D computation and measurement of electric and magnetic fields of overhead electric power lines, in: Joint 3rd International Workshop on Nonlinear Dynamics and Synchronization (INDS'11) & 16th International Symposium on Theoretical Electrical Engineering (ISTET'11), Klagenfurt, July 25–27, 2011, pp. 1–6.
[40] K. Ellithy, S. Al-Suwaidi, H. Elsayed, Measuring human exposure to magnetic fields near EHV 400 KV GIS substation and power lines in state of Qatar, in: North American Power Symposium (NAPS 2011), Boston, August 4–6, 2011, pp. 1–6.
[41] T.R.O. Almeida, C.F.R. Lemos Antunes, Magnetic field computation due to high voltage power lines using easyMAG, in: IX Congreso Hispano-Luso de Ingeniería Eléctrica, Marbella, June 30 and July 1–2, 2005, pp. 1–5.
[42] K. Deželak, G. Štumberger, F. Jakl, Arrangements of overhead power line conductors related to the electromagnetic field limits, in: 2010 Modern Electric Power Systems Conference, Wroclaw, September 20–22, 2010, pp. 1–6.
[43] M. Kokoruš, S. Delic, A. Mujezinovic, M. Muratovic, A. Caršimamovic, Analysis of the possible solutions for the reduction of electric and magnetic fields near 400 kV overhead transmission lines, Environmental Impact II (WIT Transactions on Ecology and The Environment), WIT Press, Southampton, 2014, pp. 225–236.
[44] ITU-T, Evaluation techniques and working procedures for compliance with exposure limits of network operator personnel to power-frequency electromagnetic fields, Recommendation ITU-T K.90, May 29, 2012. http://handle.itu.int/11.1002/1000/11633 (accessed 10 January 2018).
[45] D. Meeker, Finite Element Method Magnetics, Version 4.2, User's Manual, October 25, 2015. http://www.femm.info/Archives/doc/manual42.pdf (accessed 10 January 2018).
[46] ANRE, NTE 003/04/00 – Normative document regarding the construction of aerial electricity lines with voltages above 1000 V (in Romanian), 2014. https://ro.scribd.com/doc/207928871/Normativ-NTE-003-04-00-Constructia-Liniilor-Aeriene-Cu-Tensiuni-de-Peste-1000V (accessed 10 January 2018).
[47] A. Salceanu, E. Lunca, M. Paulet, Affordable evaluation of low frequency electric fields from the standpoint of Directive 2013/35/EU, ACTA IMEKO 6 (4) (2017) 37–45.

Environmental Engineering and Management Journal *December 2016, Vol.15, No. 12, 2753-2759*
http://omicron.ch.tuiasi.ro/EEMJ/

"Gheorghe Asachi" Technical University of Iasi, Romania

ASSESSMENT OF RADIOFREQUENCY EXPOSURE LEVELS GENERATED BY WIMAX BASE STATIONS

Eduard Lunca*, Silviu Ursache, Andrei Salceanu

Technical University of Iasi, Faculty of Electrical Engineering, 21 Prof. Dimitrie Mangeron Street, 700050 Iasi, Romania

Abstract

The radiofrequency (RF) electromagnetic fields represent one of the most common and fast growing environmental influences, raising concerns about possible effects on human health. The fact that there is a continuous change and an emergence of RF communication technologies on the market also leads to a change of daily RF exposure levels for the general public. In such a context, the main objective of our study is to assess the RF exposure originating from the emerging Worldwide Interoperability for Microwave Access (WiMAX) technology, which was only rarely investigated. By adopting a frequency-selective technique, in-situ far-field measurements were conducted at 41 locations in the urban environment of the Iasi city, Romania, and its rural neighborhood, focusing on the coverage area of several WiMAX base stations operating in the licensed 3.5 GHz and 3.7 GHz frequency bands. The WiMAX downlink signals measured at each location were recorded, extrapolated to maximum data traffic and compared to the reference level specified by the International Commission on Non-Ionizing Radiation Protection (ICNIRP) for the general public. The highest electric field level was found to be 0.201 V/m (corresponding to only 0.33% of the ICNIRP exposure limit), while 86.9% of the individual measurements were below 0.1% of the limit. As for the total WiMAX exposure, it varied from 0.008 V/m (0.012% of the limit) to 0.201 V/m (0.33% of the limit), with a median value of 0.059 V/m (0.096% of the limit). No significant differences were observed between the results taken at urban and rural locations.

Key words: base station, frequency-selective measurements, radiofrequency exposure, Worldwide Interoperability for Microwave Access

Received: August, 2015; Revised final: December, 2016; Accepted: December, 2016

1. Introduction

WiMAX, acronym for Worldwide Interoperability for Microwave Access, is a wireless communication technology based on the IEEE 802.16 standard family. It is designed to provide high-speed 4G mobile broadband services, while replacing broadband cable networks like DSL (Digital Subscriber Line). WiMAX is currently embedded in hundreds of devices including PC cards, USB dongles, MiFi routers, laptops and cellular phones, being available to more than 1 billion people in about 150 countries (Morley and Parker, 2014).

To meet the requirements of different types of access, two versions of WiMAX were defined: similar to Wi-Fi, *Fixed WiMAX* (IEEE 802.16d-2004) is able to provide Internet access to fixed locations, but the coverage is significantly larger, up to 50 km; *Mobile WiMAX* (IEEE 802.16e-2005) is designed to support portability and mobility, covering a distance from 5 to 15 km (Hamodi et al., 2013; Meinel and Sack, 2012). There is no uniform global licensed spectrum for WiMAX, but most deployments focus on the 2.3 GHz, 2.5 GHz and 3.5 GHz frequency bands (ICNIRP, 2008; Rohde & Schwarz, 2015). A typical WiMAX base station transmits at power levels of approximately +43 dBm (20 W), while the user equipment transmits at approximately +23 dBm (200 mW) (Poulin, 2008; Sanders et al., 2012).

In the context of public exposure to RF electromagnetic fields generated by WiMAX

* Author to whom all correspondence should be addressed: e-mail: elunca@tuiasi.ro; Phone:+40 232278680/1246; Fax:+40 232237627

systems, only a small number of studies were conducted or reported. For instance, by using a frequency-selective measurement method, Bornkessel et al. (2009a, 2009b) assessed the RF exposure from several WiMAX base stations operating in the licensed 3.5 GHz and the license-free 5 GHz frequency bands, in Germany, and compared the measured levels to those generated by UMTS (Universal Mobile Telecommunications System) base stations on the same roof or in near vicinity. Similarly, Joseph et al. (2012) performed narrowband measurements of the RF electromagnetic fields from base stations of emerging wireless technologies, including WiMAX (if present), at 311 locations spread over 35 areas, in three European countries (Belgium, The Netherlands and Sweden). A different approach was adopted by Barbiroli et al. (2009), who analyzed the impact of WiMAX installations by means of simulation tools, in conformity with the information given by Italian operators. Another study was conducted by Singh (2012), who performed calculations of effective isotropic radiated power (*EIRP*) to determine compliance distances for various types of base stations, also including WiMAX, at a typical site for wireless communications in Bharat Nagar, Ludhiana, India.

According to all these studies, the emissions caused by WiMAX are well bellow the ICNIRP guidelines (ICNIRP, 1998), and generally lower than the emissions associated with other concurrent technologies, such as GSM (Global System for Mobile Communications) and UMTS. However, as very limited information is available on the public exposure to WiMAX transmitters, further research is necessary for a better knowledge of the typical RF exposure levels associated with this emerging technology.

At present, in Romania, three nationwide WiMAX networks operate in the licensed 3.5 GHz (3410 MHz – 3600 MHz) and 3.7 GHz (3600 MHz – 3800 MHz) frequency bands. One of them – the largest Mobile WiMAX network in Europe, at its launch in 2011 (Airspan, 2011) – is serving to connect government, public safety, border patrol and administrative offices across the country, while the other two – a Fixed WiMAX network operated by Radiocom, whose first part was officially launched in November 2010 (TeleGeography, 2010), and a Mobile WiMAX network operated by 2K Telecom, since March 2011 (2K Telecom, 2011) – are commercial, providing broadband services to business, public and residential customers. Thus, the main objective of our study was to investigate the RF exposure levels originating from these networks, by conducting an electric field (*E*-field) survey in the vicinity of several WiMAX base stations installed in the urban environment of the Iasi city and its rural neighborhood.

In order to achieve this goal, special attention was first paid to establish a frequency-selective technique – based on a handheld RF spectrum analyzer in conjunction with a calibrated log-periodic antenna – able to perform reliable in-situ measurements of the present WiMAX downlink signals. The survey itself was conducted during June 2015, over 41 locations (24 urban and 17 rural), where public has frequent access. All measured *E*-field levels were recorded, extrapolated to maximum data traffic and compared to the reference levels recommended by ICNIRP for the general public (ICNIRP, 1998), which are identical to the exposure limits adopted by Romania (GO, 2006).

Further, the paper is organized as follows: Section 2 describes in detail the measurement methodology for WiMAX exposure; Section 3 investigates the distribution of the measured RF exposure levels and check compliance with the ICNIRP guidelines; the conclusions are drawn in Section 4.

2. Measurement methodology

The WiMAX transmissions mainly involve the OFDM (Orthogonal Frequency Division Multiplexing) modulation scheme, which divides the occupied bandwidth into a large number of closely spaced subcarriers and transmits data in parallel streams. Currently, Fixed WiMAX has channel bandwidths of 3.5 MHz, 5 MHz, 7 MHz and 10 MHz, and supports both TDD (Time Division Duplexing) and FDD (Frequency Division Duplexing) transmission modes. Mobile WiMAX has channel bandwidths of 5 MHz, 7 MHz, 8.75 MHz and 10 MHz, and supports only TDD. Note that in FDD systems the uplink and the downlink transmissions occur simultaneously, on separate frequency channels, while in TDD systems the uplink and the downlink transmissions share the same frequency channel, but are scheduled in different time slots (Keysight Technologies, 2014; National Instruments, 2015).

All WiMAX networks operating in our country use TDD. During the survey period, a total number of 7 Mobile WiMAX (IEEE 802.16e-2005) channels were present at the considered locations. The bandwidth of four channels was 10 MHz, while the bandwidth of the other three was 5 MHz. For each signal, the duration of a TDD frame was 5 ms, a widely accepted value.

To perform in-situ measurements of these WiMAX signals, we adopted a frequency-domain technique based on a portable SPECTRAN HF-60105 V4 spectrum analyzer (1 MHz – 9.4 GHz, typ. accuracy ±1 dB) in conjunction with a wideband HyperLOG 60100 antenna (680 MHz – 10 GHz), both from Aaronia (Fig. 1a). In addition to a great mobility and a high sensitivity, this setup has also the advantage that the spectrum analyzer (SA) can directly display the electric field strength, *E*, in units of V/m.

The frequency-dependent antenna factor and losses in the connecting cable, which normally must be added to the voltage reading of the SA in order to obtain the *E*-field level (David et al., 2009; Lunca et

al., 2013), are already stored in the instrument, so this operation is automatically performed.

(a)

(b)

Fig. 1. Measurement approach used for WiMAX exposure: a) instrumentation; b) example of measurement in the vicinity of a base station in the urban area

The optimum SA's settings used for assessing the WiMAX exposure were derived as follows: RMS (Root Mean Square) detector, as the OFDM modulated signals from WiMAX base stations feature a high peak-to-average ratio, approximately 10 dB; resolution bandwidth *RBW* = 5 MHz, the maximum usable *RBW* with respect to the determined channel bandwidths; video bandwidth *VBW* = 50 MHz (FULL), at least three times higher the *RBW* (Lunca et al., 2012); sample time *SpTime* = 5 ms, equal to the duration of a TDD frame (leading to a sweep time of about 250 ms, as the SA's display has 51 horizontal pixels); frequency span of 30 MHz, with the center frequency of the SA equal to the center frequency (CF) of the WiMAX signal, previously determined by closely investigating all available channels.

At each location, the measurement approach was to record the maximum *E*-field strength for every present signal, not only from the designated WiMAX transmitter, in order to calculate a worst-case exposure level. Thus, measurements were taken with the spectrum analyzer operating in Maximum Hold mode and smoothly moving the hand-held antenna in all directions, while varying its polarization and tilt, up to about 2 m above the ground (Fig. 1b), until a maximum signal level was observed (Lunca et al., 2014). The duration of each measurement was at least one minute. During the measurements, a minimum distance of 1 m was maintained between any object and the antenna.

However, as the TDD base stations do not transmit continuously, the *E*-field readings taken in Max Hold mode will overestimate the RF exposure for maximum data traffic. For this reason, all measurement results were extrapolated to maximum duty cycle, by using the equation (CCR, 2014):

$$E_{\text{max duty cycle}} = \sqrt{t_{\text{DL subframe}} / t_{frame}} \cdot E_{\text{meas Max Hold}} \quad (1)$$

where $t_{\text{DL subframe}}$ is the duration of the downlink subframe, t_{frame} is the duration of the full TDD frame and $E_{\text{meas Max Hold}}$ is the RMS level measured in Max Hold mode.

Generally, the ratio $t_{\text{DL subframe}}/t_{\text{frame}}$ may be available from the network operator or it may be determined by inspection in the time domain. In our case, because no specific data were available from operators, we considered the maximum ratio observed during multiple measurements for each TDD channel, which was in the range of 0.56 ÷ 0.6. Hence, for a maximum duty cycle of 0.6, the extrapolation factor was 0.75.

After data processing, the total WiMAX exposure at each location was evaluated with the formula (Lewicki and Scharoch, 2015):

$$E = \sqrt{\sum_{i=1}^{n} E_i^2} < E_{\text{lim}} \quad (2)$$

where E_i is the field strength due to a particular signal and E_{lim} is the ICNIRP exposure limit for the WiMAX frequency range, i.e. 61 V/m.

3. Results and discussion

By using the methodology presented above, a total of 122 measurements were conducted – as already mentioned – at 41 locations, 24 urban and 17 rural, focusing on the coverage of several WiMAX base stations. All measurements were taken outdoor, under typical far-field exposure conditions, starting from about 30 m away from the closest base station. The downlink signals found at each location were recorded, extrapolated to maximum data traffic and compared to the ICNIRP reference level for the general public, as illustrated in Table 1.

An overview of the frequency range from 3400 MHz to 3800 MHz is given in Fig. 2. The two

spectra, which highlight the WiMAX signals in Table 1 at a particular location, are recorded by using the MCS Spectrum Analyzer Software from Aaronia, during a few minutes. The number of WiMAX downlink signals simultaneously present at a location varied from 1 to 6 in the urban environment and from 1 to 3 in the rural environment. At several sites, the WiMAX emissions were below the sensitivity of the measuring equipment.

The highest extrapolated *E*-field level observed during the entire survey was 0.201 V/m, at the frequency of 3445 MHz. This value, which represents 0.33% of the exposure limit, was measured in the vicinity of a WiMAX tower located in the rural area, at a distance of about 225 m. The highest *E*-field level recorded in the urban environment was 0.125 V/m, at the frequency of 3473 MHz. This value, which represents 0.2% of the exposure limit, was measured in front of a WiMAX antenna installed on the roof of a 13-floor building, at a distance of about 180 m. Other measurements performed closer to these transmitters revealed lower exposure levels, which means that the distance is not a determinative factor for quantifying the RF exposure in the immediate vicinity of WiMAX antennas, but rather the orientation to the main beam and site conditions (the buildings, trees and other structures in the vicinity greatly attenuate the generated RF fields).

Table 1. Example of measurement results for WiMAX exposure

Center frequency (MHz)	***$E_{meas\ Max\ Hold}$ (V/m)***	***Extrapolation factor***	***$E_{max\ traffic}$ (V/m)***	***ICNIRP limit (V/m)***	***Percentage of ICNIRP limit***
3445	0.020	0.75	0.0150	61	0.02
3473	0.026	0.75	0.0195	61	0.03
3572	0.067	0.75	0.0503	61	0.08
3697.5	0.097	0.75	0.0728	61	0.12
Total field strength			0.0918		0.15

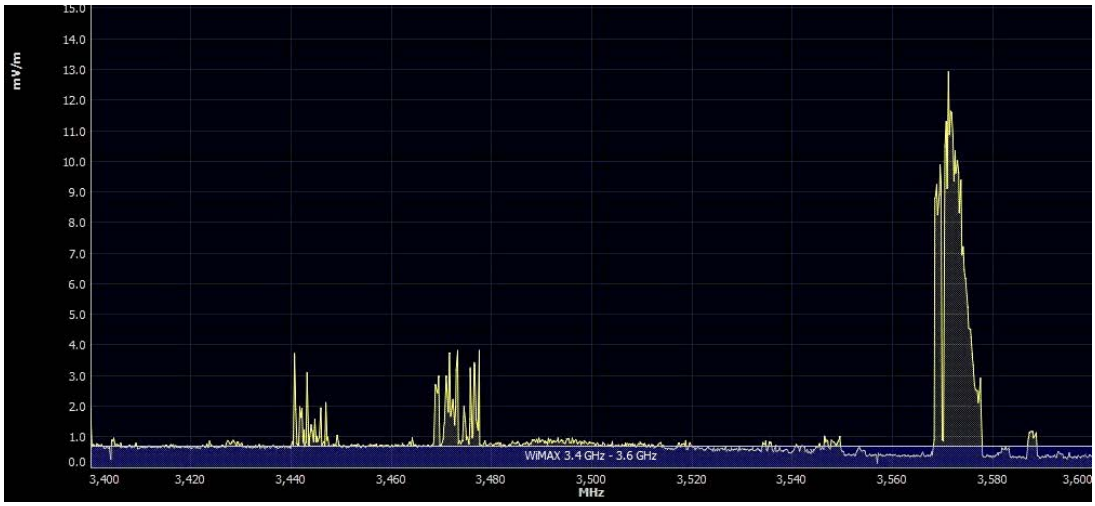

(a)

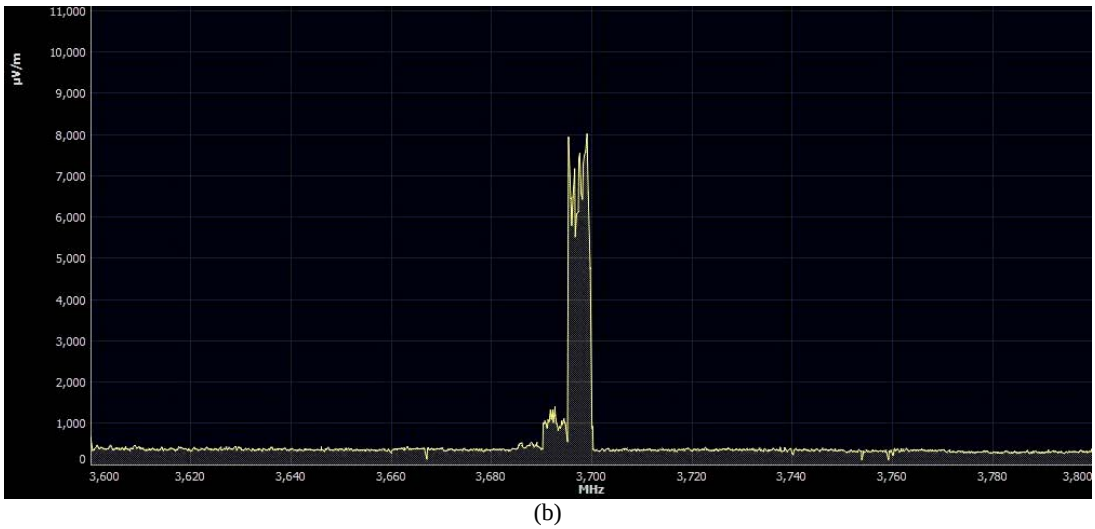

(b)

Fig. 2. WiMAX emissions in the frequency range: a) from 3400 MHz to 3600 MHz; b) from 3600 MHz to 3800 MHz

Fig. 3 illustrates the distribution of all individual readings taken in the survey. The overwhelming majority of the measurement results are below 0.05 V/m (corresponding to 0.08% of the field strength limit), with a median value of 0.0165 V/m (0.027% of the limit) and an average value of 0.0302 V/m (0.05% of the limit). In percentage terms, 86.9% of the extrapolated *E*-field values are below 0.1% of the ICNIRP exposure limit, while 9.84% of the individual readings fall between 0.1% and 0.2% of the limit. As for the power density, calculated as S (W/m^2) = E^2/Z_0, where Z_0 = 377 Ω represents the characteristic impedance of the free space (ICNIRP, 1998; Sandu et al., 2011), 86.9% of the individual results are below 0.0001% of the ICNIRP reference level, i.e. 10 W/m^2.

Fig. 4 compares, as percentage of the ICNIRP exposure limit, the total *E*-field levels (due to all WiMAX signals) and the highest *E*-field levels (due to the strongest WiMAX signal) registered at the 41 locations. As it can easily be seen, the largest contribution to the total WiMAX exposure comes from the highest WiMAX signal present at each location, which usually originated from the designated base station. The minimum value for the total WiMAX exposure is 0.008 V/m or 0.012% of the ICNIRP limit, while the maximum value is 0.201 V/m or 0.33% of the ICNIRP limit, corresponding to a single WiMAX signal. The median and average values for the total WiMAX exposure are 0.059 V/m (0.096% of the ICNIRP limit) and 0.063 V/m (0.103% of the ICNIRP limit) respectively. As for the location type, urban or rural, the medians are practically identical to the general value, while the averages are 0.060 V/m (0.098% of the limit) and 0.068 V/m (0.112% of the limit) respectively.

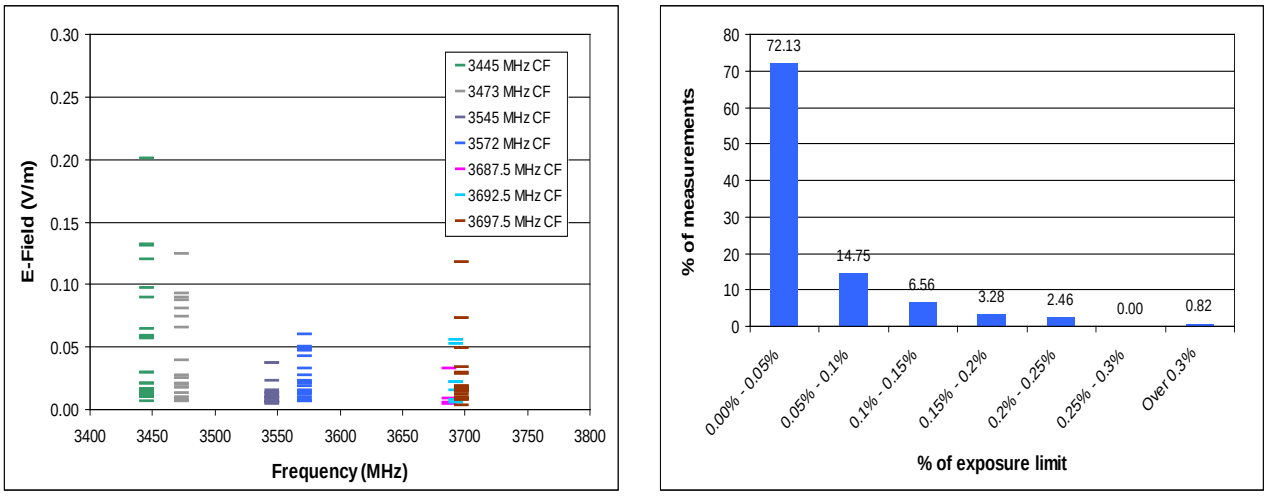

(a) (b)

Fig. 3. Overview of the recorded data: a) maximum WiMAX exposure levels within specific sub-bands; b) percentage of measurements as percentage of ICNIRP field strength exposure limit

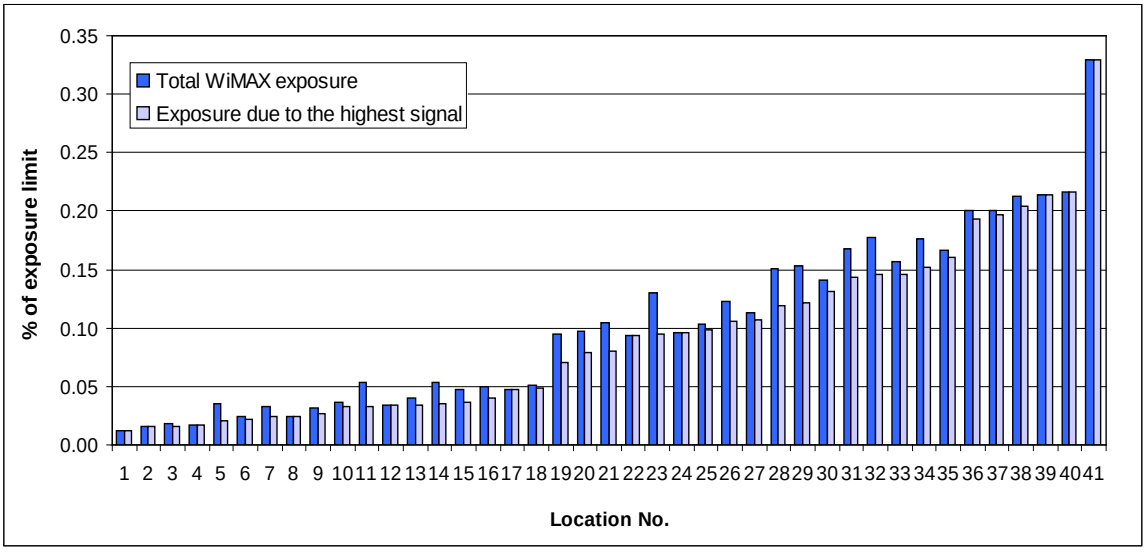

Fig. 4. Total and highest *E*-field levels registered at 41 urban and rural locations, as percentage of the ICNIRP exposure limit

Compared to the results of the studies cited in Section 2, the results reported above seem to be quite similar. For instance, Bornkessel et al. (2009a, 2009b) stated that the majority of the measurement results extrapolated to maximum data traffic were below 0.02 V/m (0.03% of the exposure limit), with a maximum value of 0.84 V/m (1.38% of the exposure limit), which is 4.18 times higher than our maximum level, and a median value of about 0.017 V/m (0.28% of the exposure limit), which is very close to ours. Joseph et al. (2012) reported a "maximal value" for the WiMAX exposure of 0.28 V/m and an average value of 0.07 V/m. This is also close to our average value for the total WiMAX exposure at the 41 locations, 0.063 V/m.

4. Conclusions and further work

At present, very limited information is available on the general public exposure to WiMAX base station radiation. The objective of this study was to establish a measurement methodology for WiMAX exposure, to collect measurement data and to assess worst-case exposure levels from a number of WiMAX base stations operating in Iasi, Romania. All measurements were taken outdoor, at 41 locations, during June 2015. The total WiMAX exposure at each location was clearly dominated by the WiMAX emissions from the designated base station, ranging from 0.008 V/m (0.012% of the ICNIRP field strength limit) to 0.201 V/m (0.33% of this limit). All of the registered WiMAX exposure levels are therefore considerably below the ICNIRP guidelines and are not considered hazardous. The main findings of this study are consistent of those of other few studies carried out in some European countries.

Further researches will be focused on investigations at more locations, as well as on the influence of different factors on the WiMAX exposure. For example, one limitation of our study was that most of the measurements were taken at the ground level, so further investigations might be necessary to determine if the height differences could significantly affect the RF exposure from WiMAX transmitters, especially in tall neighboring buildings. Another research issue will be to determine the contribution of WiMAX to the total RF exposure and to compare the WiMAX exposure levels to those generated by other concurrent technologies, such as 4G LTE (Long Term Evolution).

References

2K Telecom, (2011), The first 4G WiMAX Network in Romania, Newsletter (in Romanian), Sept. 2011, On line at: http://www.2ktelecom.ro/view_newsletter.php?nl_id=3&n_id=22#22.

Airspan, (2011), Airspan 4G Solution Deployed by STS Romania for Nationwide Mobile WiMAX Network, Article, 22 Mar. 2011, On line at: http://www.airspan.com/airspan-4g-solution-deployed-by-sts-romania-for-nationwide-mobile-wimax-network/.

Barbiroli M., Carciofi C., Guiducci D., Violanti S., (2009), *Evaluation of Exposure Levels Generated by WiMAX Systems*, 2009 International Conference on Electromagnetics in Advanced Applications, ICEAA '09, 865-868.

Bornkessel C., Schubert M., Wuschek M., (2009a), *Determination of General Public Exposure to WiMAX Base Stations*, 20th International Zurich Symposium on Electromagnetic Compatibility, 333-336.

Bornkessel C., Schubert M., Wuschek M., (2009b), *Determination of the public's exposure caused by WiMAX transmitters*, BfS Pogram (Germany), Project ID 1821, Final report – Part I (in German), On line at: http://www.emf-forschungsprogramm.de/akt_emf_forschung.html/dosi_HF_001.html.

CCR, (2014), Programme of Measurement of Non-Ionising Radiation Emissions. Methodology for the Conduct of Surveys to Measure Non-Ionizing Electromagnetic Radiation from Transmitter Sites, Document No. 08/51R2, On line at: http://www.comreg.ie/_fileupload/publications/ComReg0851R2.pdf.

David V., Nica I., Salceanu A., (2009), Survey of electromagnetic environment due to mobile communications, *Environmental Engineering and Management Journal*, **8**, 341-345.

GO, (2006), Governmental Order no. 1193/2006 on the approval of the norms on the limitation of exposure of the general public to electromagnetic fields (0 Hz to 300 GHz), *Romanian Official Monitor*, no. 895 from 3rd of November, 2006.

Hamodi J., Salah K., Thool R., (2013), Evaluating the Performance of IPTV over Fixed WiMAX, *International Journal of Computer Applications*, **84**, 35-43.

ICNIRP, (1998), Guidelines for limiting exposure to time-varying electric, magnetic and electromagnetic fields (up to 300 GHz), *Health Physics*, **74**, 494-522.

ICNIRP, (2008), ICNIRP statement on EMF-emitting new technologies, *Health Physics*, **94**, 376-392.

Joseph W., Verloock L., Goeminne F., Vermeeren G., Martens L., (2012), Assessment of RF exposures from emerging wireless communication technologies in different environments, *Health Physics*, **102**, 161-172.

Keysight Technologies, (2014), Mobile WiMAX™ PHY Layer (RF). Operation and Measurement, Application Note, On line at: http://literature.cdn.keysight.com/litweb/pdf/5989-8309EN.pdf.

Lewicki F., Scharoch P., (2015), An efficient method of EM field modification around transmitting stations, *Journal of Microwaves, Optoelectronics and Electromagnetic Applications*, **14**, 121-131.

Lunca E., David V., Salceanu A., Cretescu I., (2012), Assessing the human exposure due to wireless local area networks in office environments, *Environmental Engineering and Management Journal*, **11**, 385-391.

Lunca E., Salceanu A., Ursache S., (2013), Automated Measurement and Monitoring of the Electromagnetic Fields from GSM Systems, *Journal of Clean Energy Technologies*, **1**, 174-177.

Lunca E., Damian C., Salceanu A., (2014), *EMF Exposure Measurements on 4G/LTE Mobile Communication Networks*, 2014 International Conference and

Exposition on Electrical and Power Engineering, 545-548.

Meinel C., Sack H., (2012), *Internetworking: Technological Foundations and Applications*, Springer, Berlin.

Morley D., Parker C.S., (2014), *Understanding Computers: Today and Tomorrow, Comprehensive*, 15th Edition, Cengage Learning, Stamford.

National Instruments, (2015), Introduction to WiMAX Transmitter Measurements, Tutorial, On line at: http://www.ni.com/tutorial/8976/en/.

Poulin D., (2008), How much transmit power do WiMAX nets need?, EE Times, On line at: http://www.eetimes.com/document.asp?doc_id=1271732&page_number=1.

Rohde & Schwarz, (2015), WiMAX Technology, On line at: http://www.rohde-schwarz.com/en/technologies/cellular/wimax/wimax-technology/wimax-technology_54000.html.

Sanders F.H., Sole R.L., Caroll J.E., Secrest G.S., Lynn Allmon T., (2012), Analysis and Resolution of RF Interference to Radars Operating in the Band 2700–2900 MHz from Broadband Communication Transmitters, NTIA Technical Report TR-13-490, U.S. Dept. of Commerce, On line at: https://www.its.bldrdoc.gov/publications/2684.aspx.

Sandu D.D., Balmus S.B., Gasner P., Avadanei O.G., (2011), Electromagnetic map in the 75 – 3000 MHz band in certain areas of Iasi city – protection standards, *Environmental Engineering and Management Journal*, **10**, 471-479.

Singh R.K., (2012), Assessment of electromagnetic radiation from base station antennas, *Indian Journal of Radio & Space Physics*, **41**, 557-565.

TeleGeography, (2010), SNR aims for 10,000 WiMAX customers by end 2011, 25 Nov. 2010, On line at: https://www.telegeography.com/products/commsupdate/articles/2010/11/25/snr-aims-for-10000-wimax-customers-by-end-2011/.

Environmental Engineering and Management Journal

June 2013, Vol.12, No. 6, 1145-1151
http://omicron.ch.tuiasi.ro/EEMJ/

"Gheorghe Asachi" Technical University of Iasi, Romania

COMPARATIVE ANALYSIS OF THE EXTREMELY LOW-FREQUENCY MAGNETIC FIELD EXPOSURE FROM OVERHEAD POWER LINES

Eduard Lunca*, Marcel Istrate, Alexandru Salceanu

"Gheorghe Asachi" Technical University of Iasi, Faculty of Electrical Engineering, 21-23 Prof. Dr. Doc. D. Mangeron Street, 700050 Iasi, Romania

Abstract

The aim of this study is to carry out a theoretical investigation of the extremely low-frequency (ELF) magnetic fields produced by typical configurations of overhead power lines of the Romanian power grid. The computation of the magnetic flux density is achieved by the following two approaches: i) using an interactive LabVIEW program developed on fundamental formulas and ii) by numerical modeling with FEMM 4.2, a software package based on the finite-element method. Analytical results are then compared to numerical results and both are checked against national and international ELF exposure guidelines.

Key words: analytical computation, finite-element method, magnetic fields, overhead power lines

Received: February 2013; Revised final: June, 2013; Accepted: June, 2013

1. Introduction

During the past three decades, there has been a growing concern about possible adverse health effects of the exposure to extremely low-frequency (ELF) magnetic fields, mainly arising from the transmission and use of electrical energy at the power frequencies of 50/60 Hz. Since 1979, when an epidemiological study reported – for the first time – an association between childhood leukemia and magnetic fields from high-current electrical wiring configurations (Nica et al., 2011; Wertheimer and Leeper, 1979), numerous studies have examined this potential link.

In 2001, largely based on two pooled analyses suggesting that the chronic exposure to average ELF magnetic fields higher than 0.3 - 0.4 μT might double the risk of childhood leukemia (Ahlbom et al., 2000; Greenland et al., 2000), the International Agency for Research on Cancer (IARC) has classified the ELF magnetic fields as "possibly carcinogenic for humans", Group 2B (IARC, 2002). This means that the evidence in humans is credible, but alternative explanations, such as chance, bias, etc., can not be ruled out.

To ensure protection to electromagnetic fields (EMFs), a number of national and international organizations have formulated guidelines. Like many European countries, Romania has transposed into national legislation the Council Recommendation of 12 July 1999 on the limitation of exposure of the general public to electromagnetic fields (0 Hz to 300 GHz) and the Directive 2004/40/EC of the European Parliament and of the Council of 29 April 2004 on the minimum health and safety requirements regarding the exposure of workers to the risks arising from physical agents (electromagnetic fields).

Both documents provide reference levels derived from the guidelines published by the International Commission on Non-Ionizing Radiation Protection (ICNIRP) in 1998, which – in the case of the power-frequency magnetic fields – are 100 μT, for general public exposure, and 500 μT, for occupational exposure (ICNIRP, 1998). In 2010, ICNIRP published less restrictive recommendations for the

*Author to whom all correspondence should be addressed: E-mail: elunca@ee.tuiasi.ro; Phone:+ 40.232.278680/1246; Fax:+ 40.232.237627

frequency range 1 Hz - 100 kHz (ICNIRP, 2010), but the European Union, including our country, still follows the more conservative limits established previously.

At present, since the possible health impact of exposure to ELF magnetic fields from power-frequency systems remains somewhat controversial, the evaluation of these fields – to demonstrate compliance with adequate EMF exposure guidelines – is a very important issue (Buzdugan and Balan, 2011; Neacsu et al., 2012). In the following, by using two distinct computation methods (analytical and numerical), special emphasis will be placed on the characterization of the exposure levels generated by common configurations of 110 kV and 220 kV overhead power lines of the Romanian power grid.

2. Computation methods

Generally, the electric and magnetic fields from overhead power lines can be efficiently predicted with both analytical (Kaune and Zaffanella, 1992; Olsen et al., 1995; Filippopoulos and Tsanakas, 2005; Moro and Turri, 2008) and numerical (El-Fouly et al., 2005; Hameyer et al., 1995; Tupsie et al., 2010) methods. The computation models adopted for this study – one in each category – are briefly presented in the subsequent two sections.

2.1. Analytical method

The distribution of the magnetic fields from overhead power lines has been the subject of many calculation approaches, with different degrees of approximation. Typically, there are two simplifying assumptions, namely that the conductors are straight horizontal lines parallel to a flat conductive earth and parallel with each other, and that the influence of the transmission towers is negligible. Thus, if the currents in all the conductors are known, it is possible to calculate the magnetic flux density at any point (y, z) in the vicinity of the line by using the equation (Milutinov et al., 2009):

$$\vec{B}(y,z) = -\sum_{i=1}^{n} \frac{\mu_0 I_i}{2\pi}\left[\frac{z-z_i}{r_{ci}^2} - \frac{z+z_i+\delta(1-j)}{r_{ii}^2}\right]\vec{i}_y + \sum_{i=1}^{n} \frac{\mu_0 I_i}{2\pi}\left[\frac{y-y_i}{r_{ci}^2} - \frac{z-z_i}{r_{ii}^2}\right]\vec{i}_z \quad (1)$$

where:

I_i represents the r.m.s. current carried by the i^{th} conductor, located at (y_i, z_i) with respect to the coordinate system in the positive x-direction (Fig. 1);

$r_{ci} = \sqrt{(y-y_i)^2 + (z-z_i)^2}$ is the distance from the observation point (y, z) to the i^{th} conductor;

$r_{ii} = \sqrt{(y-y_i)^2 + (z+z_i+\delta(1-j))^2}$ is the *complex distance* from the observation point (y, z) to the i^{th} conductor's image, and n is the total number of conductors.

Note that the image current for each conductor, equal in magnitude and opposite in direction to the conductor current is buried in the earth at the *complex depth* $z_i + \delta(1-j)$, where $\delta = 503\sqrt{\rho_g / f}$ represents the skin depth of the earth, ρ_g is the earth resistivity and f is the frequency.

Since the typical values of the earth resistivity range from 10 Ωm to 1000 Ωm, the image currents are normally located at hundreds of meters below the ground (Olsen et al., 1988).

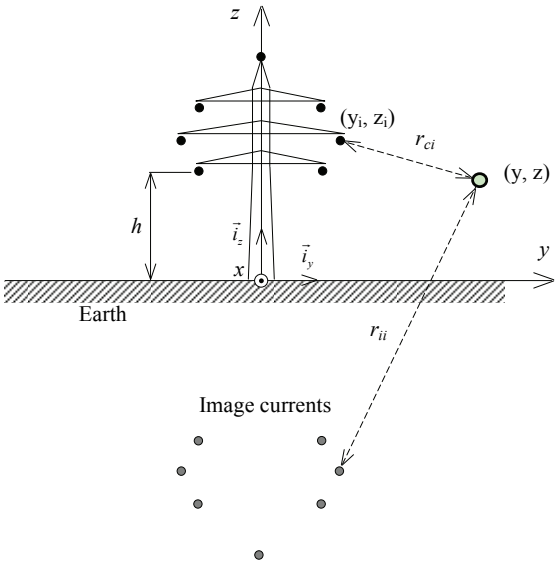

Fig. 1. Cross section of a double-circuit power line

To quickly compute ELF magnetic fields from different configurations of overhead power lines, this mathematical model has been incorporated into an interactive LabVIEW program, called PowerMAG (Lunca et al., 2012). As with other similar tools, the knowledge of the power line geometry and of the current (amplitude and phase) for each line conductor is a prerequisite. By simply specifying a computation height above the ground, the program can then generate quite accurate lateral profiles (along y-axis) for both the total magnetic flux density, B, and its transversal components, B_y and B_z.

Another useful feature of the program is the capability to directly map the magnetic field in the cross section (yz-plane) of the power line, between any two sets of user-defined coordinates.

2.2. Numerical method

As already stated, the ELF magnetic fields from overhead power lines can also be estimated by using popular numerical methods, such as the finite-element method (FEM). Thus, for confirming the validity of the results generated by PowerMAG, a number of simulations have been conducted with David Meeker's FEMM 4.2, a free FEM-based

software package that addresses some limiting cases of Maxwell's equations for solving two-dimensional, low-frequency electromagnetic problems.

Fig. 2 conceptually illustrates the FEMM model used for these simulations. The power line – in this case, a 220 kV double-circuit line – is placed in the air, above a real earth having the conductivity $\sigma_g = 1/\rho_g = 0.05$ S/m and the relative magnetic permeability $\mu_r = 1$.

The active conductors of the two circuits are steel-reinforced aluminum conductors with standard sections of 450/75 mm^2, excited by sinusoidal currents of 50 Hz frequency. The boundary conditions applied here assume that the magnetic vector potential along the boundary is zero ($A = 0$). In addition, the air region surrounding the conductors is taken large enough to neglect the side effects (only a part of the model is shown in Fig. 2.

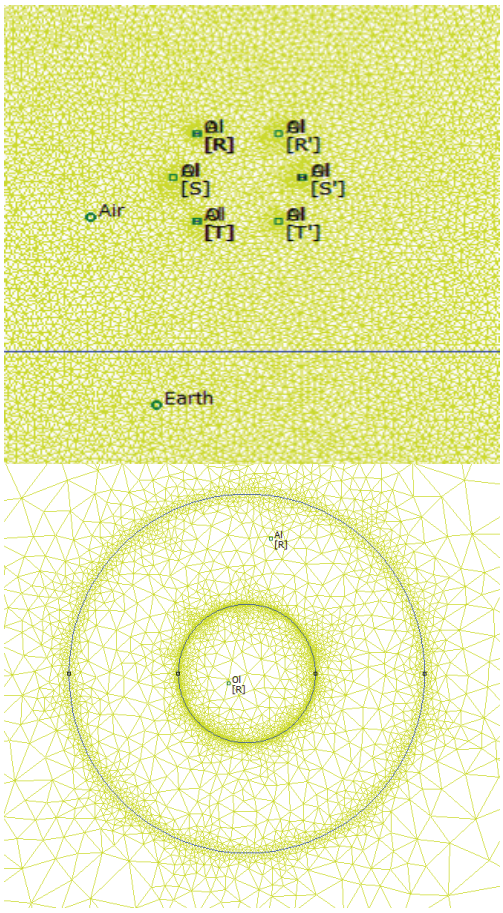

Fig. 2. FEMM model for a 220 kV overhead power line: cross section and zoom on a conductor

It should be mentioned that, in FEMM 4.2, all the quantities computed in time harmonic regime are defined in terms of peak values. For this reason, to directly compare such results to those generated by PowerMAG, which are in terms of r.m.s. values, additional processing has been carried out in MS Excel. Only the 2D distributions of magnetic flux density will be presented in the form generated with FEMM 4.2.

3. Results and discussion

All the computations performed in this study assume configurations of 110 kV and 220 kV double-circuit lines (DCLs), similar to that in Fig. 1. The influence of the grounding wire on the distribution of the magnetic field is neglected and the currents within each circuit are considered exactly balanced, which means that they have equal amplitudes and 120º-phase shift with respect to each other (in practice, the overhead transmission lines operate with the phases very nearly balanced).

In addition, the two circuits are assumed to carry perfectly balanced currents, but this is rarely found in reality. However, because the importance of the balance of current between the two circuits depends on the relative phasing of the line, both "untransposed" (U) and "transposed" (T) phasing are considered. With transposed phasing, the magnetic fields from the two circuits will partially cancel each other and, if the currents are equal, the cancellation will be good, resulting in a reduction of the magnetic field, especially at larger distances. With untransposed phasing, the magnetic fields from the two circuits will reinforce each other and it doesn't matter too much if the currents are equal or not (EMFs.info, 2013).

3.1. ELF magnetic fields from 110 kV power lines

In order to investigate the exposure levels from typical configurations of 110 kV overhead power lines, we have selected a DCL geometry dictated by suspension towers of Sn 110.252 type. According to the coordinate system in Fig. 1, the horizontal separation distances between conductors are 6.1 m, for both the upper and lower conductors, and 10 m, for the middle conductors, whereas the vertical separation distances are 4.6 m, between the lower and middle conductors, and 5.7 m, between the middle and upper conductors, respectively. With this phase arrangement, the associated ELF magnetic fields have been computed for two distinct ground clearances: 8 m and 15.2 m, respectively.

Table 1 summarizes computation results obtained at the height of 1 m above the ground, for different loading conditions, by using the PowerMAG software. For 8 m ground clearance (275 A loading, U phasing), the maximum magnetic flux density under line does not exceed 6.33 μT, which is approximately 16 times lower than the ICNIRP exposure limit.

At 18.5 m distance from the centerline, which represents the semi-width of the safety / protection zone for 110 kV simple- and double-circuit lines (NTE 003/04/00, 2004), the magnetic flux density decreases to 2.05 μT, accounting for less than 2.1 % from the ICNIRP exposure limit. In Table 1, the "maximum magnetic field under line" represents the largest field computed for the considered parameters, but it is not necessarily on the route centerline.

Table 1. Computed magnetic flux densities from the considered 110 kV double-circuit line

Line (kV)	*Load (A)*	*Clearance (m)*	*Phasing (U/T)*	*Magnetic field, B (μT), at distance from centerline*					
				maximum under line	*10 m*	*18.5 m*	*25 m*	*50 m*	*100 m*
2x110	100	8	U	2.3007	1.5190	0.7454	0.4683	0.1354	0.0352
			T	1.5930	0.6935	0.2420	0.1230	0.0206	0.0033
		15.2	U	0.9536	0.7625	0.5040	0.3603	0.1246	0.0344
			T	0.3659	0.2517	0.1338	0.0815	0.0178	0.0031
	175	8	U	4.0262	2.6583	1.3045	0.8195	0.2370	0.0617
			T	2.7879	0.8263	0.4236	0.2153	0.0362	0.0058
		15.2	U	1.6688	1.3344	0.8820	0.6305	0.2181	0.0605
			T	0.6403	0.4406	0.2342	0.1427	0.0311	0.0055
	275	8	U	6.3269	4.1774	2.0500	1.2879	0.3725	0.0969
			T	4.3810	1.9071	0.6657	0.3383	0.0569	0.0091
		15.2	U	2.6225	2.0969	1.3861	0.9908	0.3428	0.0948
			T	1.0062	0.6924	0.3680	0.2243	0.0489	0.0087

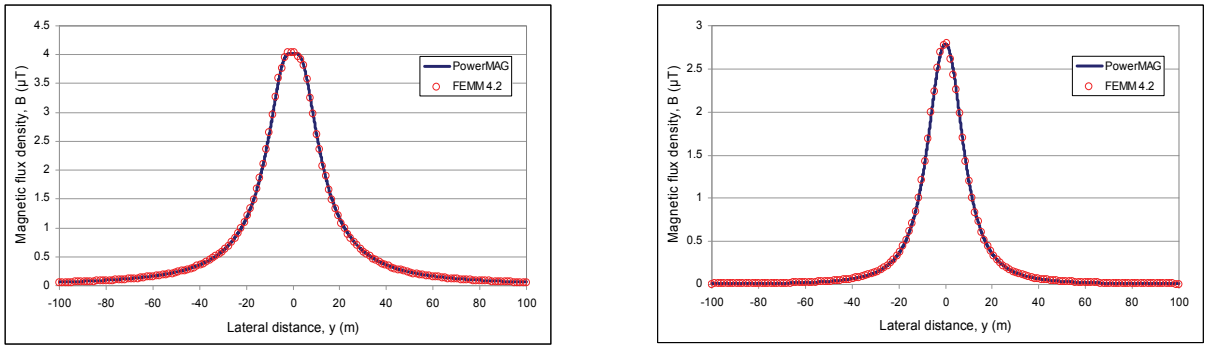

Fig. 3. Lateral profiles of the magnetic flux density from the considered 110 kV double-circuit line: (a) untransposed phasing; (b) transposed phasing

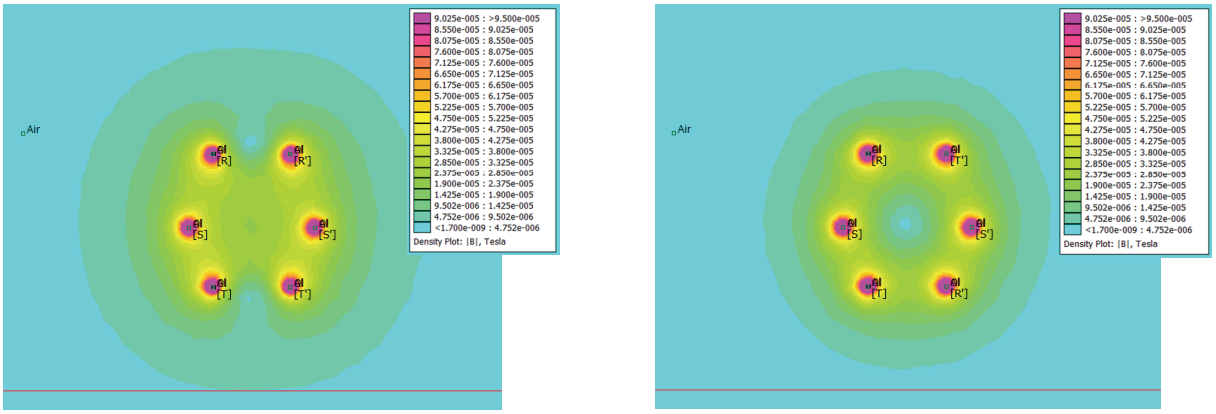

Fig. 4. Distributions of the magnetic flux density from the considered 110 kV double-circuit line, computed with FEMM 4.2: (a) untransposed phasing; (b) transposed phasing

Fig. 3 compares lateral profiles of the magnetic flux density from the considered 110 kV DCL (generated with the two methods, at the height of 1 m above the ground), revealing a very good result agreement. The FEMM model adopted here is the same as in Fig. 2, with the mention that the active conductors of the two circuits are assumed to be steel-reinforced aluminum conductors with standard sections of 185/32 mm^2.

Profiles are computed for both transposed and untransposed phasing, by considering 175 A loading and 8 m ground clearance. The distribution of the magnetic flux density around the line – obtained with FEMM 4.2 – is shown in Fig. 4. At 1 m below the lowest conductor, the magnetic field for untransposed phasing is approximately 30 μT, whereas the magnetic field for transposed phasing goes higher, to approximately 32 μT (very similar results have also

been obtained with PowerMAG). However, as can easily be seen from both Fig. 3 and Fig. 4, the ELF magnetic fields for transposed phasing fall more rapidly with distance, producing significantly lower exposure at large distances from the line.

Note that, in Fig. 4, the two distributions of magnetic flux density are given for the same region, namely 20 m lateral distance from the DCL centerline and 30 m height above the ground level (the bottom line).

3.2. ELF magnetic fields from 220 kV power lines

Similarly, to investigate the exposure levels from typical configurations of 220 kV overhead power lines, we have selected a DCL geometry dictated by suspension towers of Sn 220.202 type. In this case, the horizontal separation distances between conductors are 10 m, for both the upper and lower conductors, and 16 m, for the middle conductors, whereas, in vertical plane, all the phases are separated by 6.5 m. With this phase arrangement, the associated ELF magnetic fields have also been computed for two distinct ground clearances: 10 m and 19.2 m, respectively.

Computation results obtained with the PowerMAG software are presented in Table 2. For 10 m ground clearance (500 A loading, U phasing), the maximum magnetic flux density under line does not exceed 7.99 μT, which is approximately 12.5 times lower than the ICNIRP exposure limit. At 27.5 m distance from the centerline, which represents the semi-width of the safety / protection zone for 220 kV simple- and double-circuit lines (NTE 003/04/00, 2004), the magnetic flux density decreases to 2.37 μT, accounting for less than 2.4 % from the ICNIRP exposure limit. However, as with the 110 kV power lines, the typical exposure levels are below the aforementioned values, because the ground clearances are usually higher and the loads are usually lower.

Lateral profiles of the magnetic flux density from the considered 220 kV DCL (generated with FEMM 4.2 and PowerMAG) are comparatively presented in Fig. 5. These computations are also performed at the height of 1 m above the ground, for both transposed and untransposed phasing, by considering 250 A loading and 10 m ground clearance. Once again, a very good result agreement can be observed.

Table 2. Computed magnetic flux densities from the considered 220 kV double-circuit line

Line (kV)	*Load (A)*	*Clearance (m)*	*Phasing (U/T)*	*Magnetic field, B (μT), at distance from centerline*					
				maximum under line	*10 m*	*25 m*	*27.5 m*	*50 m*	*100 m*
2x220	100	10	U	1.5963	1.4080	0.5485	0.4735	0.1675	0.0442
			T	1.3961	0.9026	0.2203	0.1780	0.0388	0.0053
		19.2	U	0.7107	0.6329	0.3738	0.3378	0.1469	0.0426
			T	0.3613	0.2913	0.1283	0.1102	0.0320	0.0050
	250	10	U	3.9907	3.5201	1.3713	1.1839	0.4188	0.1105
			T	3.4902	2.2566	0.5508	0.4451	0.0971	0.0134
		19.2	U	1.7768	1.5823	0.9346	0.8445	0.3674	0.1066
			T	0.9034	0.7284	0.3207	0.2757	0.0802	0.0127
	500	10	U	7.9815	7.0402	2.7427	2.3679	0.8377	0.2211
			T	6.9805	4.5133	1.1016	0.8903	0.1942	0.0268
		19.2	U	3.5537	3.1647	1.8692	1.6890	0.7349	0.2133
			T	1.8068	1.4569	0.6414	0.5514	0.1604	0.0254

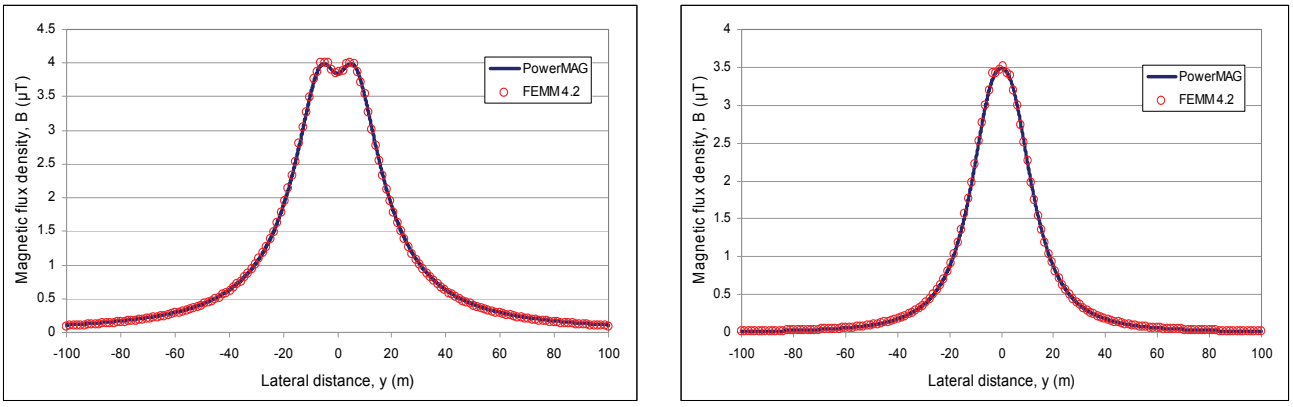

Fig. 5. Lateral profiles of the magnetic flux density from the considered 220 kV double-circuit line: (a) untransposed phasing; (b) transposed phasing

The distribution of the magnetic flux density around the line – obtained with FEMM 4.2 – is shown in Fig. 6. At 1 m below the lowest conductor, the magnetic field for untransposed phasing is approximately 45.5 μT, whereas the magnetic field for transposed phasing is approximately 47.3 μT (the values computed with PowerMAG are 44.2 μT and 46.9 μT, respectively). And this time, as can be seen from both Fig. 5 and Fig. 6, the ELF magnetic fields for transposed phasing fall more rapidly with distance. In Fig. 6, the two distributions of magnetic flux density are given for 30 m lateral distance from the DCL centerline and 35 m height above the ground level.

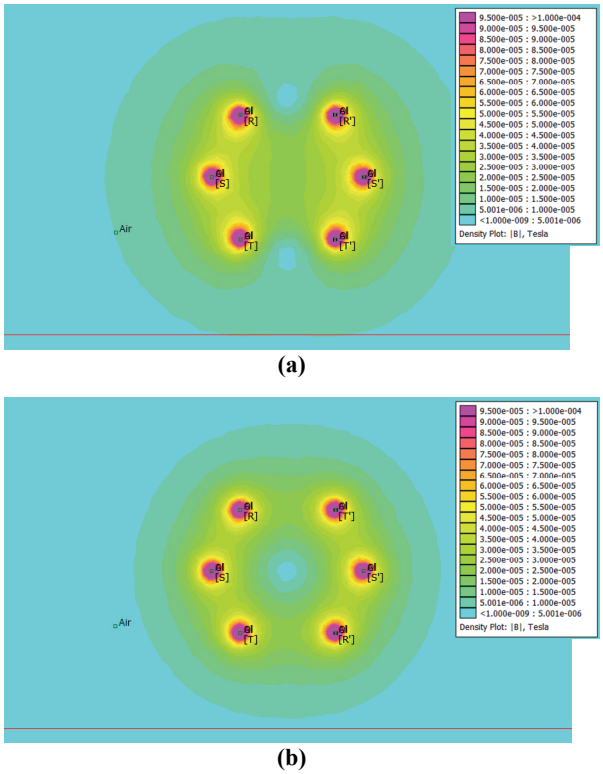

(a)

(b)

Fig. 6. Distributions of the magnetic flux density from the considered 220 kV double-circuit line, computed with FEMM 4.2: (a) untransposed phasing; (b) transposed phasing

4. Conclusion and future work

According to the computations carried out in this study, it can be concluded that the levels of general public exposure to ELF magnetic fields from common configurations of 110 kV and 220 kV overhead power lines of the national power grid are well bellow the limits recommended by ICNIRP.

The results obtained with analytical and numerical methods – for different exposure scenarios – are in very good agreement. Future work will be focused on extending this theoretical investigation to other configurations of overhead power lines, also including 400 kV transmission lines, as well as on comparing computation results with measurement data.

Likewise, special attention will be paid to the determination of the ELF electric fields associated with such lines, which are generally less investigated with respect to human exposure.

Acknowledgement

This paper was supported by the project PERFORM-ERA "Postdoctoral Performance for Integration in the European Research Area" (ID-57649), financed by the European Social Fund and the Romanian Government.

References

Ahlbom A., Day N., Feychting M., Roman E., Skinner J., Dockerty J., Linet M., McBride M., Michaelis J., Olsen J.H., Tynes T., Verkasalo P.K., (2000), A pooled analysis of magnetic fields and childhood leukaemia, *British Journal of Cancer*, **83**, 692-698.

Buzdugan M.I., Balan H., (2011), Some practical considerations in electromagnetic biocompatibility, *Environmental Engineering and Management Journal*, **10**, 519-525.

El-Fouly T.H.M., El-Saadany E.F., Salama M.M.A., Abdel-Galil T.K., Habiballah I.O., (2005), *Power Transmission Lines Generated Electric and Magnetic Fields Calculations*, Proc. COMSOL Multiphysics User's Conference, Boston, USA, 255-260.

EMFs.info website, (2013), Factors affecting the field from an overhead power line phasing, On line at: http://www.emfs.info/Sources+of+EMFs/Overhead+power+lines/Factors/Phasing.

Filippopoulos G., Tsanakas D.K., (2005), Analytical calculation of the magnetic field produced by electric power lines, *IEEE Transactions on Power Delivery*, **20**, 1474-1482.

Greenland S., Sheppard A.R., Kaune W.T., Poole C., Kelsh M.A., (2000), A pooled analysis of magnetic fields, wire codes, and childhood leukemia. Childhood Leukemia-EMF Study Group, *Epidemiology*, **11**, 624-634.

Hameyer K., Mertens R.P., Belmans R., (1995), *Numerical Methods to Evaluate the Electromagnetic Fields Below Overhead Transmission Lines and Their Measurement*, Proceedings of the 1995 First IEEE International Caracas Conference on Devices, Circuits and Systems (ICCDCS), 12-14 December, Caracas, Venezuela, 32-36, DOI 10.1109/ICCDCS.1995.499113.

IARC Working Group, (2002), *IARC Monographs on the Evaluation of Carcinogenic Risks to Humans series. Non-Ionizing Radiation, Part 1: Static and Extremely Low-Frequency (ELF) Electric and Magnetic Fields*, Vol. 80, IARC Press, Lyon, France, On line at: http://monographs.iarc.fr/ENG/Monographs/vol80/mono80.pdf.

ICNIRP, (1998), Guidelines for limiting exposure to time-varying electric, magnetic and electromagnetic fields (up to 300 GHz), *Health Physics*, **74**, 494-522.

ICNIRP, (2010), Guidelines for limiting exposure to time-varying electric and magnetic fields (1 Hz – 100 kHz), *Health Physics*, **99**, 818-836.

Kaune W.T., Zaffanella L.E., (1992), Analysis of magnetic fields produced far from electric power lines, *IEEE Transactions on Power Delivery*, **7**, 2082-2091.

Lunca E., Istrate M., Salceanu A., Tibuliac S., (2012), *Computation of the Magnetic Field Exposure from 110 kV Overhead Power Lines*, Proc. 7th Int. Conf. on

Electrical and Power Engineering, 25-27 October, Iasi, Romania, 628-631, DOI 10.1109/ICEPE.2012.6463803.

Milutinov M., Juhas A., Prša M., (2009), *Electromagnetic Field Underneath Overhead High Voltage Power Line*, Proc. 4th Int. Conf. on Engineering Technologies, Novi Sad, Serbia, 1-5.

Moro F., Turri R., (2008), Fast analytical computation of power-line magnetic fields by complex vector method, *IEEE Transactions on Power Delivery*, **23**, 1042-1048.

Neacşu O., Beniugă O., Sălceanu A., (2012), Assessment on electric charges pollution in the residential area and laboratory environment, *Environmental Engineering and Management Journal*, **11**, 635-640.

Nica I., David V., Dafinescu V., Salceanu A., Haba C.G., (2011), Characterization of electromagnetic radiation from a patient monitor, *Environmental Engineering and Management Journal*, **10**, 561-566.

NTE 003/04/00, (2004), Normative document regarding the construction of aerial electricity lines with voltages about 1000 V (in Romanian), approved by Order No. 32/17.11.2004 of ANRE CEO, On line at: http://www.scribd.com/doc/55867608/NTE-003-04-00-PE-104-15-noe-2004.

Olsen R.G., Backus S.L., Steams R.D., (1995), development and validation of software for predicting elf magnetic fields near power lines, *IEEE Transactions on Power Delivery*, **10**, 1525-1534.

Olsen R.G., Deno D., Baishiki R.S., Abbot J.R., Conti R., Frazier M., Jaffa K., Niles G.B., Stewart J.R., Wong R., Zavadil R.M., (1988), Magnetic fields from electric power lines: theory and comparison to measurements, *IEEE Transactions on Power Delivery*, **3**, 2127-2136.

Tupsie S., Isaramongkolrak A., Pao-la-or P., (2010), Analysis of electromagnetic field effects using FEM for transmission lines transposition, *International Journal of Electrical and Computer Engineering*, **5**, 227-231.

Wertheimer N., Leeper E., (1979), Electrical wiring configurations and childhood cancer, *American Journal of Epidemiology*, **109**, 273-284.

Finite Element Analysis of Electromagnetic Fields Emitted by Overhead High-Voltage Power Lines

Eduard Lunca, Bogdan Constantin Neagu, and Silviu Vornicu

Abstract The overhead high-voltage power lines (OHVPLs) are considered significant sources of extremely low frequency (ELF) electric and magnetic fields (EMFs), whose potential health effects became during the past decades a matter of scientific debate and public concern all over the world. In this chapter, a simple and yet effective finite element (FE) approach is proposed to compute and analyze—from the perspective of public exposure—both electric and magnetic fields emitted by typical configurations of OHVPLs belonging to the Romanian power grid. First, a 2D ANSYS Maxwell model is developed for the specific instance of a 110 kV double-circuit OHVPL and validated against two software tools based on quasi-static analytical methods, PowerELT and PowerMAG. Next, it will be used to investigate exposure to ELF-EMFs emitted by a selection of OHVPLs with nominal voltages of 110 kV, 220 kV and 400 kV, taking into consideration influencing factors such as loading, phasing and ground clearance. Compliance with the exposure guidelines specified by the International Commission on Non-Ionizing Radiation Protection (ICNIRP) for general public is assessed for each particular case. As a result, all calculated magnetic fields are below the ICNIRP limit of 100 μT, while the electric fields exceed the ICNIRP limit of 5000 V/m only in limited areas beneath the 400 kV OHVPLs. The calculated field levels are in line with those reported in the scientific literature for similar OHVPLs.

E. Lunca (✉) · S. Vornicu
Department of Electrical Measurements and Materials, Gheorghe Asachi Technical University of Iasi, Iasi, Romania
e-mail: elunca@tuiasi.ro

S. Vornicu
e-mail: silviusieca@gmail.com

B. C. Neagu
Power System Department, Electrical Engineering Faculty, Gheorghe Asachi Technical University of Iasi, Iasi, Romania
e-mail: bogdan.neagu@tuiasi.ro

N. Mahdavi Tabatabaei and N. Bizon (eds.), *Numerical Methods for Energy Applications*, Power Systems,
https://doi.org/10.1007/978-3-030-62191-9_29

Keywords Overhead high-voltage power line · Electric field · Magnetic field · Public exposure · 2D ANSYS maxwell model

Abbreviations

A. Acronyms

2D	Two-Dimensional
ACSR	Aluminum Conductor Steel-Reinforced
ELF	Extremely Low Frequency
EMF	Electric and Magnetic Fields
EU	European Union
FE	Finite Element
FEM	Finite Element Method
IARC	International Agency for Research on Cancer
ICNIRP	International Commission on Non-Ionizing Radiation Protection
IEEE	Institute of Electrical and Electronics Engineers
OHVPL	Overhead High-Voltage Power Line
RMS	Root Mean Square
SW	Shield Wire
T	Transposed
U	Untransposed
WHO	World Health Organization

B. Symbols/Parameters

B	Magnetic flux density
E	Electric field strength
i	Conductor number
I_i	Phase current of conductor i
U_i	Phase voltage of conductor i
d_i	Lateral distance from centerline to conductor i
h_i	Height of conductor i
h_g	Line-to-ground clearance
h	Calculation height above ground
R_{eq}	Bundle conductor equivalent radius

1 General

The electricity has many benefits in our daily life. But generating, transmitting, distributing and using electricity can expose people to ELF-EMFs, which interact with the human body by mainly inducing electric currents in it. During the past

decades, a lot of research has been devoted to investigation of possible health effects of exposure to ELF-EMFs, including childhood and adult cancers, reproductive dysfunctions, cardiovascular and developmental disorders, immunological modifications, neurological effects, etc. Particularly, a (poor) statistical link between childhood leukemia and prolonged exposure to residential ELF magnetic fields higher than 0.3–0.4 μT has been reported by a number of epidemiological studies [1, 2]. In 2002, based on these findings, the International Agency for Research on Cancer (IARC)—an intergovernmental agency activating within the World Health Organization (WHO)—has concluded that the ELF magnetic fields are "possibly carcinogenic to humans" (Group 2B carcinogens, designating agents for which the evidence in humans is limited and the evidence in animals is "less than sufficient"). As for ELF electric fields, IARC has concluded that they are "unclassifiable as to carcinogenicity in humans" (Group 3 carcinogens) [3].

Aiming at preventing the established health effects associated with short-term exposure to high intensity ELF-EMFs, principally induced currents, ICNIRP and IEEE (the Institute of Electrical and Electronics Engineers) have formulated exposure guidelines in 1998 [4] and 2002 [5], respectively. According to the scientific information currently available, long-term exposure to ELF field levels not exceeding the limits prescribed by these guidelines is considered safe for the purpose of protecting human health. There is no established evidence that exposure to ELF-EMFs emitted by power lines, substations, transformers or other electrical equipment, regardless of the proximity, can cause any known health effects. But there is a continuous debate as to what might be adequate precautionary approaches at these lower field levels. Furthermore, the general public often expresses concern about ELF-EMFs, especially in relation with setting up new overhead high-voltage power lines or living in their vicinity [6–9].

The OHVPLs are considered significant sources of both electric and magnetic fields. Both fields are strongest directly under the OHVPL and sharply reduce with distance from it. Of course, in addition to distance, there are many other factors influencing the ELF-EMFs originating from OHVPLs, including voltage, current, phasing, ground clearance, observation height above the ground, balance within circuit, balance between circuits, conductor bundle, existence of parallel lines, ground resistivity (conductivity), etc. Moreover, the electric fields are greatly attenuated by buildings, walls, fences, trees and other obstacles in the neighborhood, but the magnetic fields pass through most materials and cannot be attenuated as easily as the electric fields [10–12].

To determine ELF electric and magnetic field levels emitted by OHVPLs and to assess compliance with relevant exposure limits, both measurements and computations can be performed [13–19]. Computations are often preferable to measurements because they can be conducted for any desired exposure scenario rather than being confined to the particular conditions at the time of taking measurements. Analytical and numerical methods can be used for computations, usually employing two-dimensional (2D) models because of their simplicity [20–33]. Very often, the numerical calculations (simulations) exploit the finite element method (FEM), which is

recognized for its ability to generate accurate 2D electric and magnetic field distributions in the transverse section of the OHVPLs and of other power–frequency systems [19, 29–33].

In this chapter, a simple and yet effective FEM approach is proposed to compute and analyze—from the perspective of public exposure—ELF electric and magnetic fields produced by typical configurations of OHVPLs belonging to the Romanian power grid. Computations are performed with ANSYS Maxwell 2D electromagnetic simulation software, mainly in the form of RMS electric field strength and RMS magnetic flux density lateral profiles, at the standard height $h = 1$ m above the ground level. It is worthwhile to remark that Romania, as a member of the European Union (EU), has implemented exposure limits derived from the *Council Recommendation of 12 July 1999 on the limitation of exposure of the general public to electromagnetic fields (0 Hz–300 GHz)* [34], which is based on the guidelines issued by ICNIRP in 1998. For power–frequency electric and magnetic fields, these limits are 5000 V/m and 100 μT, respectively.

From this point, the chapter is organized as follows. First, a 2D ANSYS Maxwell model for computing ELF electric and magnetic fields around OHVPLs will be developed and validated against simulation software based on analytical methods. Next, it will be used to investigate exposure to ELF-EMFs generated by a selection of OHVPLs with nominal voltages of 110, 220 and 400 kV. As already mentioned, special attention will be given to the field distribution at 1 m height above the ground, taking into consideration influencing factors such as loading, phasing and ground clearance. Compliance with the ICNIRP exposure limits for general public will be assessed for each particular case.

2 2D ANSYS Maxwell Model for Computing ELF Electric and Magnetic Fields Around OHVPLs

ANSYS Maxwell 2D is a high-performance low frequency electromagnetic field simulation software that uses the finite element method for solving electric, magnetostatic, eddy current and transient problems. Therefore, it may serve as an appropriate tool for computing exposure to ELF-EMFs originating from OHVPLs, but such investigations are rather rare and mostly focused only on the magnetic field exposure [17, 35, 36]. As an extension of a recent study by the authors [11], this section presents the development and validation of a 2D Maxwell model for computing both electric and magnetic fields emitted by various OHVPLs. The model is implemented for a common configuration of 110 kV double-circuit line used for primary power distribution, but it can easily be applied to any other OHVPL. The model validation is achieved against previously developed software based on quasi-static analytical methods.

2.1 Model Development

The 110 kV double-circuit OHVPL selected for model implementation—often found in the proximity of urban settings—has geometry dictated by suspension towers of Sn 110.252 type, as illustrated in Fig. 1. The phases of the two circuits are realized with Aluminum Conductor Steel-Reinforced (ACSR) cables of Sect. 240/40 mm^2 (21.7 mm exterior diameter), while the shield wire (SW) is represented by a 160/95 mm^2 ACSR conductor (20.75 mm exterior diameter). The OHVPL is considered to operate at a load of 500 A (close to the maximum rated current), with the phases of the two circuits perfectly balanced. In addition, because the field level largely depends on the relative phasing between the two circuits, we assumed both untransposed (ABC/A'B'C') and directly transposed (ABC/C'B'A') phase arrangements, which

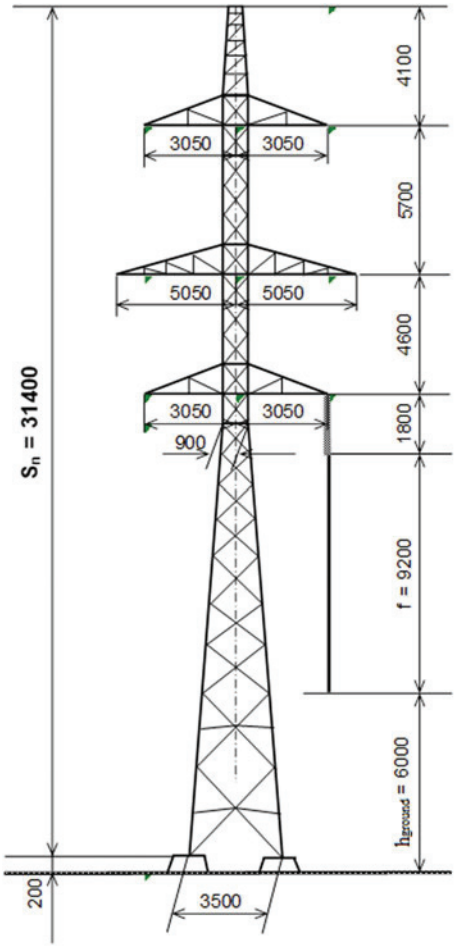

Fig. 1 Suspension tower of Sn 110.252 type (dimensions are given in mm)

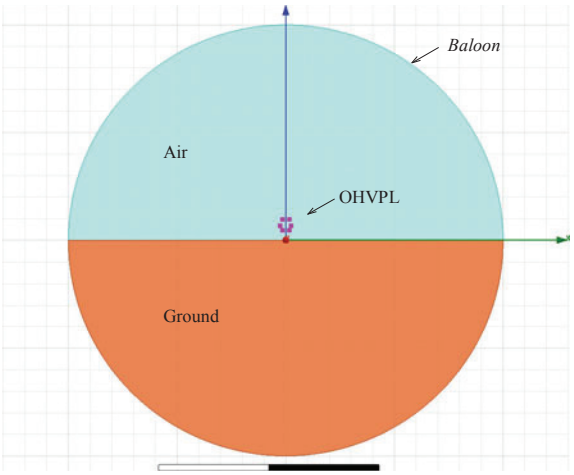

Fig. 2 Global FEM geometric model of the 110 kV double-circuit OHVPL

clearly determine the maximum and minimum exposure to the sides of the line [37, 38], where people are most likely to live or spend time.

a. *FEM geometric model*

The global FEM geometric model is presented in Fig. 2, where the considered 110 kV double-circuit OHVPL is placed above a ground with the electrical conductivity of 0.01 S/m, the relative electric permittivity of 10 and the relative magnetic permeability of 1. The ground clearance, namely 9 m, corresponds to an "average height" of the OHVPL above the ground, calculated as $h_{avg} = h_{max}$—(2/3)·f [39], where $h_{max} = 15.2$ m represents the maximum height of the conductors (at tower) and $f = 9.2$ m is the conductors sag. The active conductors are modeled as presented in Fig. 3, as simple aluminum cylinders with the electrical conductivity of $3.8 \cdot 10^7$ S/m, the relative electric permittivity of 1 and the relative magnetic permeability of 1, while the influence of the SW on the electric and magnetic field distribution is ignored (the SW is not included in simulation). The applied boundary conditions are of Balloon type, which models the region outside the defined space as extending to infinity. The radius of the bounded region is taken $R = 200$ m, sufficiently large to determine the behavior of the two fields well outside the power line corridor, even for OHVPLs with higher nominal voltages. All simulations conducted in this study assume a total number of mesh elements of 1,223,286, but it can be lowered for more rapid and yet satisfactory analyzes.

b. *Magnetic field calculation*

The magnetic field distribution around the OHVPL is obtained using the *eddy current solver*, which allows calculating magnetic fields that oscillate with a frequency (in this case, 50 Hz). However, because the magnetic field distributions generated with this solver are reported in terms of instantaneous magnetic flux density values over a 20 ms period, further post-processing is necessary to generate RMS

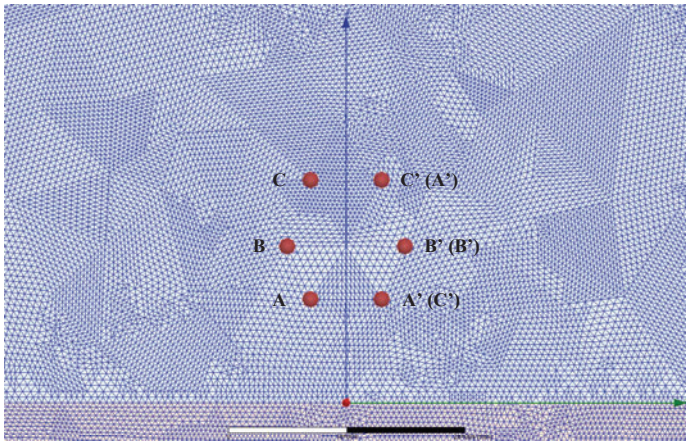

Fig. 3 Discretized OHVPL region

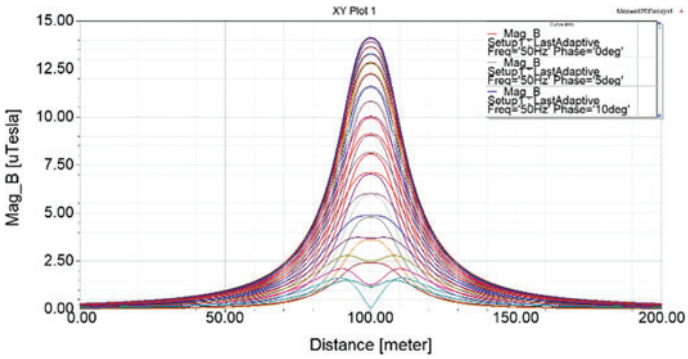

Fig. 4 Instantaneous magnetic flux density profiles at $h = 1$ m, for U phasing

magnetic flux density (lateral) profiles at the height $h = 1$ m, as often used for assessing exposure to ELF-EMFs from overhead power lines. Consequently, multiple instantaneous magnetic flux density profiles have been imported into Microsoft Excel, where they have been processed in a point-by-point fashion, according to the formula [11]:

$$B_{RMS}(i) = \sqrt{\frac{1}{N}\sum_{n=1}^{N} B_n^2(i)}, \tag{1}$$

where $B_1(i), \ldots, B_N(i)$ represent the instantaneous values of the magnetic flux density corresponding to the point i of the profile and $N = 73$ is the total number of values.

Figure 4 presents instantaneous magnetic flux density profiles obtained for untransposed (U) phasing, while Fig. 5 shows similar profiles obtained for transposed (T) phasing. The correspondent RMS magnetic flux density profiles—computed with Eq. (1)—are comparatively presented in Fig. 6. Starting at a certain distance from the centerline, any other phase arrangement will generate an RMS magnetic flux density profile between these two limit plots.

Figures 7 and 8 illustrate the magnetic field distribution around the OHVPL at the time instants corresponding to the maximum field profiles in Figs. 4 and 5, respectively. As evident, an extra degree of cancellation between the magnetic fields generated by the two circuits can be observed for transposed phasing. The distance from the centerline is 30 m in both distributions.

c. *Electric field calculation*

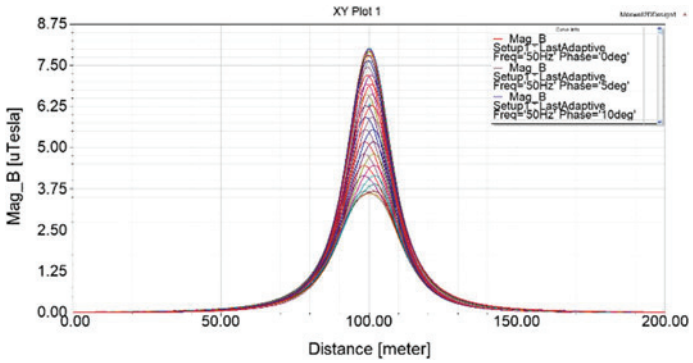

Fig. 5 Instantaneous magnetic flux density profiles at $h = 1$ m, for T phasing

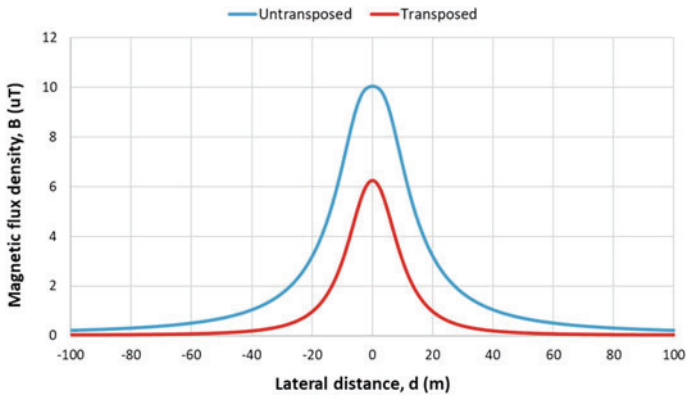

Fig. 6 Comparison between RMS magnetic flux density profiles obtained for untransposed and transposed phasing

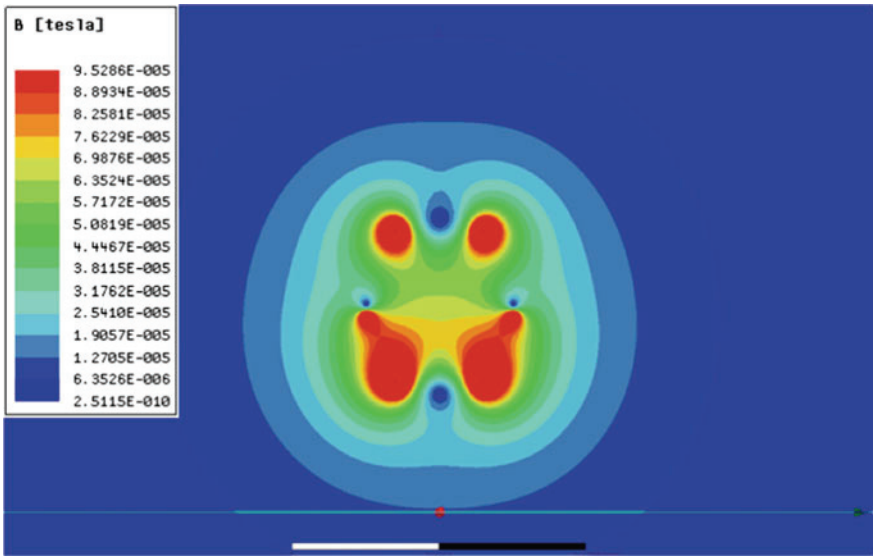

Fig. 7 The magnetic field distribution around the 110 kV double-circuit OHVPL for U phasing ($t = 10.83$ ms)

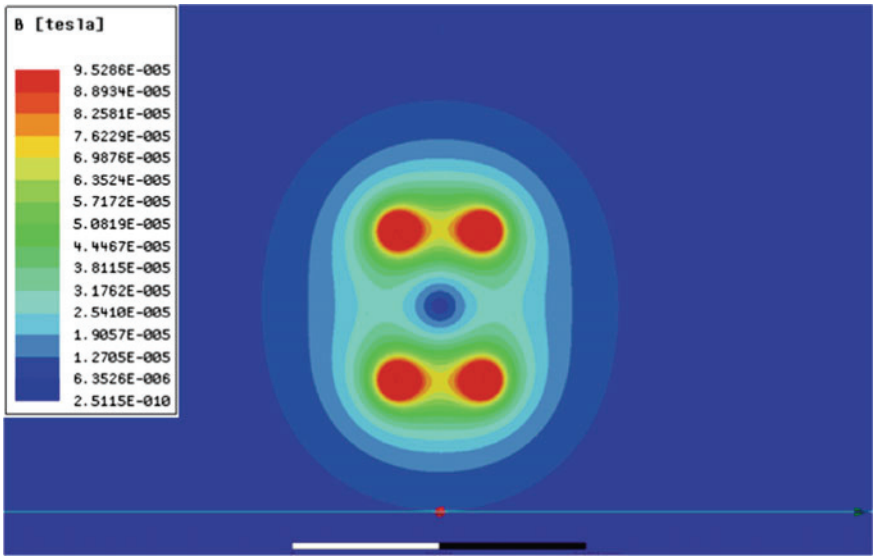

Fig. 8 The magnetic field distribution around the 110 kV double-circuit OHVPL for T phasing ($t = 11.66$ ms)

The electric field distribution around the OHVPL is determined using the *AC conduction solver*, which allows calculating sinusoidally-varying electric fields (here, varying at 50 Hz). And this time, to generate RMS electric field strength lateral profiles at the height $h = 1$ m, multiple profiles of instantaneous electric field strength have been imported into Microsoft Excel, where they have been processed in the same way, by applying the formula [11]:

$$E_{RMS}(i) = \sqrt{\frac{1}{N}\sum_{n=1}^{N} E_n^2(i)} \tag{2}$$

where $E_1(i), \ldots, E_N(i)$ represent the instantaneous values of the electric field strength corresponding to the point i of the profile and $N = 73$ is the total number of values.

As in the case of magnetic field, Fig. 9 gives instantaneous electric field strength profiles obtained for U phasing, while Fig. 10 shows profiles obtained for T phasing. The two associated RMS electric field strength profiles—computed with Eq. (2)—are compared in Fig. 11.

Figures 12 and 13 illustrate the momentary distribution of the electric field around the OHVPL corresponding to the maximum field profiles in Figs. 9 and 10, respectively. Once again, an extra degree of cancellation between the electric fields generated by the two circuits can be observed for transposed phasing. As in the case of magnetic field, the distance from the centerline is 30 m in both distributions.

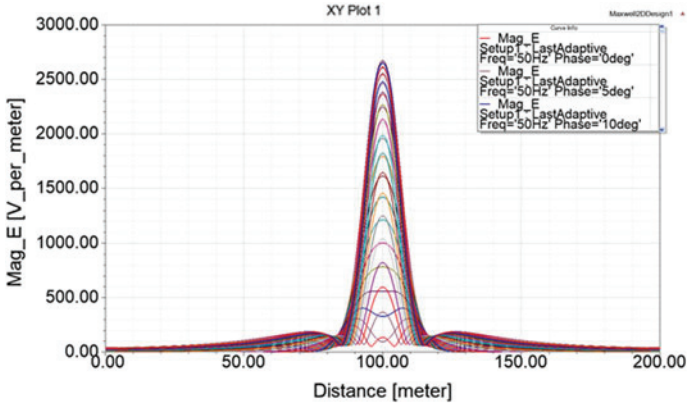

Fig. 9 Instantaneous electric field strength profiles at $h = 1$ m, for U phasing

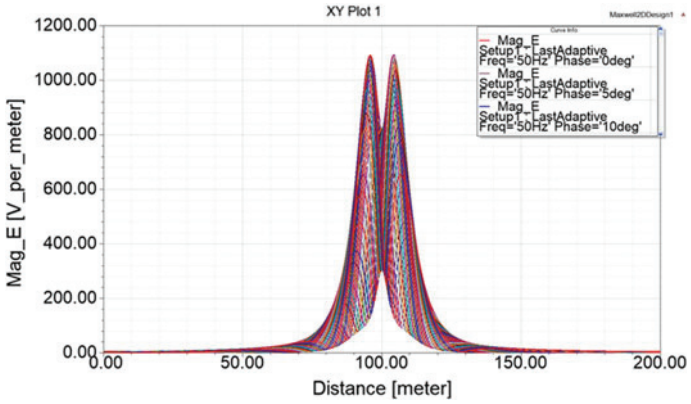

Fig. 10 Instantane-ous electric field strength profiles at $h = 1$ m, for T phasing

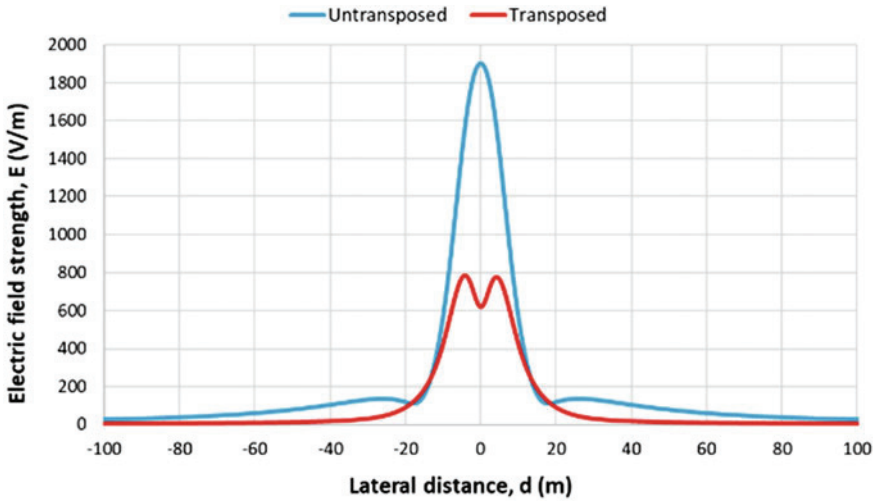

Fig. 11 Comparison between RMS electric field strength profiles obtained for untransposed and transposed phasing

2.2 Model Validation

The model validation has mainly been performed with the help of two interactive software tools based on analytical methods, *PowerELT* and *PowerMAG* [28], which are capable to produce accurate electric and magnetic field (lateral) profiles at any user-defined height above the ground level, together with 2D electric and magnetic field distributions in the transverse section of the OHVPL, in any rectangular plotting area also defined by user. Assuming the same power line geometry, and voltage and current information (amplitude and phase, respectively), Fig. 14 compares RMS

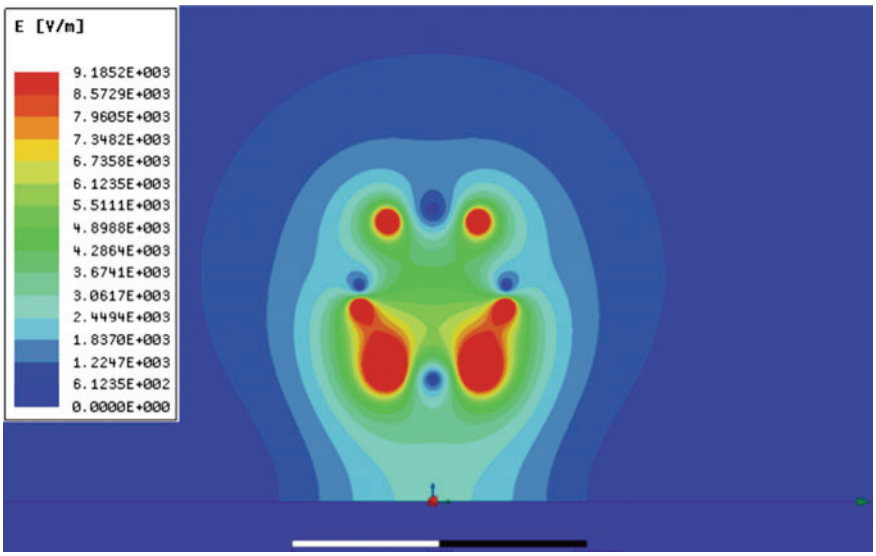

Fig. 12 The electric field strength distribu-tion around the 110 kV OHVPL for U phasing (t = 10.55 ms)

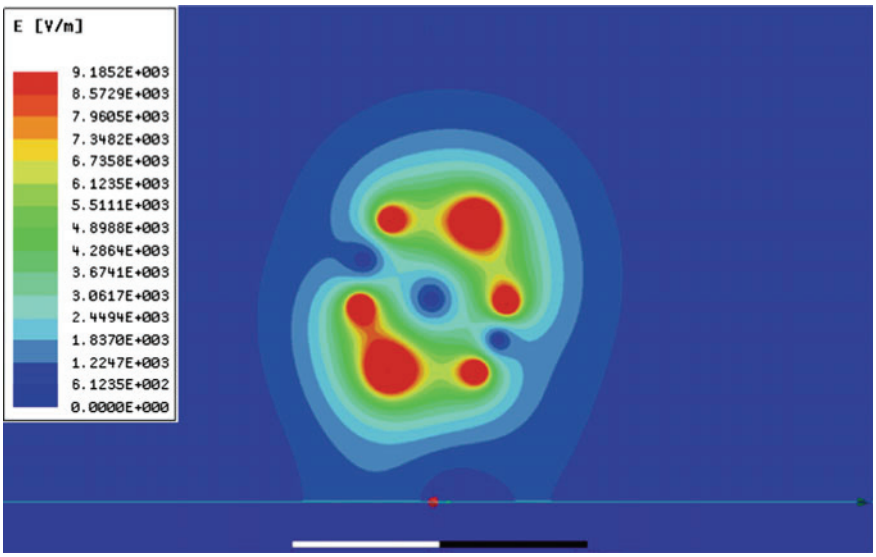

Fig. 13 The electric field strength distribu-tion around the 110 kV OHVPL for T phasing (t = 20 ms)

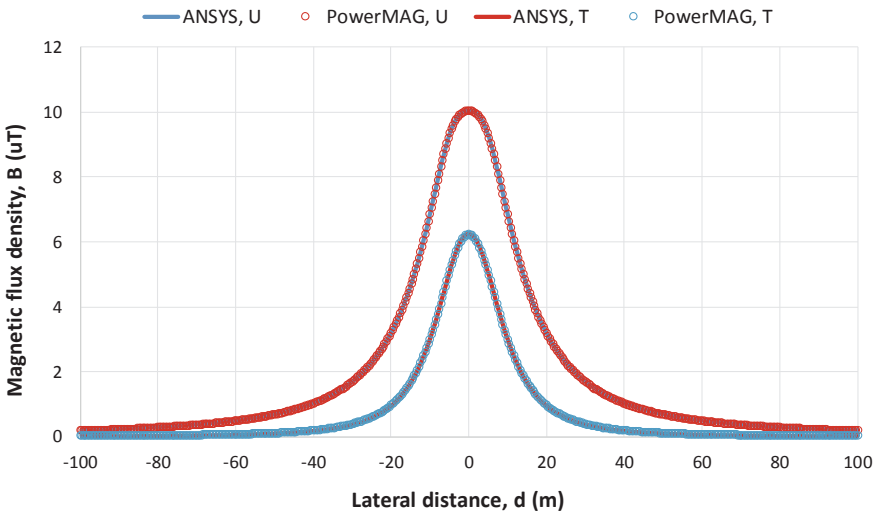

Fig. 14 Comparison between RMS magnetic flux density profiles obtained by numerical simulation and analytical computation

magnetic flux density profiles computed with the developed 2D ANSYS Maxwell model and PowerMAG software. Similarly, Fig. 15 compares RMS electric field strength profiles computed with the developed 2D ANSYS Maxwell model and

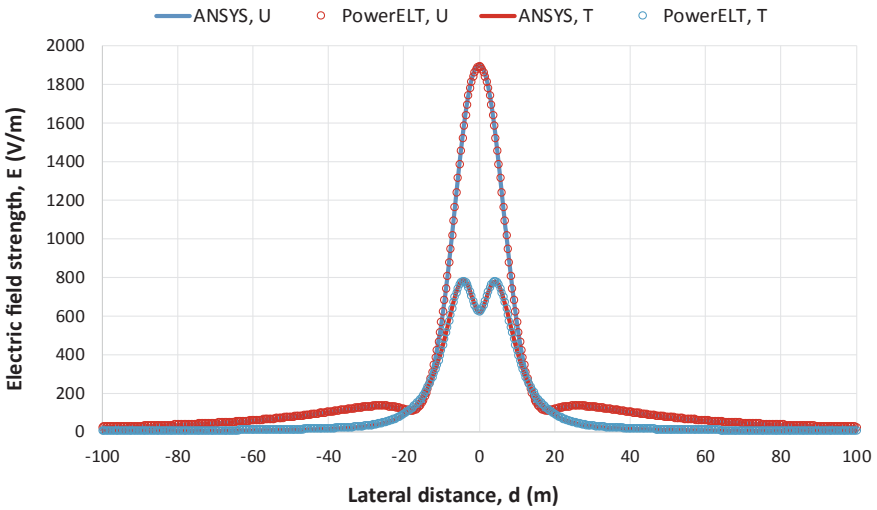

Fig. 15 Comparison between RMS electric field strength profiles obtained by numerical simulation and analytical computation

PowerELT software. As obvious, there is an excellent agreement between numerical and analytical results, regardless the phasing (U or T).

Similar comparisons have also been made for OHVPLs with higher nominal voltages (i.e., larger physical dimensions), each time obtaining perfect matching between simulated profiles. Exposure to ELF-EMFs from some of these lines, under various conditions, will be discussed in the subsequent section.

3 Finite Element Analysis of ELF-EMFs from Typical OHVPLs Used in the Romanian Power Grid

In Romania, OHVPLs are used for both power transmission and power distribution. Power transmission is achieved through a total length of 8759.4 km of OHVPLs, of which [40]: 3.1 km—750 kV, 4915.2 km—400 kV, 3875.6 km—220 kV and 40.4 km—110 kV, where 482.6 km serves as interconnection lines. In addition, power distribution operators make use of more than 20,000 km of OHVPLs operating at 110 kV. Thus, for assessing exposure to ELF-EMFs emitted by these OHVPLs, we have selected two double-circuit lines with nominal voltages of 110 kV and 220 kV, respectively, and a single-circuit line with nominal voltage of 400 kV, which can be considered typical. Finite element analysis of ELF-EMFs from these lines assumes the same conditions as in the described model, except that computations will be performed for three different ground clearances (minimum, average and maximum), as well as for maximum allowable current. However, because of the direct proportionality between current and magnetic flux density, the computed fields can easily be scaled down for more common loads.

3.1 ELF-EMFs from the 110 kV Double-Circuit OHVPL

In essence, the 110 kV double-circuit OHVPL subjected to investigations is the same used for model development, which has geometry dictated by suspension towers of Sn 110.252 type. As already mentioned, the two circuits are realized with standard 240/40 mm^2 ACSR conductors (21.7 mm exterior diameter), which have a maximum allowable current of 575 A (RMS). All other input data for this line are presented in Table 1, where d_i is the lateral distance from the OHVPL centerline to the conductor i, hi represents the height of the conductor i and h_g denotes the ground clearance of the line: 6 m, 9 m and 15.2 m, respectively.

a. *Magnetic field distribution*

Figure 16 presents RMS magnetic flux density profiles at the height $h = 1$ m, for untransposed phasing. The maximum magnetic field beneath the line (not necessarily at the centerline) varies from 5.48 μT for $h_g = 15.2$ m (at tower) to 18.5 μT for $h_g = 6$ m (at mid-span), which is generally below 18.5% of the ICNIRP limit for

Table 1 Input data for the 110 kV double-circuit OHVPL using towers of Sn 110.252 type (untransposed phasing)

Phase conductor	i	d_i [m]	hi [m]	$\underline{U_i}$ [kV]	$\underline{I_i}$ [A]
A	1	−3.05	h_g	$63.51 \angle 0°$	$575 \angle 0°$
B	2	−5.05	$h_g + 4.6$	$63.51 \angle -120°$	$575 \angle -120°$
C	3	−3.05	$h_g + 10.3$	$63.51 \angle 120°$	$575 \angle 120°$
A'	4	3.05	h_g	$63.51 \angle 0°$	$575 \angle 0°$
B'	5	5.05	$h_g + 4.6$	$63.51 \angle -120°$	$575 \angle -120°$
C'	6	3.05	$h_g + 10.3$	$63.51 \angle 120°$	$575 \angle 120°$

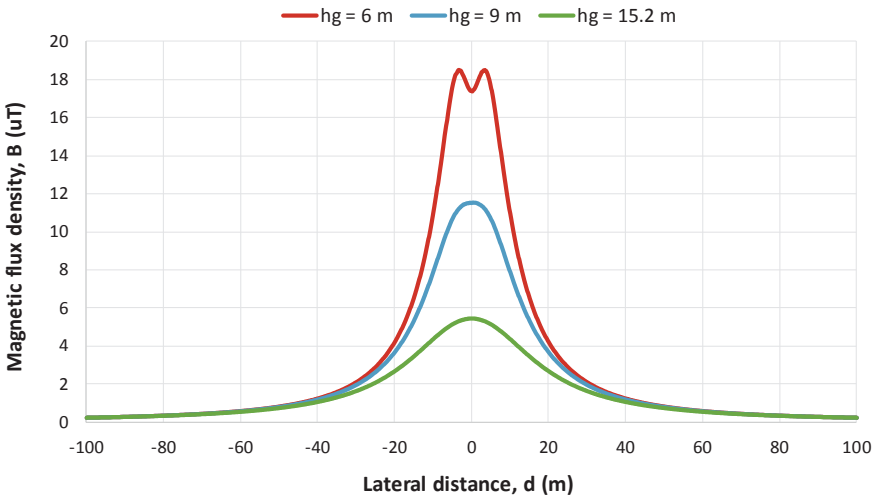

Fig. 16 RMS magne-tic flux density profiles for the 110 kV OHVPL, for untrasnsposed phasing and various ground clearances

general public, 100 μT. For transposed phasing (Fig. 17), the maximum magnetic field beneath the line varies from 2.12 μT for $h_g = 15.2$ m to 16.1 μT for $h_g = 6$ m, hence not exceeding 16.1% of the ICNIRP exposure limit. As it can easily be observed, starting with some distance from the centerline, the transposed phasing produces much lower magnetic field levels.

Considering the average clearance $h_g = 9$ m and a (more) typical loading of 325 A, Table 2 gives magnetic field levels at various distances from the centerline. Beneath the line, the magnetic flux density does not exceed 6.51 μT for U phasing and 4.03 μT for T phasing, while at the edge of the OHVPL corridor—18.5 m from the centerline, according to national regulations [41]—it decreases to 2.32 μT and 0.73 μT, respectively. The critical value of 0.4 μT—often used in epidemiological studies—is reached at a lateral distance of about 53.9 m and 24.5 m, respectively.

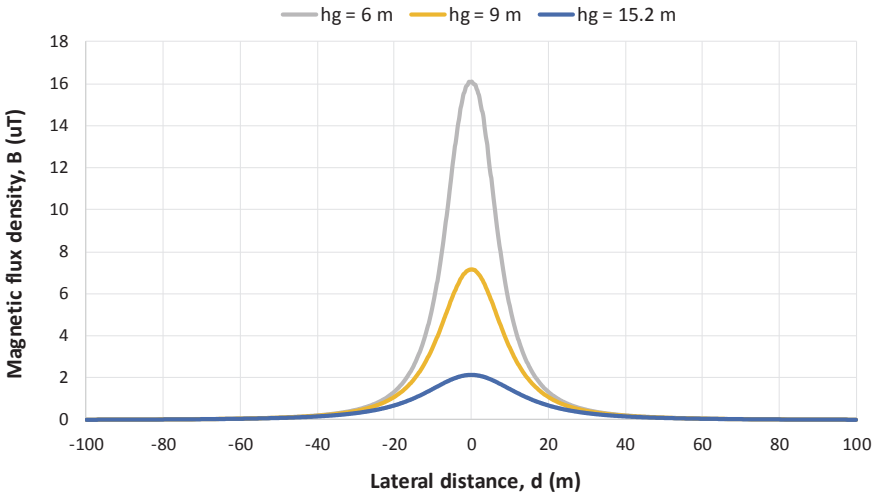

Fig. 17 RMS magne-tic flux density profiles for the 110 kV OHVPL, for transposed phasing and various ground clearances

Table 2 Typical magnetic field levels from the 110 kV OHVPL ($h_g = 9$ m, $I = 325$ A)

Phasing	B [μT], at various lateral distances				
	Maximum beneath line	*18.5 m*	*25 m*	*50 m*	*100 m*
U	6.51	2.32	1.49	0.46	0.14
T	4.03	0.73	0.38	0.067	0.011

b. *Electric field distribution*

The RMS electric field strength distribution at the height $h = 1$ m—for untransposed phasing—is illustrated in Fig. 18. The maximum electric field beneath the line (at the centerline) varies from 882.8 V/m at tower to 3017.2 V/m at mid-span, which is generally below 60.34% of the ICNIRP exposure limit for general public, 5000 V/m. For transposed phasing (Fig. 19), the maximum electric field levels beneath the line range from 243.2 V/m at tower to 1790.2 V/m at mid-span, hence not exceeding 35.8% of the exposure limit.

For the average clearance $h_g = 9$ m (Table 3), the electric field strength beneath the line reaches 1901.8 V/m for U phasing and 784.4 V/m for T phasing, while the electric field strength at the corridor edge reaches 110.3 V/m and 109.5 V/m, respectively. At the distance of 50 m from the centerline route, the electric field levels fall to only 77 and 11.3 V/m, respectively, similar to the lowest levels measured at 30 cm distance from household appliances.

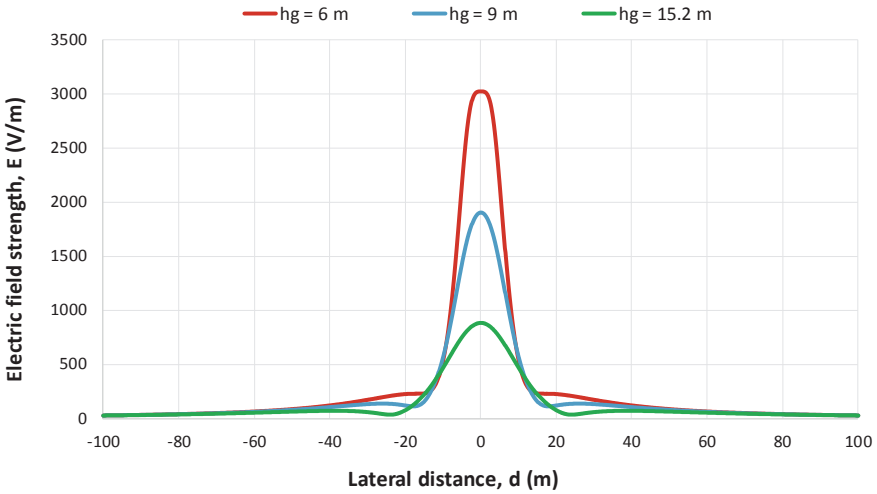

Fig. 18 RMS electric field strength profiles for the 110 kV OHVPL, for untransposed phasing and various ground clearances

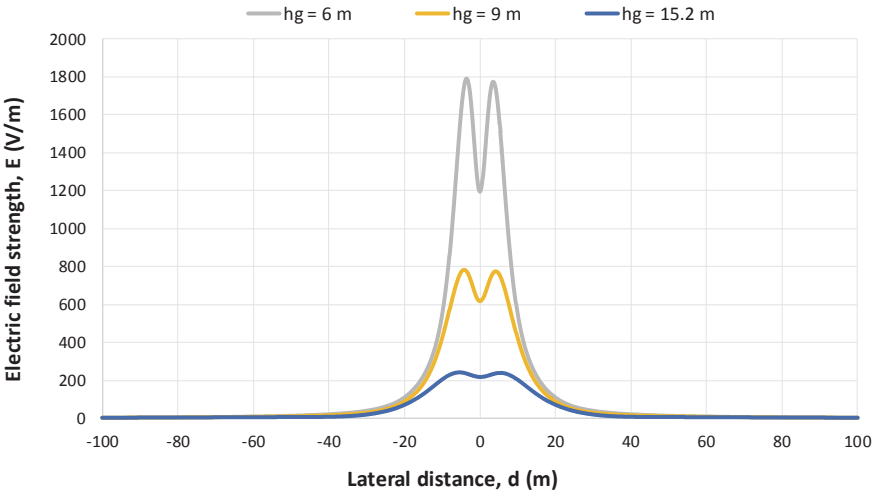

Fig. 19 RMS electric field strength profiles for the 110 kV OHVPL, for transposed phasing and various ground clearances

Table 3 Typical electric field levels from the 110 kV OHVPL ($h_g = 9$ m)

Phasing	E [V/m], at various lateral distances				
	Maximum beneath line	*18.5 m*	*25 m*	*50 m*	*100 m*
U	1901.8	110.3	134.4	77	25
T	784.4	109.5	47.9	11.3	3.3

3.2 ELF-EMFs from the 220 kV Double-Circuit OHVPL

The 220 kV double-circuit OHVPL selected for FE analysis has geometry dictated by suspension towers of Sn 220.202 type. The line is equipped with standard 450/75 mm^2 ACSR conductors (29.25 mm exterior diameter), for which the maximum allowable current is 975 A. Table 4 presents the geometrical data, as well as the voltage and current information used for computation, where the ground clearance h_g is taken 7 m, 11 m and 19 m, respectively. Because the geometry of this line is quite similar to the geometry of the 110 kV line, we expect similar electric and magnetic field distributions.

a. *Magnetic field distribution*

For untransposed phasing (Fig. 20), the maximum RMS magnetic flux density beneath the 220 kV OHVPL ranges from 7 μT at tower to 23.9 μT at mid-span, generally accounting for less than 24% of the ICNIRP exposure limit for general public. For transposed phasing (Fig. 21), the maximum RMS magnetic flux density along the half-span varies between 3.62 and 24.33 μT, hence not exceeding 24.4% of the ICNIRP exposure limit. And this time, much lower field levels can be observed at larger distances from the line for T phasing.

Table 5 gives magnetic field levels at various distances from the OHVPL centerline for the average clearance $h_g = 11$ m and a (more usual) loading of 200 A. Beneath the line, the magnetic flux density does not exceed 2.87 μT for U phasing and 2.35 μT for T phasing, while at the edge of the OHVPL corridor—27.5 m from the centerline [41]—it decreases to 0.93 μT and 0.42 μT, respectively. The critical value of 0.4 μT is reached at a lateral distance of about 45 m and 25.4 m, respectively. As we can see, because of the low load conditions, the typical exposure levels from this line are lower than those associated with the 110 kV OHVPL.

b. *Electric field distribution*

The electric field strength distribution for untransposed phasing is illustrated in Fig. 22. Beneath the 220 kV double-circuit OHVPL, the maximum field strength at the standard height $h = 1$ m ranges from 1452.8 V/m for $h_g = 19$ m to 4673.7 V/m for $h_g = 7$ m, which is very close to the ICNIRP limit for general public (93.5% of

Table 4 Input data for the 220 kV double-circuit OHVPL using towers of Sn 220.202 type (untransposed phasing)

Phase conductor	i	d_i [m]	hi [m]	$\underline{U}_i$ [kV]	$\underline{I}_i$ [A]
A	1	−5.00	h_g	$127 \angle 0°$	$975 \angle 0°$
B	2	−8.00	$h_g + 6.5$	$127 \angle -120°$	$975 \angle -120°$
C	3	−5.00	$h_g + 13$	$127 \angle 120°$	$975 \angle 120°$
A’	4	5.00	h_g	$127 \angle 0°$	$975 \angle 0°$
B’	5	8.00	$h_g + 6.5$	$127 \angle -120°$	$975 \angle -120°$
C’	6	5.00	$h_g + 13$	$127 \angle 120°$	$975 \angle 120°$

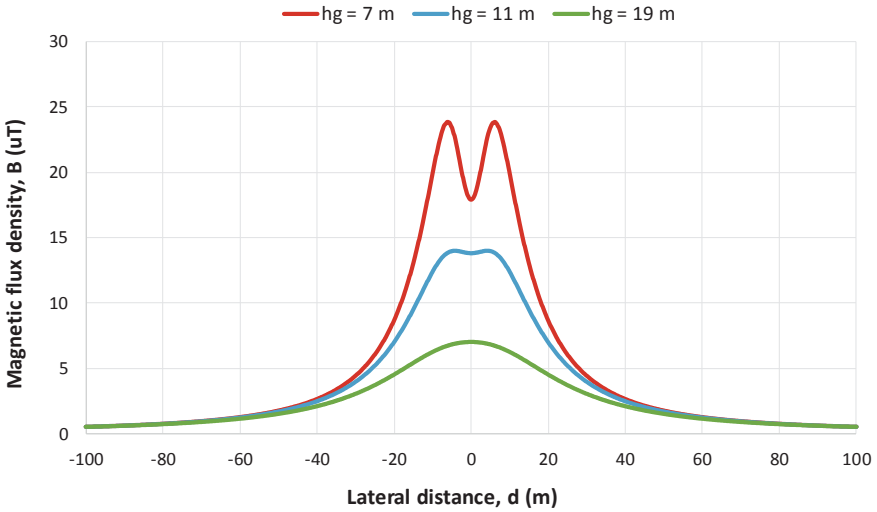

Fig. 20 RMS mag-netic flux density profiles for the 220 kV OHVPL, for untransposed phasing and various ground clearances

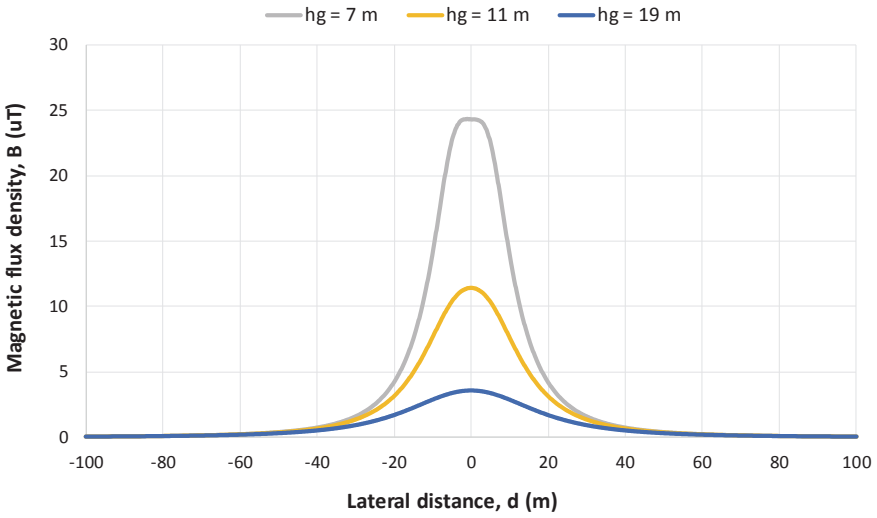

Fig. 21 RMS mag-netic flux density profiles for the 220 kV OHVPL, for transposed phasing and various ground clearances

Table 5 Typical magnetic field levels from the 220 kV OHVPL ($h_g = 11$ m, $I = 200$ A)

Phasing	B [μT], at various lateral distances				
	Maximum beneath line	*25 m*	*27.5 m*	*50 m*	*100 m*
U	2.87	1.07	0.93	0.35	0.11
T	2.35	0.42	0.34	0.076	0.01

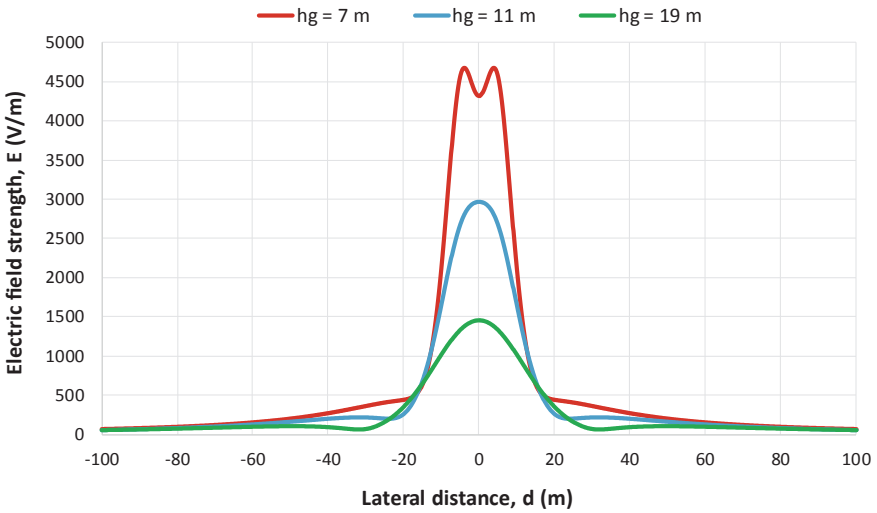

Fig. 22 RMS electric field strength profiles for the 220 kV OHVPL, for untransposed phasing and various ground clearances

the limit). For transposed phasing (Fig. 23), the maximum electric field strength at the same height lies in the range from 499.2 to 3653.9 V/m, which is below 73.1% of the ICNIRP exposure limit.

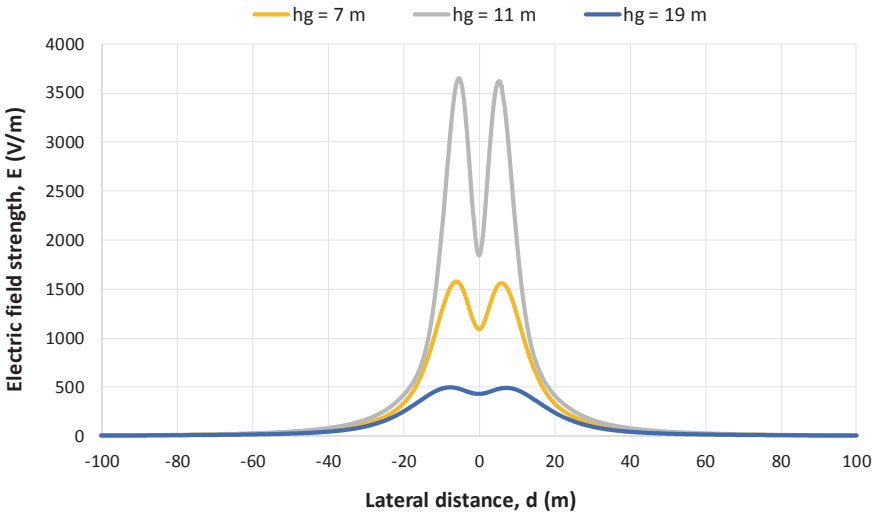

Fig. 23 RMS electric field strength profiles for the 220 kV OHVPL, for transposed phasing and various ground clearances

Table 6 Typical electric field levels from the 220 kV OHVPL ($h_g = 11$ m)

Phasing	E [V/m], at various lateral distances				
	Maximum beneath line	*25 m*	*27.5 m*	*50 m*	*100 m*
U	2969.5	207.6	215.9	161.7	60.5
T	1580	199	160	40	7.5

For the average clearance $h_g = 11$ m (Table 6), the electric field strength beneath the line reaches 2969.5 V/m for U phasing and 1580 V/m for T phasing, while the electric field strength at the corridor edge (27.5 m from the centerline) only reaches 215.9 V/m and 160 V/m, respectively. At 50 m from the OHVPL centerline, the electric field strength diminishes to 167.1 V/m and 40 V/m, respectively. As in the case of the 110 kV single-circuit OHVPL, such levels can also be measured at a distance of 30 cm from household appliances.

3.3 ELF-EMFs from the 400 kV Single-Circuit OHVPL

The last OHVPL selected for FE analysis is a 400 kV single-circuit line with geometry dictated by anchor portal towers of PAS 400.102 type. The line is equipped with two standard 450/75 mm^2 ACSR conductors per phase, with a distance between individual conductors of 0.4 m. The input data for this line are presented in Table 7, where the ground clearance h_g is taken 8.2 m, 12.6 m and 21.4 m, respectively. Magnetic field computations assume a maximum current of 1950 A.

a. *Magnetic field distribution*

The RMS magnetic flux density distribution at the height $h = 1$ m is illustrated in Fig. 24. As with the other investigated OHVPLs, the magnetic field beneath the 400 kV line does not exceed the ICNIRP exposure limit for general public, but at mid-span it can be as high as 57.4 μT, which represents more than half of this limit. Towards the tower, it falls to only 14.85% of the limit.

Table 7 Input data for the 400 kV single-circuit OHVPL using towers of PAS 400.102 type

Phase conductor	i	d_i [m]	hi [m]	$\underline{U_i}$ [kV]	$\underline{I_i}$ [A]
A	1	−11.50	h_g	$231 \angle 0°$	$975 \angle 0°$
	2	−11.10	h_g	$231 \angle 0°$	$975 \angle 0°$
B	3	−0.20	h_g	$231 \angle -120°$	$975 \angle -120°$
	4	0.20	h_g	$231 \angle -120°$	$975 \angle -120°$
C	5	11.10	h_g	$231 \angle 120°$	$975 \angle 120°$
	6	11.50	h_g	$231 \angle 120°$	$975 \angle 120°$

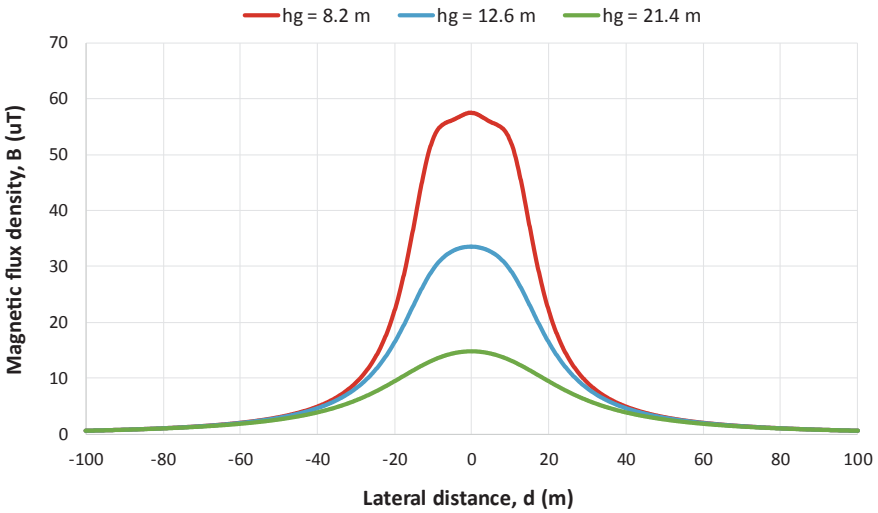

Fig. 24 RMS mag-netic flux density profiles for the 400 kV OHVPL, for various ground clearances

Table 8 Typical magnetic field levels from the 400 kV OHVPL ($h_g = 12.6$ m, $I = 450$ A)

B [μT], at various lateral distances				
Maximum beneath line	*25 m*	*37.5 m*	*50 m*	*100 m*
7.73	2.64	1.22	0.69	0.16

Once again, Table 8 gives magnetic field levels at various distances from the OHVPL centerline for the average clearance $h_g = 12.6$ m and a (normal) loading of 450 A. As it can easily be observed, the magnetic flux density at the OHVPL centerline is 7.73 μT, while at the edge of the OHVPL corridor—37.5 m from the centerline [41] —it decreases to only 1.22 μT. The critical value of 0.4 μT is reached at a lateral distance of about 65.1 m.

b. *Electric field distribution*

The RMS electric field strength distribution at the height $h = 1$ m is illustrated in Fig. 25. This time, the electric field at mid-span ($h_g = 8.2$ m) is about two times higher than the ICNIRP exposure limit for general public, namely 9145.3 V/m. Towards the tower ($h_g = 21.4$ m), the electric field strength falls to 1970.9 V/m (39.41% of the limit), but, as the ground clearance increases, the maximum field levels slightly move outside the line (for $h_g = 21.4$ m, the maximum field strength is recorded at a distance of 16 m from the OHVPL centerline).

Finally, Table 9 gives electric field levels for the average clearance $h_g = 12.6$ m. The electric field strength beneath the line reaches 4752 V/m, decreasing to 776.4 V/m at the corridor edge (37.5 m from the OHVPL centerline) and to 340.2 V/m at

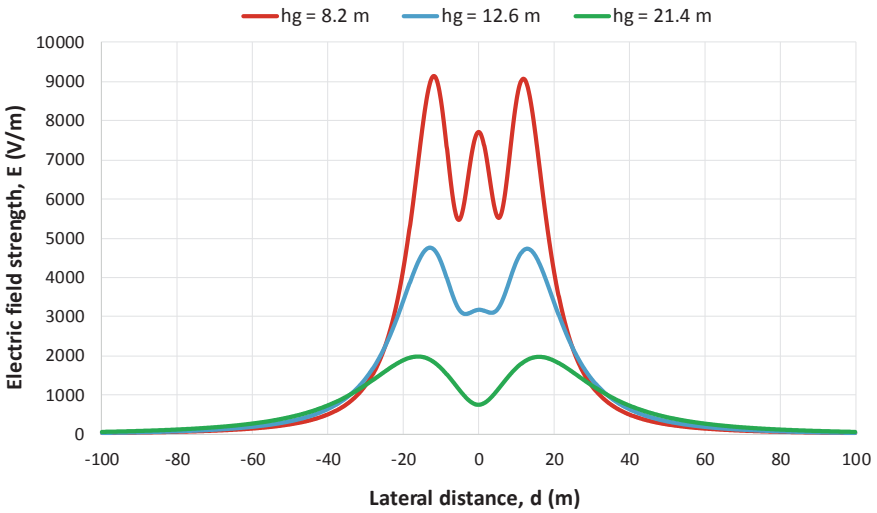

Fig. 25 RMS electric field strength profiles for the 400 kV OHVPL, for various ground clearances

Table 9 Typical electric field levels from the 400 kV OHVPL ($h_g = 12.6$ m)

E [V/m], at various lateral distances				
Maximum beneath line	*25 m*	*37.5 m*	*50 m*	*100 m*
4752	2212.7	776.4	340.2	44.1

50 m from the OHVPL centerline. At 100 m lateral distance, the electric field drops drastically, to only 44.1 V/m.

c. *Alternative computation approach*

All computations performed above assume that each sub-conductor of the considered 400 kV single-circuit OHVPL is modeled separately. However, this model can be simplified by replacing each of the three bundled conductors with an equivalent conductor of radius R_{eq}, given by [42]:

$$R_{eq} = \sqrt[N]{R \cdot d^{(N-1)}}, \tag{3}$$

where N stands for the number of sub-conductors in bundle, R represents the radius of a sub-conductor and d is the separation distance between sub-conductors. Equation (3) is applicable for up to three conductors per bundle, in our case leading to $R_{eq} = 76.485$ mm.

Figure 26 compares RMS magnetic flux density profiles computed with ANSYS Maxwell 2D by both approaches, as well as with PowerMAG software, which makes

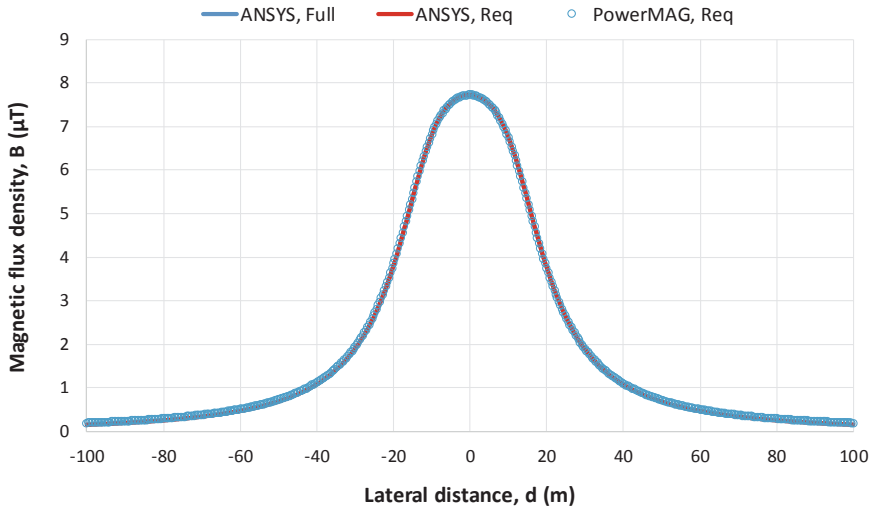

Fig. 26 Comparison between RMS magnetic flux density profiles obtained by the two approaches with ANSYS Maxwell 2D and PowerMAG software ($h_g = 12.6$ m, $I = 450$ A)

use of equivalent conductor model. As it can be observed, there is an excellent agreement between the three magnetic field profiles.

Similarly, Fig. 27 compares RMS electric field strength profiles computed with ANSYS Maxwell 2D by both approaches, as well as with PowerELT software, which

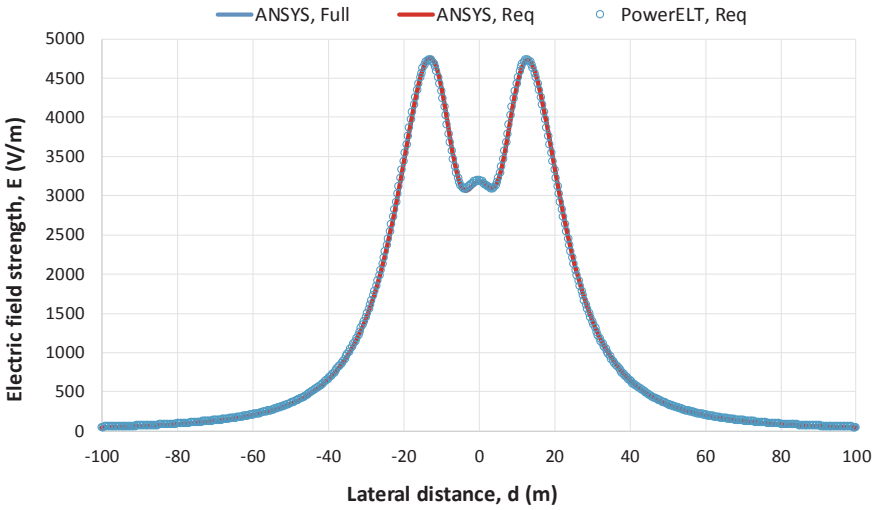

Fig. 27 Comparison between RMS electric field strength profiles obtained by the two approaches with ANSYS Maxwell 2D and PowerELT software ($h_g = 12.6$ m)

also makes use of equivalent conductor model. And this time, an excellent agreement between the three electric field profiles can be observed.

4 Conclusions

This chapter has been devoted to computing and analyzing ELF electric and magnetic fields emitted by typical configurations of OHVPLs used in Romania. All computations have been conducted using a 2D ANSYS Maxwell finite element model, strictly verified by quasi-static analytical methods. According to the obtained results, the highest exposure levels to ELF electric fields are associated with the 400 kV OHVPLs, directly beneath the line approaching the double of the ICNIRP limit for general public. As for ELF magnetic fields, the highest exposure levels are also associated with the 400 kV OHVPLs, but they are approaching only 60% of the ICNIRP limit. At the edge of the line corridor, the typical ELF electric and magnetic fields originating on the investigated OHVPLs are well below the specified limits, regardless the nominal voltage of the line. The computed ELF-EMF exposure levels are in line with those determined for similar OHVPLs in other countries.

References

1. Ahlbom A, Day N, Feychting M et al (2000) A pooled analysis of magnetic fields and childhood leukaemia. Br J Cancer 83:692–698
2. Greenland S, Sheppard AR, Kaune WT et al (2000) A pooled analysis of magnetic fields, wire codes, and childhood leukemia. Child Leuk-EMF Study Grop Epidemiol 11:624–634
3. IARC Working Group (2002) IARC monographs on the evaluation of carcinogenic risks to humans series. Non-ionizing radiation, Part 1: static and extremely low-frequency (ELF) electric and magnetic fields, vol. 80. IARC Press, Lyon. https://monographs.iarc.fr/ENG/Monographs/vol80/mono80.pdf. Last accessed 28 Sept 2019
4. ICNIRP (1998) Guidelines for limiting exposure to time-varying electric, magnetic and electromagnetic fields (up to 300 GHz). Health Phys 74:494–522
5. IEEE (2002) C95.6-2002 IEEE standard for safety levels with respect to human exposure to electromagnetic fields 0 to 3 kHz, New York
6. Porsius JT, Claassen L, Smid T, et al (2014) Health responses to a new high-voltage power line route: design of a quasi-experimental prospective field study in the Netherlands. BMC Public Health 14(237):1–12. https://www.ncbi.nlm.nih.gov/pmc/articles/PMC3975333/#B8. Last accessed 28 Sept 2019
7. Porsius JT, Claassen L, Smid T et al (2015) Symptom reporting after the introduction of a new high-voltage power line: a prospective field study. Environ Res 138:112–117
8. Sahbudin RKZ, Fauzi SA, Hitam S et al (2010) Investigation of electrical potential and electromagnetic field for overhead high voltage power lines in Malaysia. J Appl Sci 10(22):2862–2868
9. Elhabashi SM, Ehtaiba JE (2007) Electric fields intensity around the new 400 kV power transmission lines in libya. In: Proceedings of the 6th WSEAS international conference on circuits, systems, electronics, control and signal processing, Cairo, 29–31 Dec 2007, pp 390–398
10. EMFs.info (2019) Factors affecting the field from a power line. https://www.emfs.info/sources/overhead/factors/. Last accessed 28 Sept 2019

11. Vornicu S, Lunca E, Salceanu A (2019) ANSYS maxwell finite element model for 2D computation of the magnetic field generated by overhead high-voltage power lines. In: Proceedings of the 12th international conference and exhibition on electromechanical and energy systems (SIELMEN 2019), Chisinau, 10–11 Oct 2019, pp 382–385
12. Fuchs E, Masoum MAS (2008) Power quality in power systems and electrical machines. Elsevier Academic Press, Burlington
13. Olsen RG, Deno D, Baishiki RS et al (1988) Magnetic fields from electric power lines: theory and comparison to measurements. IEEE Trans Power Deliv 3(4):2127–2136
14. Vujević S, Lovrić T, Modrić T (2011) 2D computation and measurement of electric and magnetic fields of overhead electric power lines. In: Proceedings of the joint 3rd international workshop on nonlinear dynamics and synchronization (INDS'11) & 16th international symposium on theoretical electrical engineering (ISTET'11), Klagenfurt, 25–27 July 2011, pp 1–6
15. Kokoruš M, et al (2014) Analysis of the possible solutions for the reduction of electric and magnetic fields near 400 kV overhead transmission lines. In: Passerini G, Brebbia CA (eds) Environmental impact II. 2nd international conference on environmental and economic impact on sustainable development, Ancona, May 2014. WIT transactions on ecology and the environment, vol. 181. WIT Press, Southampton, p 225
16. Ellithy K, Al-Suwaidi S, Elsayed H (2011) Measuring human exposure to magnetic fields near EHV 400 kV GIS substation and power lines in state of qatar. In: Proceedings of the north American power symposium (NAPS 2011). Boston, 4–6 Aug 2011, pp 1–6
17. Medved D, Mišenčík L, Kolcun M, et al (2015) Measuring of magnetic field around power lines. In: Proceedings of the 8th international scientific symposium ELEKTROENERGETIKA 2015. Stará Lesná, 16–18 Sept 2015, pp 148–151
18. Vergara XP, Kavet R, Crespi CM et al (2015) Estimating magnetic fields of homes near transmission lines in the California power line study. Environ Res 140:514–523
19. Tourab W, Babouri A (2016) Measurement and modeling of personal exposure to the electric and magnetic fields in the vicinity of high voltage power lines. Saf Health Work 7(2):102–110
20. Filippopoulos G, Tsanakas DK (2005) Analytical calculation of the magnetic field produced by electric power lines. IEEE Trans Power Deliv 20(2):1474–1482
21. Moro F, Turri R (2008) Fast analytical computation of power-line magnetic fields by complex vector method. IEEE Trans Power Deliv 23(2):1042–1048
22. Ztoupis IN, Gonos IF, Stathopulos IA (2013) Calculation of power frequency fields from high voltage overhead lines in residential areas. In: Proceedings of the 18th international symposium on high voltage engineering. Seoul, 25–30 Aug 2013, pp 61–66
23. Milutinov M, Juhas A, Prša M (2007) Electric field strength and polarization of multi three-phase power lines. In: Proceedings of the 8th international conference on applied electromagnetics. Niš, 3–5 Sept 2007, pp 1–4
24. Milutinov M, Juhas A, Prša M (2009) Electromagnetic field underneath overhead high voltage power line. In: Proceedings of the 4th international conference on engineering technologies. Novi Sad, 28–30 April 2009, pp 1–5
25. Al Salameh MSH, Hassouna MAS (2010) Arranging overhead power line conductors using swarm intelligence technique to minimize electromagnetic fields. Prog Electromagn Res B 26:213–236
26. Gouda OE, Amer GM, Salem WA (2009) Computational aspects of electromagnetic fields near H.V. Transmission lines. Energy Power Eng 1(2):65–71
27. Lunca E, Istrate M, Salceanu A et al (2012) Computation of the magnetic field exposure from 110 kV overhead power lines. In: Proceedings of the 7th international conference on electrical and power engineering. Iasi, 25–27 Oct 2012, pp 628–631
28. Lunca E, Ursache S, Salceanu A (2018) Computation and analysis of the extremely low frequency electric and magnetic fields generated by two designs of 400 kV overhead transmission lines. Measurement 124:197–204
29. Razavipour SS, Jahangiri M, Sadeghipoor H (2012) Electrical field around the overhead transmission lines. World Acad Sci Eng Technol 6(2):168–171

30. Lunca E, Istrate M, Salceanu A (2013) Comparative analysis of the extremely low-frequency magnetic field exposure from overhead power lines. Environ Eng Manag J 12(6):1145–1152
31. Ali Rachedi B, Babouri A, Berrouk F (2014) A study of electromagnetic field generated by high voltage lines using COMSOL MULTIPHYSICS. In: Proceedings of the 2014 international conference on electrical sciences and technologies in Maghreb. Tunis, 3–6 Nov 2014, pp 1–5
32. Salceanu A, Lunca E, Paulet M (2017) Affordable evaluation of low frequency electric fields from the standpoint of directive 2013/35/EU. ACTA IMEKO 6(4):37–45
33. Lunca E, Vornicu S, Salceanu A et al (2018) 2D Finite element model for computing the electric field strength-rms generated by overhead power lines. J Phys Conf Ser 1065:1–4
34. EU (1999) 1999/519/EC: Council recommendation of 12 July 1999 on the limitation of exposure of the general public to electromagnetic fields (0 Hz to 300 GHz). https://publications.europa.eu/en/publication-detail/-/publication/9509b04f-1df0-4221-bfa2-c7af77975556/language-en. Last accessed 28 Sept 2019
35. Braicu SF, et al (2017) Evaluation of the electric and magnetic field near high voltage power lines. In: Vlad S, Roman NM (eds) MEDITECH 2016. 5th international conference on advancements of medicine and health care through technology. Cluj-Napoca, 2016. IFMBE proceedings, vol. 59, Springer International Publishing, p 141
36. Ghani SA, Ahmad Khiar MS, Chairul IS, et al (2014) Study of magnetic fields produced by transmission line tower using finite element method (FEM). In: Proceedings of the 2nd international conference on technology, informatics, management, engineering & environment. Bandung, 19–21 Aug 2014, pp 64–68
37. EMFs.info (2019) Phasing—how the phasing affects the field produced by an overhead line. https://www.emfs.info/sources/overhead/factors/phasing/. Last accessed 28 Sept 2019
38. Ponnle AA, Adedeji KB, Abe BT et al (2017) Variation in phase shift of phase arrangements on magnetic field underneath overhead double-circuit HVTLs: field distribution and polarization study. Prog Electromagn Res M 56:157–167
39. Lunca E, Ursache S, Salceanu A (2017) Characterization of the electric and magnetic field exposure from a 400 kV overhead power transmission line in Romania. In: Proceedings of the 22nd IMEKO TC4 international symposium and 20th international workshop on ADC modelling and testing. Iasi, 14–15 Sept 2017, pp 239–243
40. Transelectrica (2019) Power transmission grid. https://www.transelectrica.ro/en/web/tel/date-generale-management. Last accessed 28 Sept 2019
41. ANRE (2007) Technical norm regarding the delimitation of the protection and safety zones associated with energy capacities—Revision I of 09 March 2007
42. Grigsby LL (2012) Electric power generation, transmission, and distribution, 3rd edn. CRC Press, Boca Raton

2D Finite Element Model for computing the electric field strength-rms generated by overhead power lines

2D Finite Element Model for computing the electric field strength-rms generated by overhead power lines

E Lunca[1], **S Vornicu**[1], **A Salceanu**[1,2] and **O Bejenaru**[1]
[1]Gheorghe Asachi" Technical University of Iasi, Faculty of Electrical Engineering

E-mail: asalcean@tuiasi.ro

Abstract. In this article, a simple 2D finite element model is proposed for computing the RMS electric field strength generated by overhead power lines. The model it is implemented in FEMM 4.2, a high quality, open source finite element software for solving low frequency electromagnetic problems, for the particular case of a 110 kV single-circuit overhead power line. The results obtained with this model there are analyzed and then compared to those obtained by analytical calculations, revealing a very good agreement. The proposed FEMM 4.2 model it is primarily intended to assess the compliance with the electric field exposure limits established by health regulations, but other applications are also possible.

1. Introduction

The overhead power lines (OPLs) are structures used for electric power transmission and distribution along large distances, consisting of conductors suspended by towers or poles [1]. All OPLs produce extremely low frequency (ELF) electric and magnetic fields, which can induce electrical currents within the human body. Consequently, in order to check the compliance with the exposure limits established by health regulations, such as those published by the International Commission on Non-Ionizing Radiation Protection (ICNIRP) in 1998 [2] and 2010 [3], these ELF fields need to be properly assessed. For this purpose, measurements and theoretical computations are complementarily performed.

The computation of the ELF electric and magnetic fields emitted by overhead power lines can be achieved by both analytical and numerical methods [4-9], often employing expensive general software. We here propose a simple 2D numerical model for computation of the electric field strength, which is based on Finite Element Method Magnetics 4.2 (FEMM 4.2) [10], open source finite element software for solving low frequency electromagnetic problems on 2D planar and axisymmetric domains. Previous results obtained with this FEMM model were only briefly presented in [11], for the particular case of a 110 kV double-circuit line commonly encountered in the Romanian power system. A finite element model for computation of the magnetic flux density in the vicinity of OPLs, also based on FEMM software, was presented by the authors in [12].

The rest of the paper is structured as follows: Section 2 details the construction of the FEMM model for a typical 110 kV single-circuit OPL, as well as the methodology adopted for determination of the RMS values of the electric field strength; Section 3 presents representative results – lateral profiles

[2] To whom any correspondence should be addressed.

and 2D planar distributions of electric field strength – obtained for the considered OPL; Section 4 draws the conclusions.

2. FEMM model for a 110 kV single-circuit OPL

The 110 kV single-circuit line proposed for study has its geometry imposed by normal suspension towers of Sn 110.102 type, according to data from Table 1. The three phases (A, B and C) are equipped with ACSR (Aluminium Conductor Steel Reinforced) conductors of section 185/32 mm^2 (19.2 mm exterior diameter and 7.2 mm core diameter). The ground wire (GW) consists of a 95/55 mm^2 ACSR conductor (16 mm exterior diameter and 9.6 mm core diameter). The ground clearance of the line is assumed to be h_g = 10 m, an intermediate one.

Table 1. Geometrical parameters of the 110 kV single-circuit overhead power line.

Conductor	i	x_i (m)	y_i (m)
Phase A	1	4.35	h_g
Phase B	2	2.85	h_g + 4.20
Phase C	3	-4.35	h_g
GW	4	0.00	h_g + 9.50

The global FEMM model of the 110 kV single-circuit overhead power line is presented in Figure 1, discretized by a mesh of 494839 triangular elements and 247613 nodes. The boundary conditions applied to this model assume that the scalar electric potential at the ground level and along the semi-circular boundary is zero (U = 0). The air region surrounding the power line (limited by the previously established boundary) is taken large enough to neglect the side effects, having a radius of at least 10 times the arrangement dimensions.

The four ACSR conductors are modelled as presented in Figure 2, using the following electric parameters: for aluminium (Al), $\sigma = 3.77 \cdot 10^7$ S/m and ε_r = 1; for steel (Ol, internal symbol), $\sigma = 0.56 \cdot 10^7$ S/m and ε_r = 1.

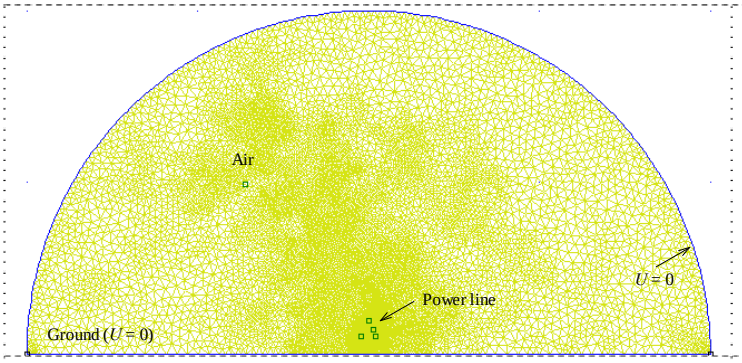

Figure 1. Discretized global FEMM model of the 110 kV single-circuit overhead power line.

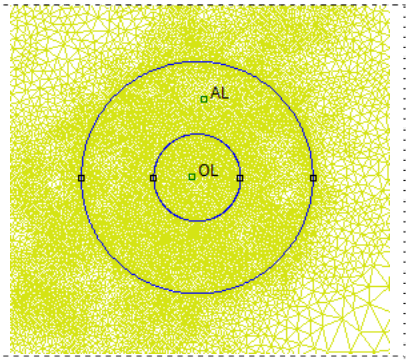

Figure 2. Detailed model for an ACSR conductor.

The model is implemented using the "current flow" module of FEMM 4.2, which generally allows to determine electric field distributions, voltage (potential) distributions, current densities, etc. By imposing adequate "fixed voltages" on the conductors, it is possible to obtain electric field distributions around the power line at different time instants over a 20 ms period. The RMS values of the electric field strength along a defined contour – a lateral profile, for instance – might be calculated by taking multiple distributions, equally-spaced over a 20 ms period. The RMS calculations performed

in this study assume 40 electric field strength distributions ("density plots"), corresponding to the instantaneous phase voltages presented in Figure 3.

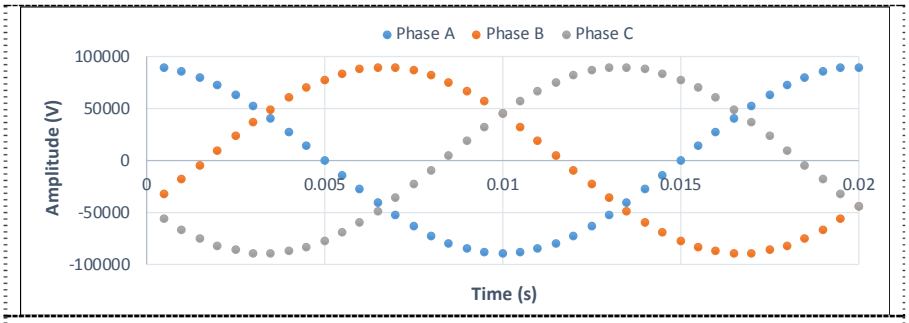

Figure 3. Instantaneous phase voltages imposed on the conductors for computing the RMS electric field strength.

3. Simulation results

Figure 4 shows the lateral profiles of the electric field strength at the considered time moments, taken at the standard height of 1 m above the ground, as well as the lateral profile of the computed RMS electric field strength (blue thick line). The unperturbed RMS electric field strength under the power line does not exceed 994.1 V/m, which is 5.02 times below the ICNIRP limit for general public exposure, 5 kV/m; at the edge of the power line corridor (18.5 m from the centreline), the RMS electric field strength decreases to about 260 V/m, which is 19.23 times below the aforementioned exposure limit.

Figure 5 compares the lateral profiles of the RMS electric field strength obtained by the described FEMM model with those analytically obtained, using the simulation software proposed by the authors in [13]. As it can easily be seen, there is good concordance between the results provided by the two methods.

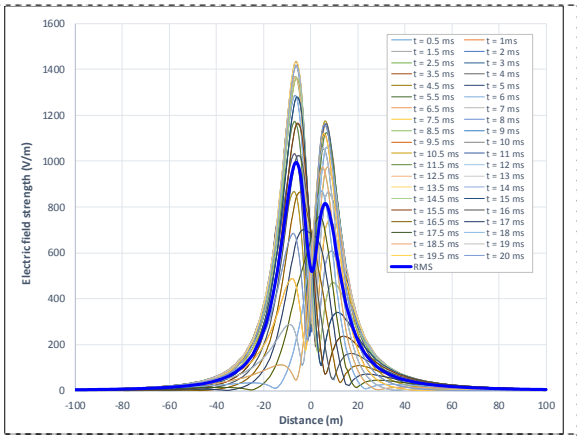

Figure 4. Lateral profiles of the momentary and RMS electric field strength at the height of 1 m above the ground.

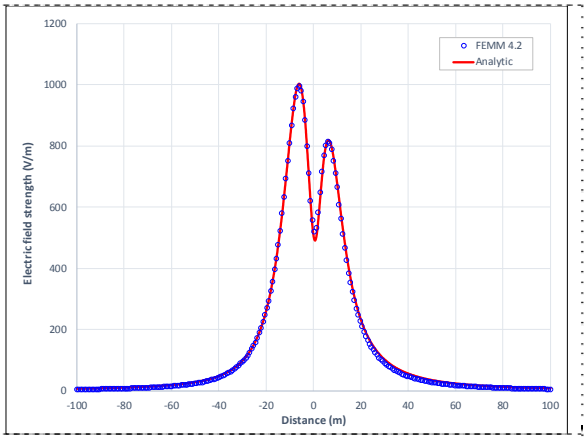

Figure 5. Comparison between lateral profiles of RMS electric field strength obtained with FEMM 4.2 and analytical calculations.

Figure 6 presents the distribution of the electric field strength around the 110 kV single-circuit OPL at the time instant t = 13.5 ms, corresponding to the maximum lateral profile in Figure 4. Comparing the field levels in this distribution to the 5 kV/m (RMS) limit will provide a safety margin, but it has to be mentioned that the electric field strength reaches this limit value only at a fairly high height, approximately 7.5 m. The distribution of the electric potential at t = 13.5 ms is presented in Figure 7.

4. Conclusions

The main result of this study is the development of a simple but effective FEMM 4.2 model for computing the RMS electric field strength surrounding the overhead power lines. The model is primarily intended to verify the compliance with the ELF exposure limits established by health regulations, but other applications can easily be identified. Lateral profiles of the RMS electric field strength obtained with the proposed model and similar profiles obtained by software based on a quasi-static analytical approach were compared, revealing a very good agreement. As future development, we intend to automatically calculate the RMS values of electric field strength.

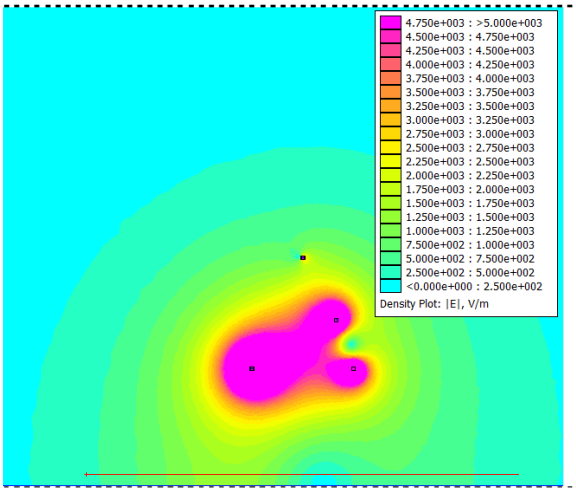

Figure 6. The distribution of the electric field strength around the 110 kV single-circuit OPL at the time instant t = 13.5 ms.

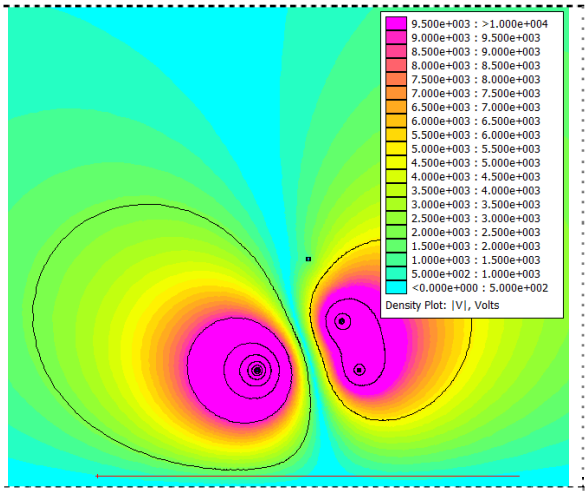

Figure 7. The distribution of the electric potential around the 110 kV single-circuit OPL at the time instant t = 13.5 ms.

5. References

[1] Tewari J P 2003 *Basic Electrical Engineering* (New Delhi: New Age International)
[2] ICNIRP 1998 *Health Phys.* **74** 494
[3] ICNIRP 2010 *Health Phys.* **99** 818
[4] Ali Rachedi B, Babouri A and Berrouk F 2014 A study of electromagnetic field generated by high voltage lines using COMSOL MULTIPHYSICS *Proc. 2014 Int. Conf. on Electrical Sciences and Technologies in Maghreb (Tunis, Tunisia, 3–6 November 2014)* pp 1–5
[5] Xiao L and Holbert K E 2014 Development of software for calculating electromagnetic fields near power lines *North American Power Symp. (Pullman, U.S., 7–9 September 2014)* pp 1–6
[6] Ahmadi H, Mohseni S and Shayegani-Akmal A A 2010 *Iran. J. Environ. Health Sci. Eng.* **7** 181
[7] Razavipour S S, Jahangiri M and Sadeghipoor H 2012 *World Acad. Sci. Eng. Technol.* **6** 168
[8] Milutinov M, Juhas A and Prša M 2009 Electromagnetic Field underneath Overhead High Voltage Power Line *Proc. 4th Int. Conf. on Engineering Technologies (Serbia, Novi Sad, 28–30 April 2009)* pp 1–5
[9] Filippopoulos G and Tsanakas D K 2005 *IEEE Trans. Power Delivery* **20** 1474
[10] Meeker D 2015 Finite Element Method Magnetics Version 4.2 *User's Manual*
[11] Salceanu A, Lunca E and Paulet M 2017 *ACTA IMEKO* **6** 37
[12] Lunca E, Istrate M and Salceanu A 2013 Environ. Eng. Manag. J. **12** 1145
[13] Lunca E, Ursache S and Salceanu A 2017 Characterization of the Electric and Magnetic Field Exposure from a 400 kV Overhead Power Transmission Line in Romania *Proc. 22nd IMEKO TC4 Int. Symp. and 20th Int. Workshop on ADC Modelling and Testing (Romania, Iasi, 14–15 September 2017)* pp 1-5

Measurement and Numerical Simulation of the Low-Frequency Electric Field Generated by an Overhead Power Line

2022 International Conference and Exposition on Electrical And Power Engineering (EPE) | 978-1-6654-8994-2/22/$31.00 ©2022 IEEE | DOI: 10.1109/EPE56121.2022.9959872

Eduard Lunca
Department of Electrical Measurements and Materials
Technical University of Iasi
Iasi, Romania
elunca@tuiasi.ro

Silviu Vornicu
Department of Electrical Measurements and Materials
Technical University of Iasi
Iasi, Romania
silviusieca@gmail.com

Ionel Pavel
Department of Electrical Measurements and Materials
Technical University of Iasi
Iasi, Romania
ionelpavel7@tuiasi.ro

Mihai Andrusca
Department of Power Systems
Technical University of Iasi
Iasi, Romania
mandrusca@tuiasi.ro

***Abstract*—In this study, the low-frequency electric field generated by a 110-kV double-circuit overhead power line is comparatively assessed by measurements and numerical simulations. Measurements were performed with a self-developed 5 Hz – 2 kHz electric field sensor (EFS-01) in conjunction with a portable signal analyzing device, i.e. Fluke 43 single-phase power quality analyzer, while simulations were performed using a 2D finite element model developed in ANSYS Maxwell 2D. The results obtained by the two methods are in good agreement and in line with expected exposure field levels for such types of 110-kV overhead power lines.**

Keywords—electric field, electric field sensor, overhead power line, measurement, numerical simulation

I. Introduction

The overhead power lines (OPLs) are significant sources of low-frequency electric and magnetic fields. Usually, these fields reach the highest levels directly under the line, but they quickly diminish with distance from the OPL. In addition to distance, there are other factors influencing the electric and magnetic field distribution around an OPL, including voltage, current, ground clearance, evaluation height from the ground, physical phasing, balance within circuit and balance between circuits, ground conductivity, parallel lines, etc. Furthermore, the trees, bushes, fences and buildings naturally reduce the electric fields generated by OPLs, but the magnetic fields pass through the most materials and objects [1, 2].

Since the magnetic field is directly linked to the current flowing on the line (line load), it typically shows daily and seasonal variation patterns. On the other hand, the electric field, which is proportional to voltage, changes very little in time because of the line's stable voltage. Both fields can be either measured using a "field meter" or (quite accurately) computed based on power line geometry and information on current and voltage, respectively. Measuring electric fields is harder than measuring magnetic fields because the person taking the measurement often perturbs the field [3].

There are many studies dealing with the measurement and simulation of low-frequency electric and magnetic fields produced by OPLs, especially from human exposure point of view [2, 4-13]. However, comparative assessments were only rarely performed [14-16], while most of them were focused on magnetic fields (probably because of the statistical association between these fields and childhood leukemia). This is why, in this study, the electric field associated with a common 110-kV double-circuit OPL is comparatively assessed by measurements under real conditions and numerical simulations.

Comparisons were performed in terms of RMS electric field strength profiles taken at the height of 1 m above ground level, as usually considered in exposure studies. For this purpose, special emphasis was put in the development and calibration of an active electric field sensor, called EFS-01, which offers a very flat frequency response from 5 Hz to 2 kHz and is configured to measure electric field strengths from about 1 V/m to more than 50 kV/m. On the other side, numerical simulations were performed with ANSYS Maxwell 2D, by adopting a 2D finite element model derived from that proposed in a recent study [17].

The rest of this research paper is structured as follows: Section II summarizes the OPL's characteristics; Section III gives details about instrumentation and measurements; Section IV focuses on the 2D finite element model used for numerical simulations; Section V compares measurement and simulation results and check them against the ICNIRP limit for general public exposure; Section VI draws conclusions.

II. Electrical and Geometrical Characteristics of the Considered 110-kV Double-circuit OPL

The selected 110-kV double-circuit OPL is a typical power distribution line often found in urban areas and their proximity. Fig. 1 and Table I summarize the geometrical and electrical characteristics of the considered 110-kV OPL, mainly required for numerical simulation. The two circuits are equipped with ACSR conductors of section 300/50 mm^2 (exterior diameter of 24.2 mm), while the shield wire (SW) consists of an 160/95 mm^2 ACSR conductor (exterior diameter of 20.75 mm). As we can see, the same phase sequence is employed in both circuits, which clearly produces the maximum field levels to the sides of the line. The RMS values of the phase-to-ground voltages (at the measurement time), U_i, were obtained from the power distribution company, while the conductor heights above ground, y_i, were measured with a Suparule Model 600E cable height meter. The separation distances between phases, x_i, were chosen according to the used type of suspension tower, Sn 110.252.

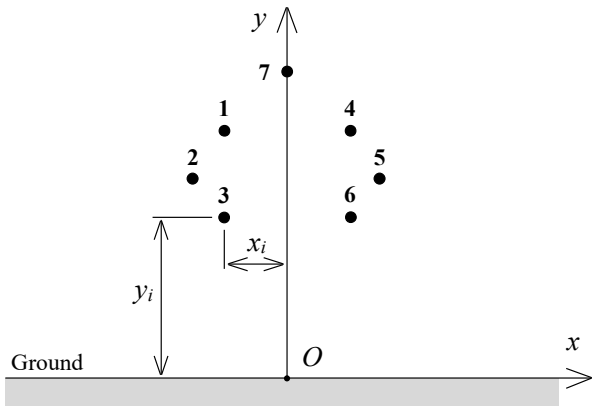

Fig. 1. Cross section of the 110-kV double-circuit OPL.

TABLE I. GEOMETRICAL AND ELECTRICAL CHARACTERISTICS OF THE SELECTED 110-KV DOUBLE-CIRCUIT OVERHEAD POWER LINE

Line conductor	i	x_i (m)	y_i (m)	D_i (mm)	$\underline{U_i}$ (kV)
Phase I	1	-3.1	20.12	24.2	68.4 ∠ 0°
Phase II	2	-4.7	15.44	24.2	68.3 ∠ -120°
Phase III	3	-3.1	10.77	24.2	68.2 ∠ 120°
Phase I	4	3.1	20.4	24.2	68.3 ∠ 0°
Phase II	5	4.7	15.4	24.2	68.2 ∠ -120°
Phase III	6	3.1	10.85	24.2	68.5 ∠ 120°
SW	7	0	26.2	20.75	0 ∠ 0°

III. INSTRUMENTATION AND MEASUREMENTS

A. Instrumentation

Generally, near the ground surface, the electric field generated by an OPL is nearly vertical and nearly linearly polarized, a consequence of the fact that the ground itself is conducting. To measure such fields, we designed a single-axis electric field sensor, EFS-01, which basically consists of a circular pickup probe connected to a signal processing circuit, as depicted in Fig. 2. The pickup probe is fabricated from a double-sided PCB disk, in the form of two closely spaced electrodes: an active (electrode) disk with the diameter d = 58 mm – surrounded by a guard ring – on the top side and the reference backside (electrode) disk of diameter $D \approx 3d$. The active disk is connected to the inverting input of an op-amp with capacitive feedback, while the non-inverting input of the op-amp, the guard ring and the backside disk are connected together to ground. In this way, the displacement current (I) induced by the electric field E on the active surface (A) is converted to an equivalent voltage (U), according to the formula [18]:

$$U = \frac{\varepsilon_0 \cdot E \cdot A}{C}, \qquad (1)$$

where C is the capacitance in the feedback loop of the op-amp and ε_0 is the permittivity of free space ($8.85 \cdot 10^{-12}$ F/m).

In order to prevent field distortion caused by unwanted emissions, this low-level voltage is fed into a 4th order high-pass Butterworth filter with the cutoff frequency of 5 Hz (attenuation of 80 dB/dec below 5 Hz) and then into a 2nd order low-pass Butterworth filter with the cutoff frequency of 2 kHz (attenuation of 40 dB/dec above 2 kHz). After filtering, the voltage signal is passed to a manually controlled gain stage with 4 selectable gains (1, 10, 100 and 1000), implemented with an INA128 instrumentation amplifier, and finally applied to the input of an AC-coupled variable gain stage (2 ÷ 200), which is used to set out the sensor's overall sensitivity (S) during the calibration process. The electric field strength is determined very simple, by multiplying the RMS value of the output voltage (in this case, measured with the portable Fluke 43 power quality analyzer) by the selected scale factor, 1/S. The dual voltage supply for sensor, ±9 V, is provided by two 9 V batteries.

The sensor accuracy is derived from a sinusoidal calibration field, E_c = 200 V/m, established with a parallel plate arrangement (air dielectric). After setting the overall sensitivity, the frequency response of the sensor was tested at twelve frequencies varying from 5 Hz to 2 kHz, as presented in Fig. 3. As it can be seen, in the frequency range from 20 Hz to 1 kHz, the frequency response flatness is within -0.3/+0.1 dB. Depending on the selected measurement range (sensitivity), the sensor is able to measure electric field strengths from about 1 V/m to 50 kV/m, which virtually covers all situations for the intended use.

B. Measurements

The field assessment was conducted close to mid-span, as illustrated in Fig. 4. During measurements, the sensor was mounted on a 1-m non-conductive tripod, parallel to the power line conductors, with the active disk facing upward. Electric field waveform measurements were taken at 41 locations in the cross section of the OPL, up to 20 m from the centerline, with at least 2 m distance between sensor and operator position. The air temperature was 20.3 °C (October 2022) and the terrain in the cross section of the OPL was relatively smooth.

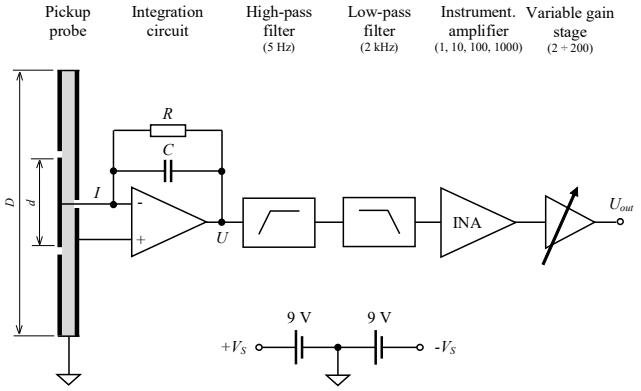

Fig. 2. Block diagram of the single-axis electric field sensor.

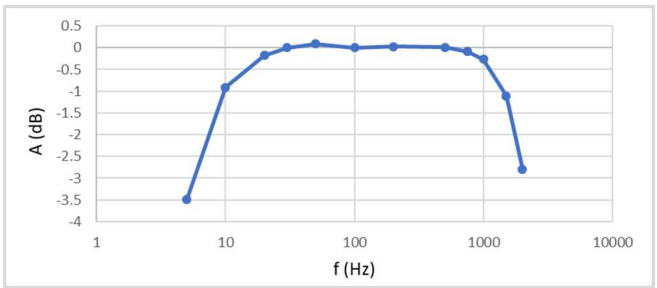

Fig. 3. The frequency response of the single-axis electric field sensor (measured at the field strength of 200 V/m).

Fig. 4. Electric field measurements under the 110-kV OPL.

IV. Numerical Simulation

The ANSYS Maxwell 2D model used for numerical simulation is illustrated in Fig. 5, where the 110-kV double-circuit OPL is located above a ground with the electrical conductivity σ_g = 0.05 S/m and the relative permittivity ε_r = 10, according to the heights and separation distances in Table I. All conductors are modeled as aluminum cylinders with the electrical conductivity $\sigma_c = 3.8 \cdot 10^7$ S/m and proper diameters (very important role in electric field estimation), energized with the measured phase-to-ground voltages ($\underline{U}_i$). In addition, Balloon boundary conditions are assigned, which model the region outside the delimited space as being infinitely large. Field calculations are performed using the *AC conduction solver*.

The RMS electric field strength at the height of 1 m above ground is derived from a sufficiently large number of instantaneous electric field strength profiles taken over a 20-ms period (Fig. 6.a), using the formula [17]:

$$E_{RMS}(k) = \sqrt{\frac{1}{N}\left(E_1^2(k) + E_2^2(k) + \ldots + E_N^2(k)\right)}, \qquad (2)$$

where $E_1(k)$, …, $E_N(k)$ are the instantaneous values of the electric field strength corresponding to the point k of the profile and N = 73 stands for the total number of values.

A distribution of the electric field around the power line is presented in Fig. 6.b. As expected, close to the ground, the electric field is nearly vertical.

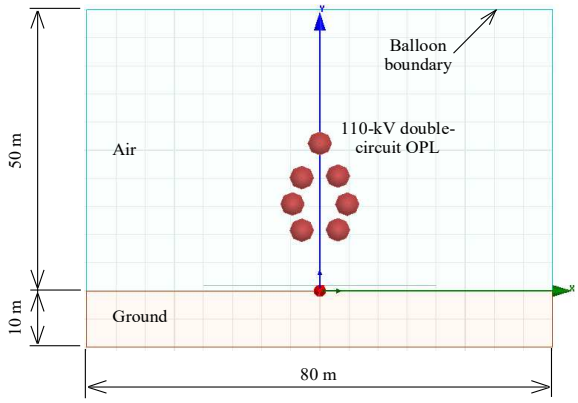

Fig. 5. Finite element modeling of the 110-kV double-circuit OPL.

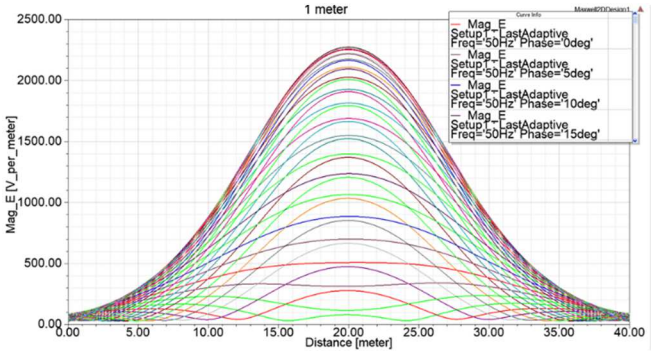

a)

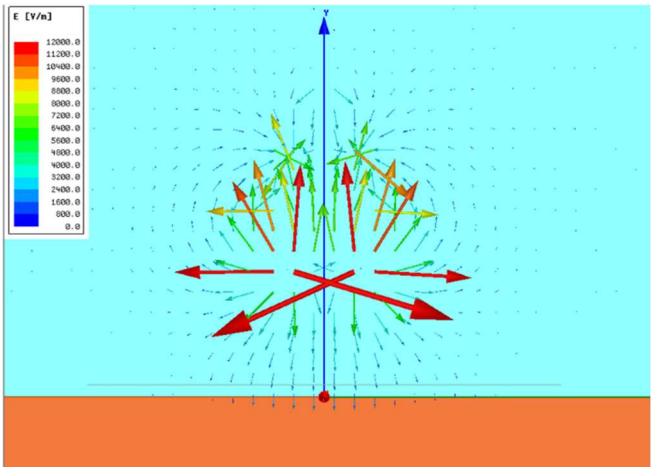

b)

Fig. 6. Results directly obtained with the proposed finite element model: a) lateral profiles of the instantaneous electric field strength at the height of 1 m above ground; b) example of electric field distribution around OPL.

V. Results

Fig. 7 graphically compares the measured E-field profile and the E-field profile calculated with Eq. (2). As it can easily be seen, there is a good correlation between the RMS electric field strength profiles obtained by the two methods. This can also be observed in Fig. 8, which gives percentage differences between measurements (E_{meas}) and calculations (E_{calc}) for all test points, determined with the formula:

$$diff(\%) = \frac{|E_{meas} - E_{calc}|}{\left[\frac{E_{meas} + E_{calc}}{2}\right]} \cdot 100 \,. \qquad (3)$$

All percentage differences are below 23.2%, while, for most of the points, they are below 15%. An error factor could be the terrain unevenness.

Field values at several distances from the centerline are presented in Table II, alongside the associated percentage of the ICNIRP reference level for general public (5 kV/m at 50 Hz) [19]. In accordance with the measured and simulated data, the electric field strength at the centerline (0 m) is around 32% of the ICNIRP reference level. At 20 m distance from the OPL centerline, the electric field strength falls to about 1.6% of the ICNIRP reference level, a value that can be found in the vicinity of many household and office appliances. In practice, it is possible to encounter slightly higher field levels from such type of overhead power lines, especially due to conductor sag.

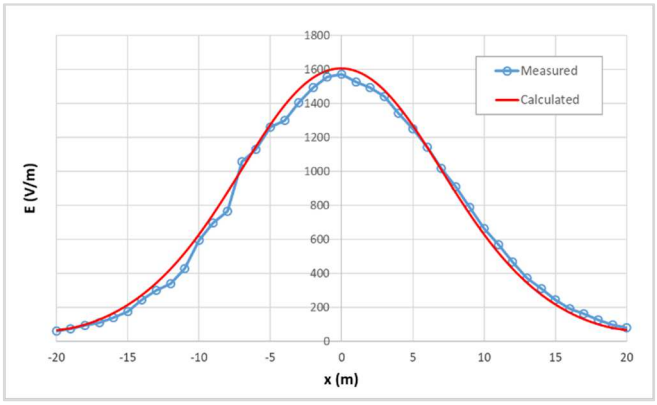

Fig. 7. Comparison between measurement and simulation results: RMS electric field strength profiles at the height of 1 m above ground.

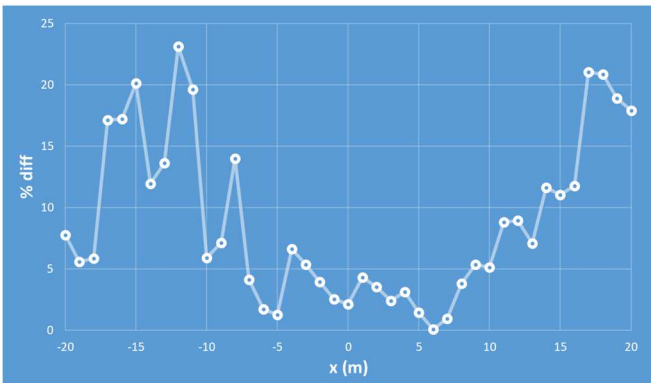

Fig. 8. Percentage differences between measurements and calculations.

TABLE II. RMS ELECTRIC FIELD STRENGTH AT SEVERAL DISTANCES FROM THE CENTERLINE AND COMPARISON TO ICNIRP LIMIT

Distance	RMS electric field strength, *E*(V/m)		% of ICNIRP exposure limit	
	Measured	*Calculated*	*Measured*	*Calculated*
0 m	1573.8	1607.6	31.5	32.2
5 m	1251.7	1269.9	25.0	25.4
10 m	662.4	629.2	13.2	12.6
15 m	242.8	217.4	4.9	4.3
20 m	80.5	67.3	1.6	1.3

VI. CONCLUSIONS

The measured and simulated electric fields associated with the selected 110-kV overhead power line correlate within acceptable limits, resulting in percentage differences below 23.2%. Based on the obtained data, it can also be concluded that the exposure levels from this common type of 110-kV OPL are quite small compared to the ICNIRP limit for general public, not exceeding 2% of the limit at a distance of 20 m from the centerline. As approaching the tower, the electric field levels are even lower.

REFERENCES

[1] EMFs.info, "Overhead power lines," online at http://www.emfs.info/sources/overhead/ (Accessed September 2022).

[2] S. Vornicu, E. Lunca, and A. Salceanu, "ANSYS Maxwell Finite Element Model for 2D Computation of the Magnetic Field Generated by Overhead High-Voltage Power Lines," 2019 International Conference on Electromechanical and Energy Systems (SIELMEN), 2019, pp. 1-4.

[3] X.P. Vergara, R. Kavet, C.M. Crespi, C. Hooper, J.M. Silva, and L. Kheifets, "Estimating magnetic fields of homes near transmission lines in the California Power Line Study," Environmental research, Vol. 140, pp. 514-523, 2015.

[4] E. Lunca, S. Vornicu, A. Salceanu, and O. Bejenaru, "2D Finite Element Model for computing the electric field strength-rms generated by overhead power lines," Journal of Physics: Conference Series, Vol. 1065, pp. 1-4, 2018.

[5] E. Lunca, S. Ursache, and A. Salceanu, "Characterization of the Electric and Magnetic Field Exposure from a 400 kV Overhead Power Transmission Line in Romania," 22nd IMEKO TC4 International Symposium and 20th International Workshop on ADC Modelling and Testing, Iasi, 2017, pp. 1-5.

[6] B. Ali Rachedi, A. Babouri, and F. Berrouk, "A study of electromagnetic field generated by high voltage lines using COMSOL MULTIPHYSICS," 2014 International Conference on Electrical Sciences and Technologies in Maghreb, Tunis, 2014, pp 1-5.

[7] L. Xiao and K.E Holbert, "Development of software for calculating electromagnetic fields near power lines," North American Power Symposium (NAPS 2014), Pullman, 2014, pp. 1-6.

[8] I.N. Ztoupis, I.F. Gonos, and I.A. Stathopulos, "Calculation of Power Frequency Fields from High Voltage Overhead Lines in Residential Areas," 18th International Symposium on High Voltage Engineering, Seoul, 2013, pp. 61-66.

[9] M. Nafar, "Magnetic Field Calculation Around 230 kV Bundled Transmission Lines," International Journal of Engineering Innovation & Research, Vol. 2, No. 6, pp. 463-466, 2013.

[10] E. Lunca, M. Istrate, A. Salceanu, and S. Tibuliac, "Computation of the Magnetic Field Exposure from 110 kV Overhead Power Lines," 7th International Conference on Electrical and Power Engineering, Iasi, 2012, pp. 628-631.

[11] S.S. Razavipour, M. Jahangiri, and H. Sadeghipoor, "Electrical Field around the Overhead Transmission Lines," World Acad. Sci. Eng. Technol., Vol. 6, No. 2, pp. 168-171, 2012.

[12] J.S. Santos, C.E.A. Henrique, R.M. Silva, and C.A.C. Tenorio, "A Matlab based software for measurement of transmission line fields," 2011 IEEE Power & Energy Society Innovative Smart Grid Technologies Conference, Anaheim, 2011, pp. 1-6.

[13] M. Milutinov, A. Juhas, and M. Prša, "Electromagnetic Field underneath Overhead High Voltage Power Line," 4th International Conference on Engineering Technologies, Novi Sad, 2009, pp. 1-5.

[14] S. Vujević, D. Lovrić, and T. Modrić, "2D Computation and Measurement of Electric and Magnetic Fields of Overhead Electric Power Lines," Joint 3rd International Workshop on Nonlinear Dynamics and Synchronization (INDS'11) & 16th International Symposium on Theoretical Electrical Engineering (ISTET'11), Klagenfurt, 2011, pp. 1-6.

[15] M. Kokoruš, S. Delić, A. Mujezinović, M. Muratović, and A. Čaršimamović, "Analysis of the possible solutions for the reduction of electric and magnetic fields near 400 kV overhead transmission lines," Environmental Impact II (WIT Transactions on Ecology and The Environment), pp. 225-236, WIT Press, Southampton, 2014.

[16] S.F. Braicu, L. Czumbil, D. Stet, and D.D. Micu, "Evaluation of the Electric and Magnetic Field near High Voltage Power Lines," 5th International Conference on Advancements of Medicine and Health Care through Technology, Cluj-Napoca, 2016, pp. 141-146.

[17] E. Lunca, B.C. Neagu, and S. Vornicu, "Finite Element Analysis of Electromagnetic Fields Emitted by Overhead High-Voltage Power Lines," in *Numerical Methods for Energy Applications*, Springer, Cham, 2021.

[18] IEEE, "IEEE Standard Procedures for the Measurement of Electric and Magnetic Fields from Video Display Terminals (VDTs) from 5 Hz to 400 kHz," in IEEE Std. 1140-1994, pp.1-32, 27 June 1994, doi: 10.1109/IEEESTD.1994.121446.

[19] "ICNIRP Guidelines for Limiting Exposure to Time-Varying Electric, Magnetic, and Electromagnetic Fields (up to 300 GHz)," Health Physics, Vol. 74, No. 4, pp. 494-522, 1998.

21st IMEKO TC4 International Symposium and
19th International Workshop on ADC Modelling and Testing
Understanding the World through Electrical and Electronic Measurement
Budapest, Hungary, September 7-9, 2016

Evaluation of EMF Exposure from Digital Terrestrial Television Transmitters

Eduard Lunca[1], Alexandru Salceanu[2], Silviu Ursache[2], Mirela-Adelaida Anghel[3]

[1]*Faculty of Electrical Engineering, 21 Prof. Dimitrie Mangeron Street, 700050 Iasi, Romania, elunca@tuiasi.ro, +40 232 278683/1246*
[2]*Faculty of Electrical Engineering, 21 Prof. Dimitrie Mangeron Street, 700050 Iasi, Romania, asalcean@tuiasi.ro, silviu_ursache@tuiasi.ro, +40 232 278683/1157*
[3]*Romanian Bureau of Legal Metrology, Bucharest, Vitan Barzesti Road nr.11, Romania, mirela.a.anghel@gmail.com, +40213320954*

***Abstract* – This study presents results of a preliminary survey of the RF electromagnetic fields (EMFs) originating from digital terrestrial television transmitters. In situ-measurements of DVB-T2 signals were conducted in the city of Iasi, Romania, and its rural vicinity, where a 180 meters tall guyed mast for FM-/TV-broadcasting is installed. The measured *E*-field levels were found to be well below the exposure limits recommended by the International Commission on Non-Ionizing Radiation Protection (ICNIRP) for the general public.**

***Keywords* – EMF exposure, DVB-T2 transmitter antennas, in-situ measurements**

I. INTRODUCTION

The transition from analogue to digital terrestrial television (DTT or DTTV) is a process in various stages of implementation around the world [1]. In the European Union (EU), DTT represents the most widespread platform for TV reception, reaching over 100 Million households – 250 million viewers [2].

DVB-T (*Digital Video Broadcasting – Terrestrial*) is the DVB European-based consortium standard for the broadcast transmission of digital terrestrial television. It transmits compressed digital audio, digital video and other data in an MPEG transport stream, using the coded orthogonal frequency-division multiplexing modulation (COFDM). DVB-T was first published in 1997 and first broadcast in 1998, in the UK [3].

Although Romania started DVB-T broadcasting in 2005, it was only experimental. In 2012, the Romanian authorities decided that DVB-T2 (*Digital Video Broadcasting – Second Generation Terrestrial*) will be the standard used for terrestrial broadcasts, as it allows a larger number of programs to be broadcast on the same multiplex (MUX). On 17 June 2015, the analogue terrestrial television was switched off, with the exception of the main public TV program (TVR1), which will continue to be broadcast strictly in the VHF band until the end of 2016 [4].

At the end of 2015, free-to-air DVB-T2 broadcasts on MUX1, provided by the state-owned Radiocom, were available for about 56% of the population [5]. In such a context, we initiated a measurement campaign of the RF electromagnetic fields originating from DVB-T2 transmitter antennas, first in the city of Iasi and its rural vicinity. To our knowledge, no study has tried to evaluate the in-situ DVB-T2 exposure in our country.

II. RELATED RESULTS IN THE LITERATURE

A number of studies concerning – at least partially – the RF exposure from DVB-T systems were published over the past decade, with the migration to DTT in the European countries.

In Germany, extensive exposure measurements were performed at more than 300 points in two DVB-T starting-areas, Munich and Nuremberg. At 200 locations in residential areas, measurements before and after the switchover were carried out to determine a possible change of exposure situation. Additional measurements along defined lines and inside buildings were also performed [6, 7].

In Belgium, The Netherlands and Sweden, measurements of DVB-T signals were carried out in the framework of a common survey of the RF electromagnetic fields from emerging wireless communication technologies. According to this study [8], which was published in 2012, the exposure ratios from DVB-T (if present) were the highest except GSM.

A study from 2013, [9], deals with the electromagnetic field exposure from a DVB-T transmitter in the urban environment of Zagreb. Measurements of electric field were performed at several key locations and compared to theoretical calculations of the present field.

There are also several studies and reports concerning the evaluation of the RF exposure from DVB-T, e.g. [10], but all of these show that the RF exposure levels are generally well below the exposure limits recommended by ICNIRP [11]. This is also true in our case.

III. MEASUREMENT METHOD

Like its predecessor, DVB-T2 uses the OFDM modulation scheme [12], which divides the available bandwidth into a large number of closely spaced subcarriers and transmits data in parallel streams. The signal bandwidth can be either 8 MHz (in the UHF band) or 7 MHz (in the VHF band). Currently, the DVB-T2 transmissions occur in the UHF band, relayed from a number of transmitters located at high sites around the country.

In order to measure such emissions, we adopted a frequency-selective method based on a SPECTRAN HF-60105 V4 spectrum analyzer (1 MHz – 9.4 GHz) in conjunction with a calibrated BicoLOG 20300 antenna (20 MHz – 3 GHz), both from Aaronia AG (Fig. 1). After extensive investigations, taking into account the characteristics of the DVB-T2 signals with respect to the performances of the spectrum analyzer, the following settings were established for assessing the DVB-T2 exposure: RMS (Root Mean Square) detector, resolution bandwidth *RBW* = 5 MHz, video bandwidth *VBW* = 50 MHz (FULL), sample time *SpTime* = 250 ms (sweep time *ST* about 750 ms, as reported by the MCS Spectrum Analyzer Software), frequency span of 20 MHz, with the center frequency (CF) of the spectrum analyzer equal to the CF of the DVB-T2 signal.

Fig. 1. Instrumentation used for the survey

At each selected location, MAX HOLD measurements were taken with the antenna oriented in three orthogonal directions, at a distance of 1.5 m above the ground or floor, for a sufficiently long time to allow the trace to stabilize. During the investigations, a minimum distance of 0.5 m was maintained between any object and the antenna [13, 14].

All readings indicated by the spectrum analyzer (power in units of dBm) were recorded and converted to *E*-field strength levels, in units of V/m, by taking into account the antenna factor and power losses in the connecting coaxial cable [15, 16]. Then, the total *E*-field at each location was calculated with the formula [17]:

$$E_{tot} = \sqrt{E_x^2 + E_y^2 + E_z^2}\,, \qquad (1)$$

where E_x, E_y and E_z represent the three orthogonal readings.

The specified accuracy of the HF-60105 V4 spectrum analyzer is ±1 dB (typically), but higher deviations are possible especially when approaching the so-called noise floor or the maximum sensitivity of the instrument [18].

IV. RESULTS AND DISCUSSION

DVB-T2 exposure measurements were performed at 80 locations: 62 – in different areas of the Iasi city, 18 – in the surrounding of the "Pietraria" transmitter, a 180 meters tall guyed mast for FM-/TV-broadcasting at Pietraria, a village near Iasi. Fig. 1 shows the position of the transmitter and considered measurements locations on the map. Most of the measurements were taken outdoor, in the period March 2016 – April 2016.

An overview of the VHF and UHF frequency bands at a measurement location is shown in Fig. 3. At the moment, only a DVB-T2 signal is present in the UHF band, on channel 25 (506 MHz CF). Other two multiplexes will be broadcast in the UHF band until the end of May 2017, so we expect an increase in total RF exposure associated with this technology.

Fig. 2. Indication of the measurement locations on the map (yellow marker: E < 0.1 V/m; black marker: E > 0.1 V/m)

The highest *E*-field level recorded during the survey was 0.382 V/m, which represents 1.24% of the exposure limit (30.93 V/m at the frequency of 506 MHz). It was measured in the proximity of the "Pietraria" transmitter, at a ground distance of about 150 m (location "1" on the map). The highest *E*-field level measured in the urban environment was 0.096 V/m (location "2" on the map), which accounts for 0.31% of the limit.

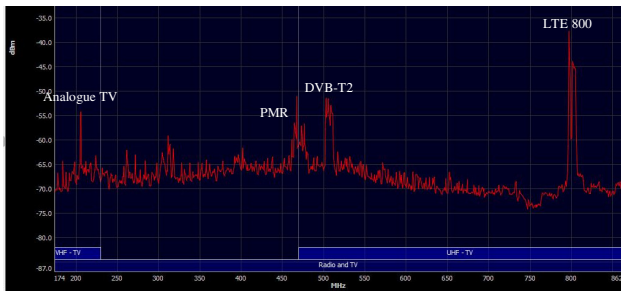

Fig. 3. Overview of the VHF and UHF frequency bands

Fig. 4.*a* illustrates the general distribution of the survey results in terms of *E*-field strength. The overwhelming majority of the results are below 0.1 V/m (0.32% of the field strength limit), whereas the average and median values are 0.072 V/m (0.23% of the limit) and 0.056 V/m (0.18% of the limit) respectively. In percentage terms, 61% of the recorded *E*-field levels are below 0.25% of the ICNIRP exposure limit, whereas 13% of the readings are in the range from 0.25% to 0.5% of the limit (Fig. 4.*b*).

At a first glance, the obtained results are comparable to those reported for DVB-T in the literature. For instance, in [7], the maximal exposure concerning the power density is 6.5 mW/m^2 (corresponding to 0.24% of the ICNIRP reference levels), whereas our maximum value is 0.39 mW/m^2 (corresponding to 0.015% of the ICNIRP limit, 2.53 W/m^2). In [8], the maximal and average exposure values reported for Analogue TV / DVB-T are 1.65 V/m and 0.09 V/m respectively. As we can see, these levels are somewhat higher than our results, but we measured only a single channel.

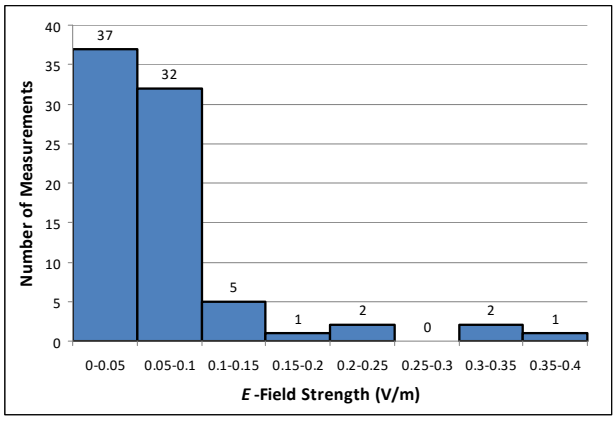

a)

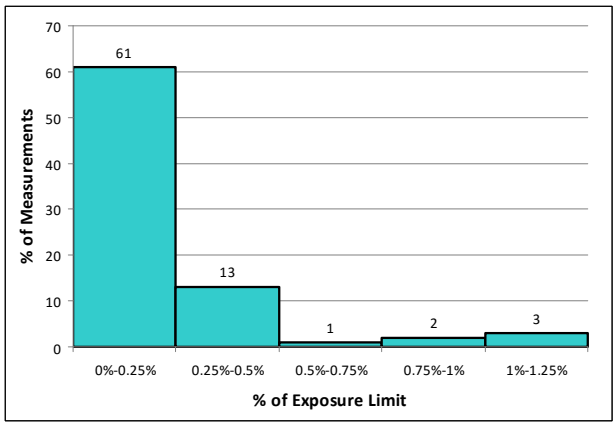

b)

Fig. 4. Distribution of the recorded data: a) number of measurements as a function of E-field strength; b) percent of measurements as percent of ICNIRP exposure limit

Regarding the main factors influencing the DVB-T2 exposure, this greatly depends on the distance from the transmitter and terrain irregularities. The buildings and other obstructing structures in the urban environment have also a strong influence on the DVB-T2 exposure, causing not only a significant reduction in the EMF levels, but also a very complex spatial distribution.

V. CONCLUSIONS AND FUTURE WORK

According to the measurements performed for this survey, the *E*-field levels from DVB-T2 transmitter antennas were found to be well bellow the exposure limits recommended in the ICNIRP guidelines. The highest *E*-field level was 0.382 V/m, which corresponds to only 1.24% of the exposure limit, whereas 74% of the measurements were below 0.5% of the limit.

Future research will be focused on the influence of different factors on the DVB-T2 exposure. For instance, one limitation of our study was that most of the measurements were taken outdoor, at the ground level, so further investigations might be necessary to characterize the indoor exposure, especially in tall buildings that are in the direct line-of-sight of the transmitter. Also, we expect an increase in the total DVB-T2 exposure with the release of MUX2 and MUX4, until the end of May 2017.

REFERENCES

[1] *Report ITU-R BT.2140-8, "Transition from analogue to digital terrestrial broadcasting"*, International Telecommunication Union – Radiocomunication Sector, 02/2015. https://www.itu.int/pub/R-REP-BT.2140-9-2015

[2] *"Radio Spectrum"*, European Broadcasting Union (EBU), November 2015. http://www3.ebu.ch/files/live/sites/ebu/files/Publications/Policy%20sheets/Radio%20Spectrum_EN.pdf

[3] Poole, I. "What is DVB-T?", Tutorial. http://www.radio-electronics.com/info/broadcast/digital-video-broadcasting/what-is-dvb-t-basics-tutorial.php

[4] *DVB-T2*, Article. https://en.wiki2.org/wiki/DVB-T2

[5] *DVB-T2 – Estimated working area*, December 2015, Radiocom. http://www.radiocom.ro/poze/dvbt2/Tranzitie%20DVB-T2_Decembrie.pdf

[6] Bornkessel, K., Schubert, M., Wuschek, M., Schmidt P. "Bestimmung der Exposition der Bevölkerung in der Umgebung von digitalen Rundfunk- und Fernsehsendern." Final report for the German Federal Office for Radiation Protection, 18 July 2006. http://www.bmub.bund.de/fileadmin/bmu-import/files/pdfs/allgemein/application/pdf/schriftenreihe_rs706.pdf

[7] Schubert, M., Bornkessel, C., Wuschek, M., Schmidt, P. "Exposure of the general public to digital broadcast transmitters compared to analogue ones." Radiation Protection Dosimetry. 124(1), pp. 53-57. 2007.
DOI: 10.1093/rpd/ncm337

[8] Joseph, W., Verloock, L., Goeminne, F., Vermeeren, G., Martens, L. "Assessment of RF exposures from emerging wireless communication technologies in different environments." Health Physics. 102(2), pp. 161-172. 2012.
DOI: 10.1097/HP.0b013e31822f8e39

[9] Juričev-Sudac, L., Malarić, K. "Exposure to electromagnetic field from DVB-T transmitter." Proceedings of the 21st International Conference on Software, Telecommunications and Computer Networks (SoftCOM). pp. 1-5. 2013. DOI: 10.1109/SoftCOM.2013.6671874

[10] Wuschek, M. "Bestimmung Elektromagnetische Immissionen durch Mobilfunksendeanlagen." Report on the performed field strength measurements for the Municipality Sünching, Project no. 12/027, 2012. http://www.erlangen.de/Portaldata/1/Resources/080_stadtverwaltung/dokumente/erlaeuterungen/31ImSch_I_Messbericht_Mobilfunk_2006_verschiedene_Messpunkte_CEG_Loehestrasse_usw.pdfs/allgemein/application/pdf/schriftenreihe_rs706.pdf

[11] ICNIRP. "Guidelines for limiting exposure to time-varying electric, magnetic and electromagnetic fields (up to 300 GHz)." Health Physics. 74(4), pp. 494-522. 1998.

[12] *Standard ETSI EN 302 755 V1.4.1, "Digital Video Broadcasting (DVB); Frame structure channel coding and modulation for a second generation digital terrestrial television broadcasting system (DVB-T2)"* (2015)

[13] Lunca, E., Damian, C., Salceanu, A. "EMF exposure measurements on 4G/LTE mobile communication networks." Proceedings of the 2014 International Conference and Exposition on Electrical and Power Engineering. pp. 545-548. 2014.

[14] Lunca, E., Ursache, S., Salceanu, A. "Assessment of RF Exposure Levels Generated by WiMAX Base Stations." Environmental Engineering and Management Journal. In press.

[15] Lunca, E., David, V., Salceanu, A., Cretescu, I. "Assessing the human exposure due to wireless local area networks in office environments." Environmental Engineering and Management Journal. 11(2), pp. 385-391. 2012

[16] Lunca, E., Salceanu, A., Ursache, S. "Automated Measurement and Monitoring of the Electromagnetic Fields from GSM Systems." Journal of Clean Energy Technologies. 1(3), pp. 174-177. 2013.
DOI: 10.7763/JOCET.2013.V1.40

[17] Commision for Communications Regulations (CCR). "Programme of Measurement of Non-Ionising Radiation Emissions. Methodology for the Conduct of Surveys to Measure Non-Ionizing Electromagnetic Radiation from Transmitter Sites", Document No. 08/51R2, 2014. http://www.comreg.ie/_fileupload/publications/ComReg0851.pdf

[18] Aaronia AG, *Manual Spectran V4*, 2013. http://www.aaronia.com/Datasheets/Documents/SPECTRAN-HF_V4_EN.pdf

An Overview of RF-EMF Monitoring Systems and Associated Monitoring Data

Eduard Lunca, Alexandru Salceanu
Department of Electrical Measurements and Materials
Faculty of Electrical Engineering
Technical University of Iasi
Iasi, Romania
{elunca, asalcean}@tuiasi.ro

Abstract—**There is a high demand for monitoring the electromagnetic fields (EMFs) generated by communication systems and other radiofrequency (RF) technologies, in order to assess compliance with existing legislation and prescribed reference levels. The broadband EMF monitoring systems unquestionably represent one of the major innovations in this area, continuously measuring the total EMF from all surrounding sources and performing a real-time dissemination of the assessment results to the public. In this study, we analyze exposure data from 8 broadband EMF monitoring systems operating in 7 countries, which totalize over 400 active stations. The results of the analysis suggest that the exposure levels to RF-EMFs are quite similar between countries, and generally well below the reference levels defined by the national legislations.**

Keywords—radiofrequency electromagnetic fields; monitoring systems; monitoring data; exposure limits

I. INTRODUCTION

The exposure to RF-EMFs is a cause of concern for many people [1-6]. One solution to this problem is to control the electromagnetic emission levels by continuously taking measurements and to properly communicate the results to the general public. For years, in various countries around the world, broadband EMF monitoring systems have been used with satisfactory results, increasing citizens' confidence in governments and reducing their fear and ignorance regarding the electromagnetic radiation [7].

The EMF monitoring systems are operated either by regulatory agencies or independent entities, which make the results available on the Internet. Basically, such a system consists of a number of remote measurement stations that are managed, via the mobile network, from a data control center (DCC). Depending on the system, there may be one ore more DCCs, deployed on a regional basis. The EMF data collected from the monitoring stations is stored in a database in DCC, usually allowing end-users to look up and display measured EMF values at any location over the desired time period, in a simple chart format. The exposure levels are given either in terms of electric field strength, E(V/m), or power density, S(W/m^2), together with the considered reference limits [8-12].

The Romanian EMF monitoring system, which is operated by the National Authority for Management and Regulation in Communications (ANCOM), has been installed in the last part of 2015 and comprises 50 broadband monitoring stations located in urban areas, in Bucharest and other 35 cities, in the vicinity of schools, hospitals, public institutions, crowded areas (e.g., marketplaces) and public places that are close to multiple EMF sources. Each station (Fig. 1.*a*) uses a three-axis isotropic probe for measuring the electric field strength in four frequency bands: 100 kHz – 7 GHz (broadband), 925 MHz – 960 MHz (GSM 900), 1805 MHz – 1880 MHz (GSM 1800) and 2110 MHz – 2170 MHz (UMTS 2100) [13]. End-users can visualize the stations' location on Google Maps, select a specific station and see most recent measurements results or results further in the past through the ACTA EMF Observatory [14], a powerful web application compatible with Narda EMF stations. As presented in Fig. 1.*b*, the displayed results are compared to the limit values for the general public exposure to EMFs instituted by the Romanian state (the Decree no. 1193/2006 issued by the Ministry of Public Health).

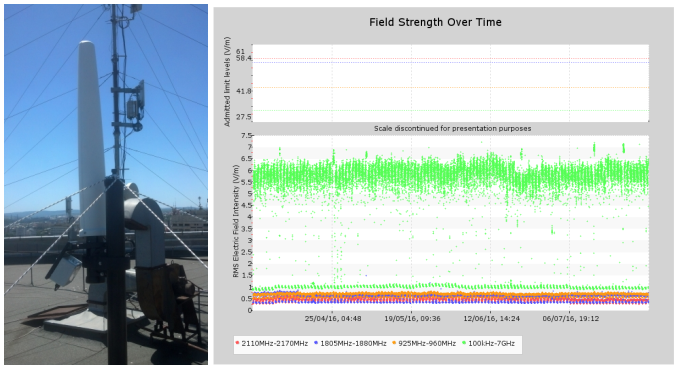

(a) (b)

Fig. 1. Quadband EMF monitoring station, model Narda AMB-8059, operating in the city of Iasi: (a) installation conditions; (b) example of EMF monitoring data – electric field strength over 4 months [Source: http://www.monitor-emf.ro, ANCOM].

Since several EMF monitoring systems are currently in use, the aim of our study is twofold. First, it aims to compare the EMF monitoring data between different countries. Second, it offers a preliminary insight into the EMF exposure levels recorded by the Romanian EMF monitoring system, from its deployment at the end of the first quarter of 2016.

978-1-5090-6129-7/16/$31.00 ©2016 European Union

II. Materials and Methods

At the moment, a limited number of broadband EMF monitoring systems are operational. In this study, we analyzed exposure data provided by 8 EMF monitoring systems from 7 countries (Romania, Spain – 2, Turkey, Switzerland, Colombia, Uruguay and El Salvador), which totalized 417 measurement stations. The largest system is the one controlled by the Government of Catalonia, Spain, with over 300 active monitoring devices installed in 185 municipalities, whereas the smallest one is the system operated by the General Superintendence of Electricity and Telecommunications (SIGET), El Salvador, with a single active station.

For each station, the exposure data consisted of the maximum and average *E*-field strength over the last week, the last month and from the beginning of the year. The end date has been set to August 11, 2016. Two systems, in Romania and Switzerland, do not provide the average value over the selected time period, but only the maximum one, which has been graphically determined. The Colombian EMF network displays the exposure data in terms of percentage of exposure limit, so the *E*-field strength has been calculated by taking into account the specified limit level.

All *E*-field data sets have been summarized with the highest, lowest and, where appropriate, median value, and then compared to the reference levels adopted by each country, which in turn are those established by the International Commission on Non-Ionizing Radiation Protection (ICNIRP), in 1998 [15]. Furthermore, to get a general distribution of the maximum and average *E*-field values from the beginning of the year, the total number of results has been plotted as a function of *E*-field strength. Finally, to obtain a preliminary insight into the EMF exposure levels recorded in our country, the maximum *E*-field strength for each of 50 stations has been plotted for all the three time periods considered above.

III. Results and Discussions

A synthetic overview of all EMF monitoring data is given in Table I. E_{max} and E_{avg} represent the maximum and average values of the electric field strength over the considered time periods, whereas E_{lim} represents the specified reference level.

TABLE I. Synthetic EMF Monitoring Data across Different Countries

Country	Institution	No. of active stations	Frequency range	Value of interest	E_{max}(V/m)			E_{avg}(V/m)			E_{lim} (V/m)
					From Jan. 1	*Last month*	*Last week*	*From Jan. 1*	*Last month*	*Last week*	
Romania	National Authority for Management and Regulation in Communications (ANCOM) [13]	50	100 kHz – 7 GHz	Highest	18.10	13.80	13.00	–	–	–	27.5
				Median	2.19	1.93	1.67	–	–	–	
				Lowest	0.42	0.32	0.29	–	–	–	
Turkey	Information and Communication Technologies Authority (ICTA) [16]	14	100 kHz – 3 GHz	Highest	9.98	9.83	9.83	6.84	6.49	6.45	41.25
				Median	3.50	2.23	2.21	1.88	1.68	1.71	
				Lowest	1.15	1.15	0.86	0.65	0.65	0.67	
Spain	Government of Catalonia [17]	275	900 MHz / 1800 MHz / 2100 MHz	Highest	35.94	35.86	16.20	19.35	21.95	11.81	41
				Median	2.14	1.98	1.73	1.29	1.27	1.27	
				Lowest	0.17	0.11	0.09	0.05	0.06	0.06	
		41	100 kHz – 8 GHz	Highest	24.93	20.67	20.67	20.37	19.04	19.25	28
				Median	3.39	3.07	2.95	2.29	2.14	2.14	
				Lowest	0.44	0.29	0.29	0.15	0.17	0.17	
	City Hall of Vitoria-Gasteiz [18]	5	900 MHz / 1800 MHz / 2100 MHz	Highest	2.03	1.73	1.69	1.41	1.36	1.36	41
				Median	1.64	1.57	1.24	1.03	1.02	1.02	
				Lowest	1.23	1.13	1.12	0.95	0.81	0.80	
Switzerland	Zentralschweizer Umweltdirektionen (ZUDK) [19]	4	100 kHz – 3 GHz	Highest	2.60	2.00	2.00	–	–	–	
				Median	1.06	1.03	0.96	–	–	–	
				Lowest	0.46	0.40	0.38	–	–	–	
Colombia	National Spectrum Agency (ANE) [20]	24	900 MHz / 1800 MHz / 2100 MHz	Highest	13.59	11.08	11.08	7.73	8.14	8.28	41
				Median	1.52	1.37	1.35	1.06	1.05	1.04	
				Lowest	0.82	0.40	0.34	0.15	0.07	0.07	
Uruguay	Communication Services Regulatory Agency (URSEC) [21]	3	100 kHz – 8 GHz	Highest	3.78	3.71	3.00	2.17	2.61	2.61	28
				Median	2.76	2.76	2.76	1.86	1.89	1.97	
				Lowest	2.40	2.40	2.40	1.61	1.85	1.96	
El Salvador	General Superintendence of Electricity and Telecommunications (SIGET) [22]	1	100 kHz – 8 GHz	–	4.96	4.43	3.99	3.30	3.14	3.00	28

None of the 417 monitoring stations have registered *E*-field levels higher than E_{lim}. The highest (global) maximum *E*-field level from the beginning of the year, 35.94 V/m (87.66% of the prescribed exposure limit, 41 V/m), has been recorded by a monitoring station covering the "current mobile phone frequency bands" (900 MHz, 1800 MHz and 2100 MHz), in Alt Camp, Catalonia (Spain); the average *E*-field level for the same station is three times lower, 11.94 V/m (29.12% of the exposure limit). Note that a maximum *E*-field level more than two times higher than the ICNIRP limit has been indicated by a monitoring station in Istanbul, Turkey, but the displayed *E*-field data have encountered errors. Consequently, they have been excluded from analysis.

The highest average *E*-field level from the beginning of the year, 20.37 V/m (72.75% of the prescribed exposure limit, 28 V/m), has been recorded by a monitoring station covering the frequency range 100 kHz – 8 GHz, also in Catalonia, but in Segrià. The maximum *E*-field strength indicated by this station is closer to the average value, namely 24.93 V/m (89.04% of the mentioned exposure limit).

The medians for both E_{max} and E_{avg} are quite low compared to the highest values of these quantities, not exceeding 3.5 V/m and 2.3 V/m respectively (from the beginning of the year). Except a few stations, no significant differences in these two quantities, and especially in E_{avg}, have been observed over the considered time periods.

Fig. 2.*a* illustrates the general distribution of the maximum *E*-field levels for a number of 414 stations. A percentage of 81.4% (N = 337) of them recorded values below 5 V/m, whereas 55.07% (N = 228) of them recorded values below 2.5 V/m. As for the average *E*-field levels, from a total of 360 monitoring stations providing such data, 94.44% (N = 340) of them recorded values below 5 V/m, whereas 79.17% (N = 285) of them recorded values below 2.5 V/m (Fig. 2.*b*). Once again, this simple statistics corresponds to the time period from Jan. 1, 2016 to Aug. 11, 2016.

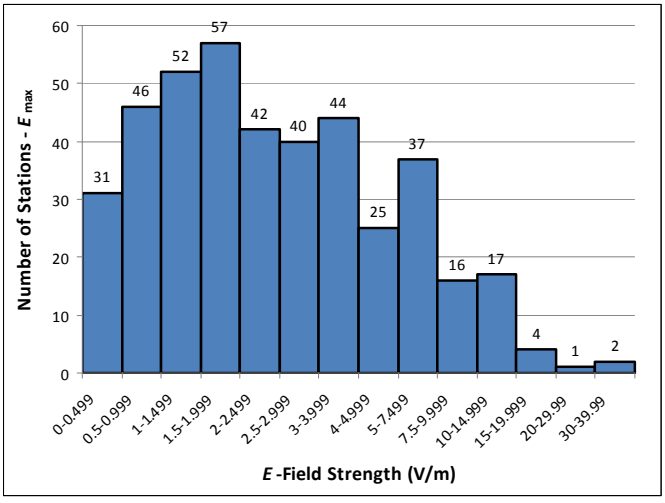

(a)

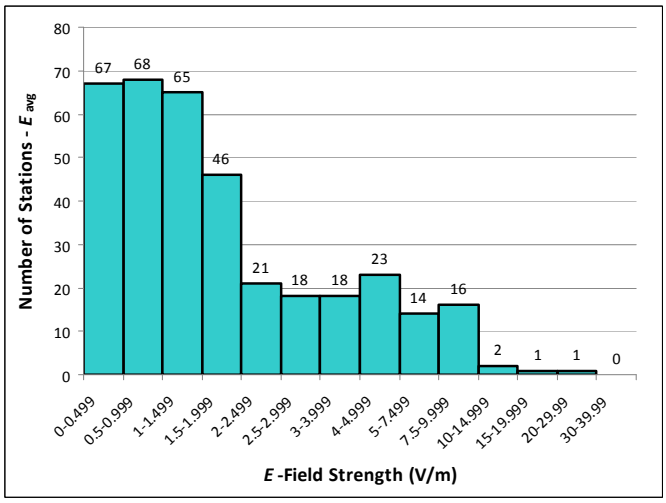

(b)

Fig. 2. Distribution of the EMF monitoring data from Jan. 1, 2016 to Aug. 11, 2016: (a) maximum *E*-field levels, E_{max}; (b) average *E*-field levels, E_{avg}.

Fig. 3 presents the maximum *E*-field strengths recorded by the 50 stations installed in our country, over the last week, the last month and the entire operation period, over 4 months. The overwhelming majority of the stations (N = 42) recorded maximum *E*-field strengths below 5 V/m, whereas 58% (N = 29) of them recorded values below 2.5 V/m. The highest *E*-field level, 18.1 V/m (65.82% of the specified exposure limit, 27.5 V/m), has been recorded by a monitoring station installed on a rooftop with different types of antennas, in the capital Bucharest. Unfortunately, the system operated by ANCOM does not provide information about the average *E*-field level over the selected time period, but in this case we estimate an average value of about 14 V/m (50.91% of the admitted limit).

IV. Conclusions and Future Work

According to the accessed monitoring data, the exposure levels to radiofrequency electromagnetic fields are quite similar between countries, and generally well below the limits defined by the ICNIRP guidelines. The highest (global) maximum *E*-field level from the beginning of the year is 35.94 V/m, which corresponds to 87.66% of the prescribed limit, 41 V/m, whereas the highest average *E*-field level for the same period is 20.37 V/m, which accounts for 72.75% of the prescribed limit, 28 V/m. Both values have been registered in Spain, Catalonia, which has the largest EMF monitoring network in the world, with over 300 active stations.

Future research will be focused on the analysis of EMF monitoring data from more stations (some systems could not be accessed due to various reasons), as well as on extending the evaluation period, in order to better assess the temporal evolution of the EMF exposure. Special attention will also be paid to the analysis of EMF data provided by the system installed in our country, during its first year of operation.

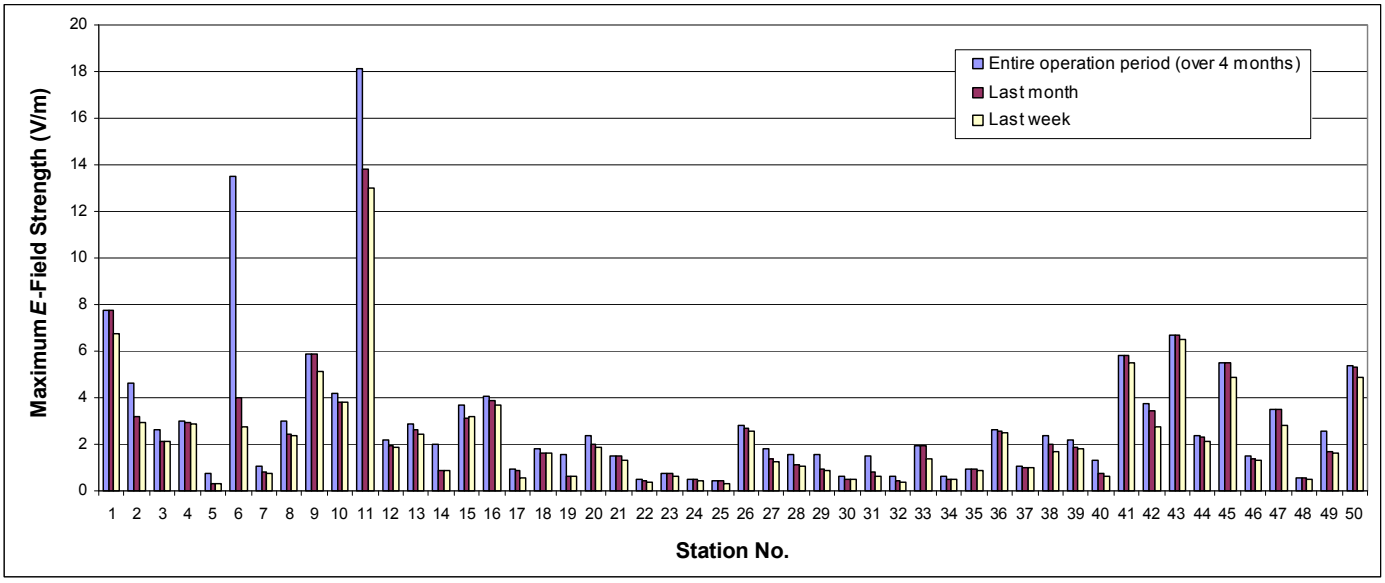

Fig. 3. Maximum *E*-field strengths recorded in our country.

REFERENCES

[1] G. Dürrenberger, J. Fröhlich, M. Röösli, and M-O Mattsson, "EMF Monitoring – Concepts, Activities, Gaps and Options", International Journal of Environmental Research and Public Health, Vol. 11, No. 9, pp. 9460-9479, 2014.

[2] E. Lunca, S. Ursache, and A. Salceanu, "Assessment of RF Exposure Levels Generated by WiMAX Base Stations", Environmental Engineering and Management Journal, in press.

[3] E. Lunca, A. Salceanu, and S. Ursache, "Evaluation of EMF Exposure from Digital Terrestrial Television Transmitters", 21st IMEKO TC-4 International Symposium on Understanding the World through Electrical and Electronic Measurement, Budapest, 2016.

[4] E. Lunca, C. Damian, and A. Salceanu, "EMF Exposure Measurements on 4G/LTE Mobile Communication Networks", 8th International Conference and Exposition on Electrical and Power Engineering (EPE 2014), Iasi, 2014, pp. 545-548.

[5] E. Lunca, A. Salceanu, and S. Ursache, "Automated Measurement and Monitoring of the Electromagnetic Fields from GSM Systems", Journal of Clean Energy Technologies, Vol. 1, No. 3, pp. 174-177, 2013.

[6] E. Lunca, V. David, A. Salceanu, and I. Cretescu, "Assessing the Human Exposure due to Wireless Local Area Networks in Office Environments", Environmental Engineering and Management Journal, Vol. 11, No. 2, pp. 385-391, 2012.

[7] ITU-T, "Monitoring of electromagnetic field levels", Recommendation ITU-T K.83 (2011) – Amendment 1, 2014, https://www.itu.int/rec/T-REC-K.83-201407-I!Amd1/en.

[8] N. Djuric, D. Kljajic, K. Kasas-Lazetic, and V. Bajovic, "The SEMONT continuous monitoring of daily EMF exposure in an open area environment", Environmental Monitoring and Assessment, Vol. 187, No. 4, pp. 1-17, 2015.

[9] D.S. Šuka, M.I. Simić, and P.V. Pejović, "Aspects of remote monitoring and recording system of non-ionizing electromagnetic radiation", 38th International Convention on Information and Communication Technology, Electronics and Microelectronics, Opatija, 2015, pp. 536-540.

[10] I. Popescu and P. Constantinou, "Review of EMR Monitoring Systems Developed by the Mobile Radiocommunications Laboratory, National Technical University of Athens", Serbian Journal of Electrical Engineering, Vol. 11, No. 3, pp. 435-455, 2014.

[11] F. Troisi, M. Boumis, and P. Grazioso, "The Italian National Electromagnetic Field Monitoring Network", Annals of Telecommunications, Vol. 63, No. 1, pp. 97-108, 2008.

[12] A. Gotsis, N. Papanikolaou, D. Komnakos, A. Yalofas, and P. Constantinou, "Non-ionizing Electromagnetic Radiation Monitoring in Greece", Annals of Telecommunications, Vol. 63, No. 1, pp. 109-123, 2008.

[13] ANCOM, *Monitor EMF*, http://www.monitor-emf.ro/index.php/en/.

[14] ACTA, "EMF Observatory", Datasheet, http://www.acta.com.gr/images/Datasheets/ACTA%20EMF%20Observatory%20Datasheet.pdf.

[15] ICNIRP, "Guidelines for limiting exposure to time-varying electric, magnetic and electromagnetic fields (up to 300 GHz)", Health Physics, Vol. 74, No. 4, pp. 494-522, 1998.

[16] ICTA, *Elektromanyetik alan Sürekli İzleme Sistemi* (*ESIS*), http://ema-olcum.btk.gov.tr/.

[17] Generalitat de Catalunya, *Governança Radioelèctrica*, http://radioelectricgovernance.gencat.cat.

[18] Ayuntamiento de Vitoria-Gasteiz, *Sistema de Monitorización de Radiofrecuencia* (*SMRF*), http://smrf.wavecontrol.com/gmap/vitoria.html.

[19] ZUDK, *Aktuelle Messstationen und daten ab 2010*, http://www.niszudk.emconsult.net/index2.php.

[20] ANE, *Sistema de Monitorización de Radiofrecuencia* (*SMRF*), http://smrni.ane.gov.co/AppPHP/indexGMap.php?idioma=es_ES.

[21] URSEC, *Sistema de Monitorización de Radiofrecuencia* (*SMRF*), http://200.40.205.85:8085/gmap/index.html.

[22] SIGET, *Sistema de Monitorización de Radiofrecuencia* (*SMRF*), http://rni.siget.gob.sv/gmap/ElSalvador.html.

EMF Exposure Measurements on 4G/LTE Mobile Communication Networks

Eduard Lunca, Catalin Damian, Alexandru Salceanu
Department of Electrical Measurements and Materials
Faculty of Electrical Engineering
"Gheorghe Asachi" Technical University of Iasi, Romania
{elunca, cdamian, asalcean}@tuiasi.ro

Abstract - **This study reports preliminary results of a survey of the RF electromagnetic fields originating from Long-Term Evolution (LTE) base station antennas. Both indoor and outdoor measurements of LTE1800 and LTE2600 signals were conducted in a large urban area, around a number of LTE transmitters. The measured E-field exposure levels, extrapolated for maximum traffic load, were found to be well below the exposure limits recommended by the International Commission on Non-Ionizing Radiation Protection (ICNIRP) for the general public. The results are in line with those of a few studies carried out recently in European countries.**

Keywords - electromagnetic field; LTE base stations; indoor and outdoor measurements; frequency-selective method

I. INTRODUCTION

Long-Term Evolution, or LTE, commonly marketed as 4G/LTE, is a new wireless communication standard of high-speed data for mobile devices, developed by the 3rd Generation Partnership Project (3GPP). It is an upgrade to the UMTS/WCDMA (3G) communication systems, featuring an enhanced radio interface and all-IP networking technology. LTE is currently adopted by more and more commercial operators around the world, being expected to become the first truly global standard for mobile phones.

Since LTE is a relatively new technology, the scientific literature related to the assessment of the RF electromagnetic fields from LTE systems is still limited. A few systematic studies were conducted starting with 2010, when the RF exposure from the world's first commercial LTE2600 network in Stockholm, Sweden, was determined at 30 randomly selected locations by Joseph et al. [1]. In [2], Joseph et al. also investigated the RF exposure from a trial network consisting of 7 LTE2600 base stations, at 40 locations in an urban environment of Reading, UK, whereas, in [3], Bornkessel and Schubert discuss results of a comprehensive measurement campaign conducted around 7 LTE800 and LTE2600 base stations, at 77 locations, in 5 German cities. A different approach was adopted by Colombi et al., in [4], who determined downlink output power distributions for more than 5000 base stations in a 4G/LTE network by extracting data using the operations support system (OSS) of the network, the results being then verified with in-situ power density measurements for one LTE cell in Stockholm [6]. All these studies revealed that the emissions caused by LTE are well below the ICNIRP reference levels [5], which were adopted by the majority of EU member states.

In Romania, the first 4G/LTE network was launched in November 2012. Other two networks became operational in December 2012 and April 2013 respectively, while another two networks are planned for 2014 [6]. In such a context, considering the current coverage of LTE in all major Romanian county seats is nearly 100%, we decided to conduct a survey of the RF exposure levels originating from LTE base stations installed in the city of Iasi. To our knowledge, until now, no study has addressed the LTE exposure in our country.

II. LTE SIGNAL STRUCTURE VS. EMISSIONS MEASUREMENT

The downlink physical layer of LTE is based on OFDMA, a multi-carrier scheme that allocates radio resources to multiple users. OFDMA takes advantage of the well-known Orthogonal Frequency Division Multiplexing (OFDM) modulation technique, which breaks the available bandwidth into many narrower subcarriers and transmits the data in parallel streams. For LTE, the basic subcarrier spacing is $\Delta f = 15$ kHz, but the total number of available subcarriers will depend on the overall transmission bandwidth of the system [7, 8].

In the time domain, the LTE transmissions are organized into radio frames of 10 ms length. Such a frame is divided into ten subframes, each being 1 ms long. A subframe is further divided into two slots, each of 0.5 ms duration. Finally, each slot consists of either 7 or 6 ODFM symbols, depending on whether a normal or an extended cyclic prefix (CP) is used. The OFDM symbol length can vary from 71.4 μs (normal CP) to 88.3 μs (extended CP).

A Resource Element is the smallest defined time-frequency unit for the LTE downlink transmission and represents one symbol (over time) by one subcarrier (in frequency). Resource Elements are grouped into Resource Blocks consisting of 12 consecutive 15 kHz subcarriers (totaling 180 kHz) in the frequency domain and one slot (i.e. 7 symbols for normal CP and 6 symbols for extended CP) in the time domain. The relationship between a slot, symbols and Resource Blocks is illustrated in Fig. 1.

978-1-4799-5849-8/14/$31.00 ©2014 IEEE

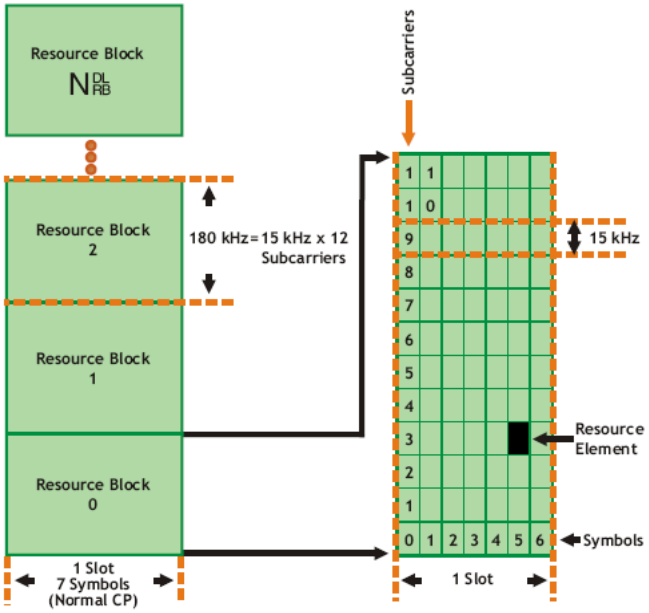

Figure 1. The relationship between a slot, symbols and Resource Blocks. [Source: LTE Resource Guide – Anritsu]

A Resource Block is the smallest unit that can be scheduled in the frequency domain. The transmission bandwidth is the number of active Resource Blocks in a transmission. As the bandwidth increases, the number of Resource Blocks also increases. The transmission bandwidth configuration, BW_{config}, is the maximum number of Resource Blocks for a particular channel bandwidth, $BW_{channel}$. The maximum occupied bandwidth is the number of Resource Blocks, N_{RB}, multiplied by 180 kHz. The relationship between LTE channel bandwidth, transmission bandwidth configuration and maximum occupied bandwidth is illustrated in Table I.

TABLE I. THE RELATIONSHIP BETWEEN LTE CHANNEL BANDWIDTH, TRANSMISSION BANDWIDTH CONFIGURATION AND MAXIMUM OCCUPIED BANDWIDTH

Channel bandwidth (MHz)	Maximum number of Resource Blocks / Transmission bandwidth configuration	Maximum occupied bandwidth (MHz)
1.4	6	1.08
3	15	2.7
5	25	4.5
10	50	9.0
15	75	13.5
20	100	18.0

Any LTE frame carries physical channels and physical signals. The channels carry information received from higher layers, such as data and system information, while the signals relate to physical layer functions, such as synchronization. The frame structure is the same for the uplink and downlink, but the physical signals and physical channels are different. Fig. 2, which represents a diagram of a downlink frame using FDD (Frequency Division Duplexing) and normal CP, shows the relative location of the various signals and channels. In LTE systems using TDD (Time Division Duplexing) or extended CP, the frames would be slightly different.

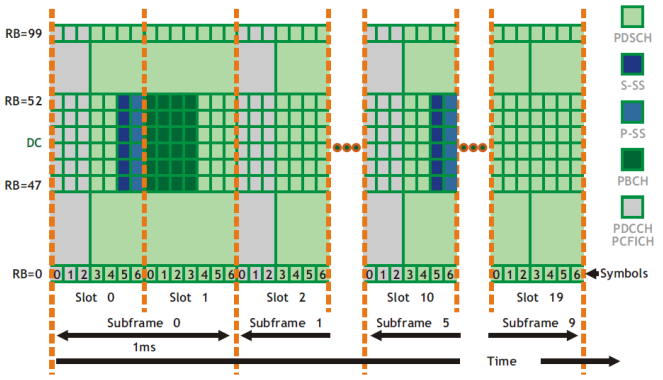

Figure 2. LTE downlink channels and signals. [Source: LTE Resource Guide – Anritsu]

The P-SS (Primary Synchronization Signal), S-SS (Secondary Synchronization Signal), PBCH (Physical Broadcast Channel) and RS (Reference Signal, not shown in Fig. 2) are of particular interest in the context of emissions measurement, because they are always transmitted (at a defined power level) in the downlink, regardless of whether data traffic is present or whether user devices are connected. Therefore, they are adequate for measurement and consequent extrapolation to the emission level resulting from the downlink under maximum data traffic [8].

III. MEASUREMENT METHOD

In this study, we adopted a frequency-selective technique focused on the P-SS and S-SS signals, which are transmitted in one OFDM symbol each, twice per frame, on 62 subcarriers around the central (DC) subcarrier. The measurement of these signals requires a spectrum analyzer with a resolution bandwidth of at least 0.93 MHz (a standard resolution bandwidth is 1 MHz), a RMS detector (due to the high crest factor) and a Max Hold function. In addition, because of the signal's timing structure, the sweep time of the spectrum analyzer must be chosen so that the measuring time per pixel does not exceed 70 μs (the minimum length of one OFDM symbol is 71.4 μs). However, rather than measuring in the frequency domain, measurements will be performed in the time domain (i.e. "Zero Span" mode). Detailed motivations for these settings are given in [8-10].

Measurements were carried out with an E4407B spectrum analyzer (9 kHz – 26.5 GHz), from Agilent Technologies, in conjunction with a HyperLOG 60100 log-periodic antenna (680 MHz – 10 GHz), from Aaronia. At each selected location, after setting the spectrum analyzer on the center frequency of the LTE signal to be measured, the worst-case exposure was determined by using the sweeping method, which involved slowly moving the hand-held measuring antenna (while varying the polarization and tilt) trough the space volume of an upright cylinder of 1 m diameter [11], up to about 2 m above

the ground or floor, until a maximum signal level was observed. During the investigations, a distance of at least 0.5 m was maintained between walls, floor, ceiling, furniture and metallic objects, and the antenna.

The entire measurement approach is summarized in Table II. Note that, in order to extrapolate for maximum traffic load (to extrapolate from the field level corresponding to the P-SS and S-SS signals measured across 1 MHz to the theoretical field level in the case when all the subcarriers across the full signal bandwidth are transmitted and carrying data), the full bandwidth of the LTE signal should be checked in the frequency domain, with respect to the values given in Table I. The maximum possible field level, E_{max}, is then calculated by applying a correction factor, K_{RBW}, which compensates for the limited resolution bandwidth of the spectrum analyzer with respect to the full signal bandwidth. The correction factor is to be derived as follows [8]:

$$K_{RBW} = \sqrt{B_{signal} / B_N} \ , \qquad (1)$$

where B_{signal} is the measured signal bandwidth and B_N is the noise bandwidth of the analyzer's filter. In the case of a Gaussian filter, $B_N \approx 1.1 B_{3dB}$, with $B_{3dB} = RBW$.

TABLE II. MEASUREMENT APPROACH USED FOR SURVEY

Equipment	E4407B spectrum analyzer and calibrated HyperLOG 60100 antenna
Measurement mode	Time domain ("Zero Span" mode)
Trace mode	Max Hold
Resolution bandwidth	1 MHz
Video bandwidth	3 MHz
Detector	RMS
Sweep time	401 (pixels) x 70 μs = 28 ms
Duration of each measurement	Until trace stabilizes
Extrapolation for maximum traffic load	Measure the LTE full signal bandwidth in the frequency domain and determine a correction factor. Calculate the field strength level for maximum traffic by applying the correction factor, $E_{max} = E_{measured}$ x K_{RBW} (V/m).

A frequency domain representation of a LTE downlink signal centered on 1815 MHz, with a signal bandwidth of 18 MHz, is shown in Fig. 3, a. Its correspondent time domain ("Zero Span") representation is shown in Fig. 3, b, the highest level indicated by marker being 0.167 V/m. By applying the extrapolation factor calculated with Equation (1), $K_{RBW} = 4.05$, a maximum value of 0.676 V/m is obtained.

IV. RESULTS

A total of 111 measurements were conducted at 38 locations (10 - indoor, 28 - outdoor), starting from about 20 m away from the closest LTE base station. The individual LTE signals measured at each site were adjusted to maximum theoretical levels and compared to the ICNIRP reference limits for the general public, as presented in Table III.

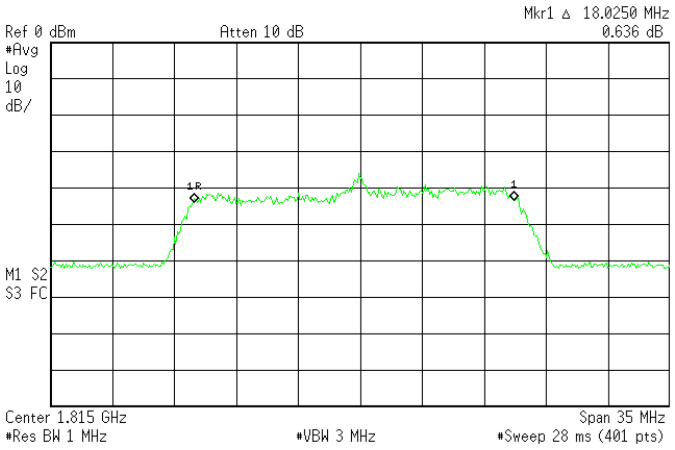

a)

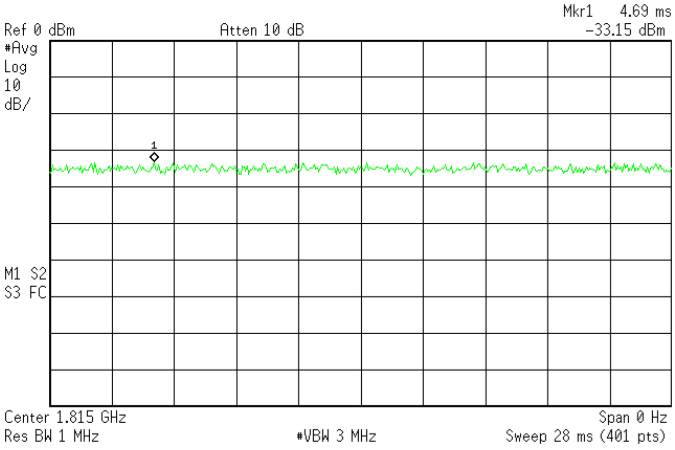

b)

Figure 3. LTE downlink signal: a) frequency domain measurement; b) time domain measurement

The highest E-field level recorded during the entire survey was 3.467 V/m, at the frequency of 2640 MHz. This value, which accounts for 5.5% of the exposure limit, was measured in front of an LTE antenna mounted on the wall of an 8-floor building, at a distance of 43.5 m from the building. The highest detected indoor level was 2.272 V/m, also at the frequency of 2640 MHz. This value, which accounts for 3.61% of the exposure limit, was measured in a classroom located at the 4th floor of a university building, in front of an LTE transmitter installed on the roof of a tower block in the neighborhood (about 105 m ground distance).

TABLE III. EXAMPLE OF MEASUREMENT RESULTS FOR LTE EXPOSURE

Center frequency (MHz)	$E_{measured}$ (V/m)	Extrap. factor	E_{max} (V/m)	ICNIRP limit (V/m)
1815	0.1671	4.05	0.6760	58.6
1865	0.0179	4.05	0.0726	59.4
2640	0.0133	4.05	0.0538	61.0

The lowest E-field level recorded during the survey was 0.008 V/m, at the frequency of 1865 MHz. This value, which represents only 0.01% of the exposure limit, was measured at two adjacent outdoor locations, being contributed by a distant LTE transmitter, with no visual contact.

An overview of all extrapolated LTE field levels is given in Fig. 4, a and b. The median corresponding to these individual readings is 0.2001 V/m, which agrees perfectly with the median reported in [3]. The maximum extrapolated E-field level reported in [3] was found to be 7.49 V/m (12.27% of the ICNIRP exposure limit), which is more than 2 times higher than our maximum level. In [2], the maximum extrapolated value for LTE exposure was found to be 1.9 V/m.

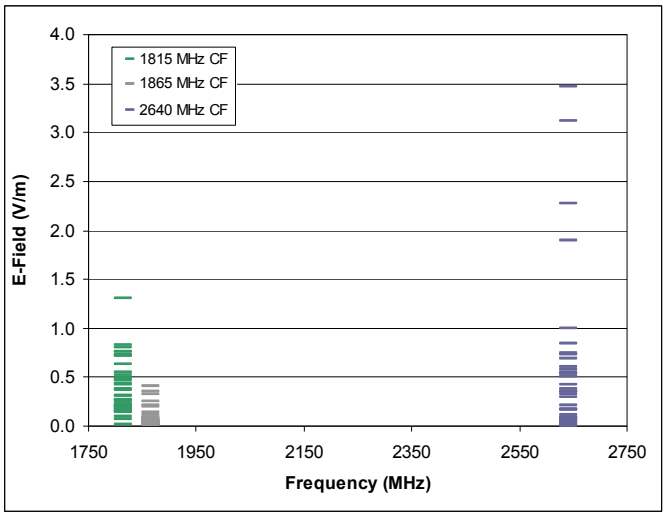

a)

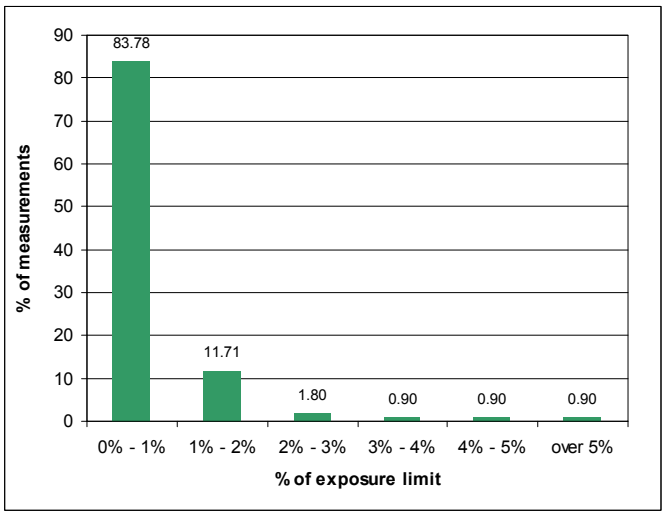

b)

Figure 4. Overview of the recorded data: a) maximum possible LTE exposure levels within specific sub-bands; b) number of measurements as percent of ICNIRP exposure limit

Statistically speaking, 83.8% of the recorded E-field values are below 1% of the ICNIRP exposure limit, whereas 11.7% of the individual readings fall between 1% and 2% of the limit. In terms of power density, 93.7% of the individual readings are below 0.02% of the ICNIRP reference level, which for LTE1800 and LTE2600 varies from 9 W/m^2 to 10 W/m^2. However, we should keep in mind that the total LTE exposure at each considered location is a summation of the LTE signals from different sub-bands.

V. Conclusions

Even if projected to a theoretical maximum, the exposure levels from LTE1800 and LTE2600 base station antennas were found to be well bellow the exposure limits recommended in the ICNIRP guidelines. According to the measurements performed for this preliminary survey, the maximal extrapolated E-field values varied from 0.008 V/m to about 3.5 V/m, which is less than 5.5% of the exposure limit. Future research will be focused on investigations at more locations, as well as on the influence of different factors on LTE exposure.

References

[1] W. Joseph, L. Verloock, F. Goeminne, G. Vermeeren, L. Martens, "Assessment of general public exposure to LTE and RF sources present in an urban environment", *Bioelectromagnetics*, Vol. 31, No. 7, pp. 576-579, 2010.

[2] W. Joseph, L. Verloock, F. Goeminne, G. Vermeeren, L. Martens, "In Situ LTE Exposure of the General Public: Characterization and Extrapolation", *Bioelectromagnetics*, Vol. 33, No. 6, pp. 466-475, 2012.

[3] C. Bornkessel and M. Schubert, "Exposure of the General Public to LTE Base Stations", 10th International Congress of the European Biolectromagnetics Association (EBEA 2011), Rome, Italy, 2011.

[4] D. Colombi, B. Thors, N. Wirén, L.-E. Larsson, C. Törnevik, "Measurements of downlink power level distributions in LTE networks", 2013 International Conference on Electromagnetics in Advanced Applications (ICEAA), Torino, Italy, 2013, pp. 98-101.

[5] ICNIRP, "Guidelines for limiting exposure to time-varying electric, magnetic and electromagnetic fields (up to 300 GHz)", *Health Physics*, Vol. 74, No. 4, pp. 494-522, 1998.

[6] 4G Americas, "4G Americas Global Deployments Status - 15 May 2014", http://www.3gamericas.org/UserFiles/file/Global%20Status%20Updates/May%2015/04_Eastern%20Europe%205_15_14.pdf.

[7] Anritsu, "LTE Resource Guide", 2009, http://www.anritsu.com/en-GB/Media-Room/Newsletters/files/anritsu_lte_guide.pdf.

[8] Commision for Communications Regulations (Ireland), "Programme of Measurement of Non-Ionising Radiation Emissions. Methodology for the Conduct of Surveys to Measure Non-Ionizing Electromagnetic Radiation from Transmitter Sites", Document No. 08/51R2, 24th January 2014, http://www.comreg.ie/_fileupload/publications/ComReg0851R2.pdf.

[9] C. Bornkessel, M. Schubert, M. Wuschek, "Bestimmung der Exposition der allgemeinen Bevölkerung durch neue Mobilfunktechniken (Determining general public exposure to emissions resulting from new mobile technologies)", Interim report prepared for the German Federal Office for Radiation Protection, 23 January 2012, http://www.emf-forschungsprogramm.de/akt_emf_forschung.html/dosi_HF_004_ZwB_01.pdf.

[10] C. Bornkessel, "Messung der elektromagnetischen Immissionen von LTE-Basisstationen (Measurement of electromagnetic emissions from LTE-base stations)", *EMF Spectrum*, No 1, pp. 10-15, 2011.

[11] M. Riederer, O. Lauer, P. Fahrni, R. Vahldieck, J. Fröhlich, "Characterization of the Electromagnetic Environment in a Hospital: Measurement Procedures and Results", *IEEE EMC Society Newsletter*, No. 224, pp.50-56, 2010.